UNIVERSITY OF CALGARY

Long-distance quantum communication with single solid-state spins

by

Faezeh Kimiaee Asadi

A THESIS
SUBMITTED TO THE FACULTY OF GRADUATE STUDIES
IN PARTIAL FULFILLMENT OF THE REQUIREMENTS FOR THE
DEGREE OF DOCTOR OF PHILOSOPHY

GRADUATE PROGRAM IN PHYSICS AND ASTRONOMY

CALGARY, ALBERTA

SEPTEMBER, 2020

Abstract

Long-distance transfer of quantum information is an essential ability for many applications of quantum science. A natural choice to distribute quantum information is to encode it into photons and transfer it through optical fibers. However, due to the unavoidable transmission losses present in every communication channel, the distances for efficient quantum communication via direct state transfer are limited to a few hundred kilometers. To overcome this limitation, the use of quantum repeaters has been suggested. A quantum repeater protocol aims to establish entanglement (i.e., quantum correlation) between remote nodes by first generating entanglement over shorter distance pieces, storing it in quantum memories, and finally extending it to the whole distance using entanglement swapping.

The main goal of this thesis is to design quantum repeater architectures using single solid-state quantum emitters and to develop the two-qubit gates required for performing entanglement swapping. We first explain the basic ideas of quantum repeaters and introduce potential material candidates, single erbium (^{168}Er) and europium (^{151}Eu) ions doped yttrium orthosilicate photonic crystals. Next, we propose a quantum repeater scheme combing erbium and europium ions to generate and distribute entanglement over long distances. We study the entanglement generation rate of the protocol and compare it with the rate of a well-known ensemble-based quantum repeater. Then, using cavity assisted interactions, we propose three different schemes to perform high fidelity two-qubit gates between single quantum systems. We quantify their expected performance in detail by taking into account many realistic imperfections and compare their strengths and weaknesses. The ability to perform local two-qubits gates is especially crucial in terms of distributing entanglement. Finally, based on our gained knowledge through these projects, we propose our second quantum repeater architecture based on erbium (^{167}Er) ions , which outperforms the first scheme. We study two possibilities for distributing entanglement and calculate the overall fidelity as well as the distribution rate of the protocol.

List of published papers and papers to be submitted

• **Paper 1:** Kimiaee Asadi, F., Lauk, N., Wein, S., Sinclair, N., O'Brien, C., and Simon, C. "Quantum repeaters with individual rare-earth ions at telecommunication wavelengths". Quantum 2, 93 (2018).

• **Paper 2:** Kimiaee Asadi, F., Wein, S. and Simon, C., "Cavity-assisted controlled phase-flip gates". Phys. Rev. A 102, 013703 (2020).

• **Paper 3:** Kimiaee Asadi, F., Wein, S. C., and Simon, C. "Protocols for long-distance quantum communication with single ^{167}Er ions". Quantum Science and Technology 5, 045015 (2020).

• **Paper 4:** Wein, S. C., Ji, J. W., Wu, Y. F., Kimiaee Asadi, F., Ghobadi, R., and Simon, C. "Analyzing photon-count heralded entanglement generation between solid-state spin qubits by decomposing the master-equation dynamics". Phys. Rev. A.102.3 033701 (2020).

• **Paper 5:** Ji, J. W., Wu, Y. F., Wein, S. C., Kimiaee Asadi, F., Ghobadi, R., and Simon, C. "A room-temperature quantum network with diamonds and optomechanics at telecommunication wavelengths", to be submitted (2020).

• **Paper 6:** Sharman, K., Kimiaee Asadi, F., and Simon, C. "Quantum repeaters based on individual electron spins and nuclear spin ensemble memories in quantum dots", to be submitted (2020).

Acknowledgements

I am so grateful for all the people who have accompanied me so far. I would especially wish to recognize my supervisor, Prof. Christoph Simon, for all his support, guidance and constructive criticisms, my family, especially my parents and sister, for their endless love and encouragement throughout my life, my co-workers for their contributions and help, and my friends for their constant support – Thank you

Table of Contents

List of Figures and Illustrations

Abbreviation

Abbreviation:	Definition:
Qubit	Quantum bit
BSM	Bell-state measurement
BS	Beam splitter
CNOT	Controlled-NOT
CZ	Controlled-Z
DLCZ	Duan-Lukin-Cirac-Zoller
QKD	Quantum key distribution
QED	Quantum electrodynamics
NV	Nitrogen vacancy
SiV	Silicon vacancy
Er	Erbium
Eu	Europium
Yb	Ytterbium
YSO	Yttrium orthosilicate
YVO	Yttrium ortho-Vanadat
REI	Rare-earth ion
MW	Microwave
ZEFOZ	Zero first-order Zeeman
FWHM	Full width half maximumn

Chapter 1

Introduction

Quantum communication is the art of encoding quantum states into photons and transmitting them between distant locations to perform communication tasks that are impossible using classical resources [1]. Among many quantum communication applications are quantum teleportation [2], quantum cryptography [3], long-baseline telescopes [4] and in the long-term, a network of quantum computers or a quantum internet [5, 6].

The use of quantum repeaters could overcome distance barriers to long-distance quantum communications such as transmission loss [7]. The realization of quantum repeaters requires the ability to interface various components such as quantum emitters and quantum memories. The primary objective of the work done for this thesis has been to investigate the possibilities of designing fiber-based quantum repeaters using individual rare-earth ions doped into crystals.

This thesis is organized as follows: In the first chapter, I present a brief description of the essential elements and resources required in quantum communication and how they relate to each other. Next, I discuss the physical systems we employed to propose our quantum repeater protocols, i.e., individual rare-earth ions. Chapters 3, 4 and 5 contain published papers. To be more precise, the third chapter presents our first quantum repeater scheme based on single erbium ($^{168}\mathrm{Er}^{3+}$) and europium ($^{151}\mathrm{Eu}^{3+}$) rare-earth ions as communication and memory qubits, respectively. The fourth chapter covers cavity mediated interactions between quantum systems. The fifth chapter explains our second quantum repeaters protocol, where we perform the entanglement generation and storage processes using a single species of ion, i.e., $^{167}\mathrm{Er}^{3+}$. Finally, the thesis is concluded in chapter six.

1.1 Qubits

While a classical bit can take values of either '0' or '1', the basic unit of quantum information, known as a qubit (i.e., a quantum bit [8]), could be in a coherent superposition of orthogonal quantum states $|0\rangle$ and $|1\rangle$ as follows

$$|\psi\rangle = \alpha\,|0\rangle + \beta\,|1\rangle\,, \tag{1.1}$$

where α and β are complex parameters that satisfy the equation $|\alpha|^2 + |\beta|^2 = 1$. The probability of finding the quantum state $|\psi\rangle$ in the state $|0\rangle$ ($|1\rangle$) is therefore given by $|\alpha|^2$ ($|\beta|^2$). In this thesis, we also use some other standard notations to represent qubit states; $|0\rangle = |\uparrow\rangle$ and $|1\rangle = |\downarrow\rangle$.

One can also visualize qubit states as points on a spherical surface with radius 1 and represent an arbitrary qubit state as

$$|\psi\rangle = \cos{(\frac{\theta}{2})}\,|0\rangle + e^{i\varphi}\sin{(\frac{\theta}{2})}\,|1\rangle\,, \tag{1.2}$$

where in spherical coordinates $0 \leq \varphi \leq 2\pi$ can be interpreted as the longitude (with respect to the x-axis) and $0 \leq \theta \leq \pi$ as the colatitude (with respect to the z-axis). This sphere, which is called the Bloch sphere, is shown in Fig. 1.1. The north pole of this unit sphere represents the state $|0\rangle$, and the south pole represents the state $|1\rangle$. Clearly the superposition state $1/\sqrt{2}(|0\rangle + |1\rangle)$ ($1/\sqrt{2}(|0\rangle + i\,|1\rangle)$), could be depicted by a Bloch vector pointing to the equator along the $\hat{x}$ ($\hat{y}$) axis. The most general state of a qubit could be represented by a

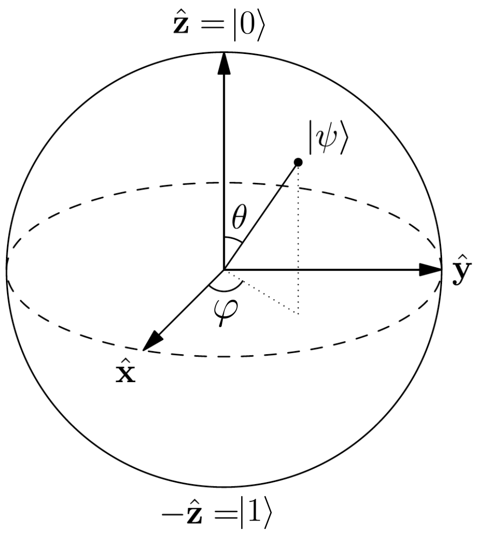

Figure 1.1: Bloch sphere representation of a qubit state. The state of any two-level quantum system, such as the Bloch vector $|\psi\rangle$, represents by a point on the Bloch sphere

2×2 matrix, i.e., density matrix ρ as follows

$$\rho = \frac{1}{2}\left(I + \vec{r}.\vec{\sigma}\right) = \frac{1}{2}\begin{bmatrix} 1+z & x-iy \\ x+iy & 1-z \end{bmatrix}, \tag{1.3}$$

where I is the 2×2 identity matrix, $\vec{r}$ is a vector in the Bloch sphere and $\vec{\sigma} = (\sigma_1, \sigma_2, \sigma_3)$ are Pauli matrices which are commonly denoted by a variety of notations (see Sec.1.2). Therefore, points on the surface of the Bloch sphere represent pure states (Bloch vectors of unit length). In contrast, mixed states (i.e., statistical ensembles of pure states [9]) lie in the interior of the sphere (as an example $r = 0$ corresponds to the mixed state $\rho = \frac{1}{2}I$). In general, a quantum memory consisting of n qubits could be in a linear combination of 2^n possible quantum states.

Similarly, a pure state of a qudit (i.e., a d-dimensional quantum system) can be written as

$$|\psi\rangle = \alpha_0 |0\rangle + \alpha_1 |1\rangle + ... + \alpha_{d-1} |d-1\rangle . \tag{1.4}$$

The density matrix of a qudit is also in the form of $\rho = \frac{1}{2}\left(I + \vec{r}.\vec{\Gamma}\right)$ where Γ_i, $i = 1, 2, ..., d^2-$

1 are traceless hermitian operators in the space of a qudit.

Although quantum has the advantage of using superposition states, in the end, the qubit (or qudit) state can only be measured in one basis (i.e., the result of the measurement is interpreted as either ‘0’ or ‘1’). However, using, for example, the quantum dense coding, one can transmit two classical bits of information to another party using only one qubit [10]. Besides, using two classical bits, quantum teleportation allows us to transfer one qubit state between two distant locations (see Sec 1.6).

1.2 Quantum gates

Analogues to logic gates in classical computers, quantum gates are building blocks of quantum computers. Quantum gates are represented by unitary matrixes. The matrix U is unitary if $UU^\dagger = U^\dagger U = 1$ where $U^\dagger$ is conjugate transpose of U. In general, a $2^n \times 2^n$ unitary matrix can represent a gate that acts on n qubits. In the following, we explain some simple quantum gates that will be used in the next chapters.

1.2.1 Single-qubit gates

• **Pauli-X gate:** The X gate, which is equivalent to the NOT gate in classical computation, in matrix form is written as

$$\sigma_1 \equiv \sigma_x \equiv X \equiv \begin{bmatrix} 0 & 1 \\ 1 & 0 \end{bmatrix}. \tag{1.5}$$

In a vector notation qubit states $|0\rangle$ and $|1\rangle$ are denoted by $|0\rangle = \binom{1}{0}$ and $|1\rangle = \binom{0}{1}$. Therefore, the corresponding output from the Pauli-X gate (also called bit-flip gate) is to map $|0\rangle$ to $|1\rangle$ and $|1\rangle$ to $|0\rangle$.

• **Pauli-Z gate:** This gate rotates the quantum state of a qubit around the $\hat{z}$-axis of the Bloch sphere by π (it is therefore also called a phase-flip gate). In the matrix notation, this gate is represented by

$$\sigma_3 \equiv \sigma_z \equiv Z \equiv \begin{bmatrix} 1 & 0 \\ 0 & -1 \end{bmatrix}. \tag{1.6}$$

As a result, this gate leaves the state $|0\rangle$ unchanged and flips the sign of $|1\rangle$ to $-|1\rangle$.

• **Pauli-Y gate:** This gate represents a rotation by π about the $\hat{y}$-axis of the Bloch sphere:

$$\sigma_2 \equiv \sigma_y \equiv Y \equiv \begin{bmatrix} 0 & -i \\ i & 0 \end{bmatrix}. \tag{1.7}$$

Hence, the Pauli-Y gate, which is equivalent to XZ gate (except for an 'i'), flips both phase and bit of a qubit state.

• **Hadamard gate:** The Hadamard gate acts as a rotation around the $(\hat{x} + \hat{z})/\sqrt{2}$-axis by π (or equivalently a rotation about the $\hat{y}$-axis by $\pi/2$, followed by a π rotation about the $\hat{x}$-axis)

$$H \equiv \frac{1}{\sqrt{2}} \begin{bmatrix} 1 & 1 \\ 1 & -1 \end{bmatrix}. \tag{1.8}$$

Therefore, it maps the state $|0\rangle$ to $(|0\rangle + |1\rangle)/\sqrt{2}$ (i.e., first column of H which is half way between $|0\rangle$ and $|1\rangle$) and $|1\rangle$ to $(|0\rangle - |1\rangle)/\sqrt{2}$ (i.e., second column of H).

1.2.2 Two-qubit gates

• **Controlled-Z (CZ) gate:** This gate is a controlled version of the Z gate with two input qubits, i.e., control and target qubits. It, therefore, flips the phase of the second qubit (i.e., target qubits), only if the control qubit is in the state $|1\rangle$. In the matrix notation, this gate is represented by

$$CZ \equiv \begin{bmatrix} 1 & 0 & 0 & 0 \\ 0 & 1 & 0 & 0 \\ 0 & 0 & 1 & 0 \\ 0 & 0 & 0 & -1 \end{bmatrix}. \tag{1.9}$$

In Chapter 4, we propose three different schemes to perform the CZ gate between two quantum systems.

- **Controlled-X (CNOT) gate:** The most well-know two-qubit gate is the CNOT gate. This gate performs a conditional negation of the target qubit. To be more precise, it performs a NOT operation on the target qubit only if the control qubit is in the state $|1\rangle$. The matrix representing the CNOT gate is

$$CNOT \equiv \begin{bmatrix} 1 & 0 & 0 & 0 \\ 0 & 1 & 0 & 0 \\ 0 & 0 & 0 & 1 \\ 0 & 0 & 1 & 0 \end{bmatrix}. \tag{1.10}$$

Hence, this gate is analogous to the XOR operation in classical computation. The CNOT gate can be decomposed as a sequence of a CZ gate and two Hadamard gates, i.e., $(I \otimes H)\, CZ\, (I \otimes H)$ (see section 5.3.2 for more information).

1.3 Entanglement

Entanglement is a form of non-classical correlation between two or more particles that could be potentially distantly located. A system composed of two or more subsystems is in an entangled state if its state can not be written as a tensor product of the states of the individual subsystems (or for mixed states, a convex combination of product states).

A pure bi-partite state $|\psi\rangle_{A,B}$, for example, is not entangled if it is separable as follows

$$|\psi\rangle_{A,B} = |\psi\rangle_A \otimes |\psi\rangle_B\,. \tag{1.11}$$

In a more general case, a mixed bi-partite state which is represented by a density operator $\rho_{A,B}$ (i.e., a matrix that describes a system's statistical state), is separable if it can be written as

$$\rho_{A,B} = \sum_i p_i \, \rho_A^{(i)} \otimes \rho_B^{(i)}, \tag{1.12}$$

where $\sum_i p_i = 1$ and p_i is a probability distribution.

A possible state of two qubits could be in any linear combination of basis states, $|00\rangle$, $|10\rangle$, $|01\rangle$ and $|11\rangle$. As an example, consider a bi-partite entangled state $1/\sqrt{2}\,(\,|0\rangle_1|1\rangle_2 + |1\rangle_1|0\rangle_2\,)$ where the subscript 1 (2) represent the first (second) qubit. Obviously, one cannot write this state in terms of the individual qubit states. Here, either the first qubit is in the state $|0\rangle_1$ and the second is in the state $|1\rangle_2$ or the second qubit is in the sate $|0\rangle_2$ and the first is in the state $|1\rangle_1$. If one measures the first qubit to be in the state $|1\rangle_1$, the state of the second qubit is instantaneously projected into the state $|0\rangle_2$. However, until the moment of measuring, the second qubit could take any of the states $|0\rangle_2$ or $|1\rangle_2$ with equal probabilities $|1/\sqrt{2}|^2 = 1/2$.

Therefore, entanglement prohibits the description of each subsystem as an individual entity. Instead, it leads to a quantum correlation between the outcomes of experiments that can be performed on subsystems individually. In section 3.3.1, we study a method to generate entanglement between photon-ion and ion-ion pairs in detail.

1.4 Bell State Measurement

In bi-partite systems, the maximally entangled states are commonly known as Bell states [9]:

$$\begin{aligned} |\psi^{\pm}\rangle &= \frac{1}{\sqrt{2}}(|01\rangle \pm |10\rangle), \\ |\phi^{\pm}\rangle &= \frac{1}{\sqrt{2}}(|00\rangle \pm |11\rangle). \end{aligned} \tag{1.13}$$

These four states form an orthonormal basis (i.e., unit vectors that are orthogonal to each other) for the two-qubit state space. A measurement in this basis, called a Bell state measurement (BSM), projects the state of the two qubits into one of the Bell states. Hence, it is also referred to as an entangling measurement. The most common way to do a partial Bell state measurement is by employing a beam splitter (BS) with two input and two output ports and a measurement device at each output port. The measurement devices should be able to identify two orthogonal modes of the degree of freedom that is used to encode the qubits. Two indistinguishable (in all except the chosen degree of freedom for qubit encoding) photons that have never interacted are directed into the input ports of a BS and detected by single-photon detectors. The projection of the state of photons into one of the Bell states will then happen due to the two-photon interference principle.

For example, consider that input spatial modes of the BS are labelled as 1 and 2, and output modes are 3 and 4. After undergoing the BS transformation, the Bell states become

$$\begin{aligned}
|\psi^+\rangle_{1,2} &= \frac{1}{\sqrt{2}}(|01\rangle_{1,2} + |10\rangle_{1,2}) \Longrightarrow \frac{i}{\sqrt{2}}(|01\rangle_{3,3} + |10\rangle_{4,4}) \\
|\psi^-\rangle_{1,2} &= \frac{1}{\sqrt{2}}(|01\rangle_{1,2} - |10\rangle_{1,2}) \Longrightarrow \frac{1}{\sqrt{2}}(|01\rangle_{3,4} - |10\rangle_{3,4}) \\
|\phi^\pm\rangle_{1,2} &= \frac{1}{\sqrt{2}}(|00\rangle_{1,2} \pm |11\rangle_{1,2}) \Longrightarrow \frac{i}{2}(|00\rangle_{3,3} + |00\rangle_{4,4} \pm |11\rangle_{3,3} \pm |11\rangle_{4,4}).
\end{aligned} \tag{1.14}$$

Therefore, simultaneous detection of photons in orthogonal state $|0\rangle$ and $|1\rangle$ in different output ports of the beam-splitter corresponds to a projection into the state $|\psi^-\rangle$. On the other hand, the coincidence of photons in orthogonal states, but the same output port corresponds to a projection into the state $|\psi^+\rangle$. It is obvious that this setup cannot distinguish other two Bell states $|\phi^\pm\rangle$ from each other. However, they are still distinguishable from the states $|\psi^\pm\rangle$. Since only half of the four Bell states are identified by measurement outcomes, the maximum success rate of this scheme is 50% [11].

Bell state measurements perform a key role in many quantum communication protocols such as quantum teleportation, entanglement swapping and quantum repeaters, as discussed in the next sections.

1.5 No-cloning theorem

Although in classical information the possibility of copying is an essential feature, the no-cloning theorem states that it is impossible to copy an arbitrary unknown quantum state perfectly [12]. It should be noted that entanglement generation does not violate the no-cloning theorem as cloning refers to the generation of the separable and definite quantum states, whereas entangled systems do not have well-defined states individually. To understand the no-cloning theorem, assume that we want to make a copy of the quantum state $|\psi\rangle$ starting from the quantum state $|0\rangle$ using a cloning machine with a unitary operation $\hat{U}$:

$$\hat{U}\left(|\psi\rangle \otimes |0\rangle\right) = |\psi\rangle \otimes |\psi\rangle . \tag{1.15}$$

Similarly, we can demand that for another quantum state $|\phi\rangle$ which is orthogonal to the state $|\psi\rangle$ (i.e.,$\langle\phi|\psi\rangle = 0$) we have $\hat{U}\left(|\phi\rangle \otimes |0\rangle\right) = |\phi\rangle \otimes |\phi\rangle$. Now consider an arbitrary unknown quantum state as a state we want to make a copy of. In this case for a perfect copier we would need to have

$$\hat{U}\left(\left(\alpha|\psi\rangle + \beta|\phi\rangle\right) \otimes |0\rangle\right) = \left(\alpha|\psi\rangle + \beta|\phi\rangle\right) \otimes \left(\alpha|\psi\rangle + \beta|\phi\rangle\right). \tag{1.16}$$

If we expand the right hand side of the above equation and multiply it once by $\langle\psi|\langle\psi|$ and once by $\langle\phi|\langle\phi|$, knowing that $\langle\phi|\phi\rangle = \langle\psi|\psi\rangle = 1$, we get $\alpha^2 = \alpha$ and $\beta^2 = \beta$, respectively. Using these results, one can simplify Eq.1.16 as:

$$\alpha\beta|\psi\rangle \otimes |\phi\rangle + \beta\alpha|\phi\rangle \otimes |\psi\rangle = 0 \tag{1.17}$$

Multiplying Eq.1.17 by $\langle\psi|\langle\phi|$ then, leads to $\alpha\beta = 0$, which is satisfied only if $\alpha = 0$ or $\beta = 0$, which clearly is not the case for an arbitrary quantum state. Although the no-cloning theorem forbids the perfect copying of an unknown quantum state, it is still possible to approximately clone the state using a universal quantum-cloning machine (see Ref [13] and references therein).

The no-cloning theorem has important consequences: it is essential for the quantum cryptography security as it does not let eavesdroppers make copies of transmitted quantum states in the quantum key distribution protocols [3, 13]. Besides, this theorem also ensures the impossibility of faster-than-light communication in quantum mechanics [14]. To understand this, assume that quantum states could be cloned. Then, consider two parties (i.e., Alice and Bob) that are distantly located, sharing a maximally entangled state (e.g., $|\phi^+\rangle$). Alice and Bob have agreed on a way of sending bits to each other: if Alice wishes to transmit a '0', she does not do any measurements on her qubit. Otherwise (i.e, to transfer '1'), she measures her qubit in the Z basis (see Sec.1.2.1), which in turn projects the state of Bob's qubit into either $|0\rangle$ or $|1\rangle$ states. Therefore, if Bob makes many copies of his qubit state and measures them all in Z basis, he will see completely random measurement outcomes if Alice has transmitted '0'. On the other hand, he gets the same result for all measurements if Alice has transmitted '1'. This would allow Alice and Bob to transfer classical bits over potentially long distances without any communication, violating Einstein's theory of relativity.

1.6 Quantum teleportation

It is very easy to determine the state of an unknown classical bit, as it can be either '0' or '1'. On the other hand, as shown in Eq.1.1, the state of an unknown qubit could be in any superposition state that cannot be uniquely determined by any quantum measurement. However, one can use quantum teleportation to transfer an unknown quantum state to a spatially separated location without the carrier's transmission [2]. Consider that $|p\rangle = \alpha|0\rangle + \beta|1\rangle$ is the state of a photon that we want to teleport. To perform this process, we share a maximally entangled state of two photons between the sender (e.g., Alice) and receiver (e.g., Bob), as shown in Fig.1.2. In this case, the original state of the three photons

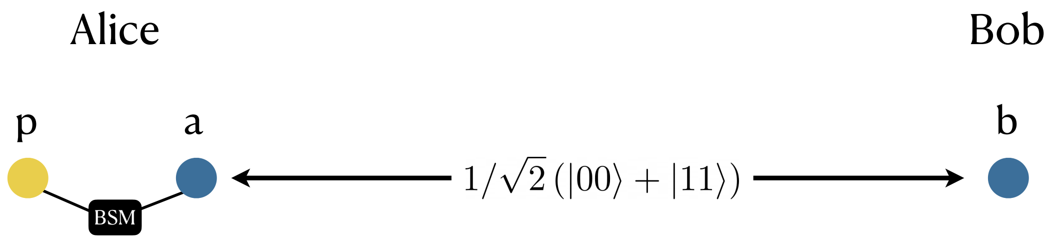

Figure 1.2: An example of a quantum teleportation scheme to teleport an unknown state $\alpha\,|0\rangle + \beta\,|1\rangle$ of the photon 'p' to Bob. Here we assume the state $|\phi^+\rangle$ remains entangled, meaning that the transportation is free from decoherence.

is

$$|\psi\rangle_{abp} = |\phi^+\rangle_{ab} \otimes |p\rangle_p = \frac{1}{\sqrt{2}}(|00\rangle_{ab} + |11\rangle_{ab}) \otimes (\alpha\,|0\rangle_p + \beta\,|1\rangle_p), \tag{1.18}$$

where $|\phi^+\rangle_{ab}$ is the state of the shared entangled photon pair between Alice and Bob. Using Eq.1.13, one can re-write the above equation as follows

$$\begin{aligned} |\psi\rangle_{abp} = \frac{1}{2}\big(\; & |\phi^+\rangle_{ap} \otimes (\alpha\,|0\rangle_b + \beta\,|1\rangle_b) + \\ & |\phi^-\rangle_{ap} \otimes (\alpha\,|0\rangle_b - \beta\,|1\rangle_b) + \\ & |\psi^+\rangle_{ap} \otimes (\beta\,|0\rangle_b + \alpha\,|1\rangle_b) + \\ & |\psi^-\rangle_{ap} \otimes (-\beta\,|0\rangle_b + \alpha\,|1\rangle_b)\,\big). \end{aligned} \tag{1.19}$$

To transfer the state of photon 'p' into the photon 'b', Alice performs a BSM on her two photons (i.e., 'a, and 'p'). Depending on the result of the Bell state measurement, the state of Bob's photon collapses into one of the states shown in Eq.1.19. As an example, if the resulting Bell state is $|\psi^+\rangle_{ap}$, Bob's photon state collapses $(\beta\,|0\rangle_b + \alpha\,|1\rangle_b)$. Now, all Alice needs to do is inform Bob about the BSM results using classical communication. Then, Bob can perform an appropriate unitary transformation (here the spin-flip gate X) to recover the original state. Note that, since classical communication is an essential ingredient of this protocol, one cannot use entanglement teleportation to send messages faster than light.

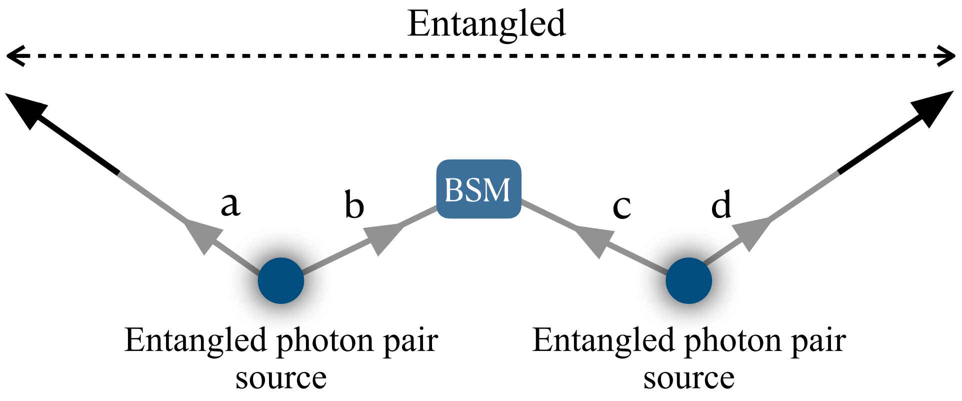

Figure 1.3: Distributing entanglement by performing entanglement swapping. Initially, there are two entangled pairs (a,b) and (c,d). Performing a BSM on photons 'b' and 'c' teleports the state of the photon 'b' to 'd' and 'c' to 'a' and leaves photons 'a' and 'd' in an entangled state.

1.7 Entanglement swapping

Entanglement swapping is very similar to quantum teleportation except that the qubit we aim to teleport is now part of an entangled state [15]. This process, which is also known as teleportation of entanglement, requires two pairs of entangled particles like photons (a,b) and (c,d). The idea is to interfere one member of each pair (i.e., 'b' and 'c') to perform a BSM so that the other members (i.e., 'a' and 'd') are projected into an entangled state, as shown in Fig. 1.3.

As an example, we consider the original state of the four photons as

$$|\psi\rangle_{abcd} = \frac{1}{\sqrt{2}}(|00\rangle_{ab} + |11\rangle_{ab}) \otimes \frac{1}{\sqrt{2}}(|00\rangle_{cd} + |11\rangle_{cd}), \tag{1.20}$$

which is equivalent to

$$|\psi\rangle_{abp} = \frac{1}{2}\left(|\phi^+\rangle_{ad} \otimes |\phi^+\rangle_{bc} + |\phi^-\rangle_{ad} \otimes |\phi^-\rangle_{bc} + |\psi^+\rangle_{ad} \otimes |\psi^+\rangle_{bc} + |\psi^-\rangle_{ad} \otimes |\psi^-\rangle_{bc}\right). \tag{1.21}$$

Therefore, after Bell state measurement, if the state of photons 'b' and 'c' is projected, for instance, into $|\psi^-\rangle_{bc}$, the resulting entangled state between 'a' and 'd' would be $|\psi^-\rangle_{ad}$.

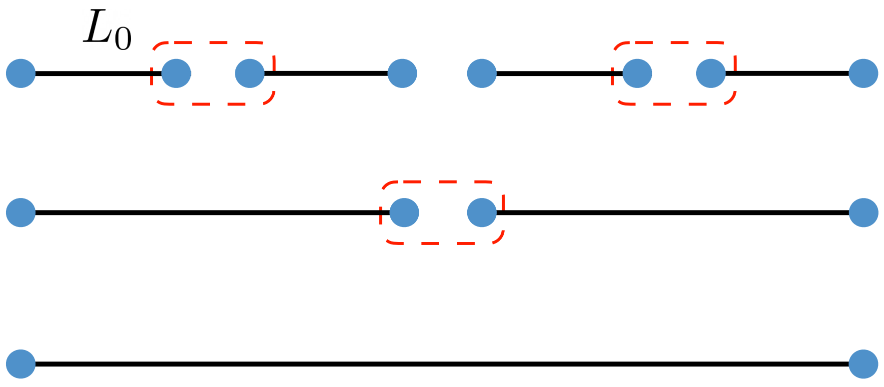

Figure 1.4: Quantum repeaters aim to create a pair of entangled quantum systems between two distant locations. To generate this pair, first, we create and store entanglement between shorter distance pairs over elementary links. Then, we swap entanglement between neighboring nodes. As a result, we have an entangled pair between the outer nodes. By repeating the swapping process, one can distribute entanglement over the entire distance.

1.8 Quantum repeaters

The maximum distance over which one can transmit photons is limited by the attenuation of the transmission channel. A convenient way in both classical and quantum communication is to distribute photons using optical fibers. The attenuation length of the available optical fibers in the telecommunication wavelengths (between 1.530 and 1.565 μm) is about $L_{att} =$ 22 km (corresponding to a loss of 0.2 dB/km). As a result, the transmission loss, which grows exponentially with distance, becomes very significant over large distances. To give an example of the impact of such loss, consider that for a single-photon source with a very high repetition rate of 10 GHz, the photon transmission rate over 1000 km would be 10^{-10}, which corresponds to 300 years. Classical communication overcomes this limitation using amplifiers that compensate for the loss by copying and regenerating the original signal. In quantum communication, however, due to the no-cloning theorem, it is impossible to make an exact copy or reproduce an unknown quantum state. Therefore, using amplifiers for quantum communication add too much noise to the amplified signal and eventually destroy the coherence of the quantum states [16] (see also chapter 7 of Ref [17]). Instead, quantum communication can use quantum repeaters based on entanglement swapping [7]. The idea of a quantum repeater is to divide the total desired distance L into 'm' sub-links (refer to as elementary links) of length $L_0 = L/m$. Then, entanglement needs to be established between the ends of each elementary link individually. The successful realization of remote entanglement can be announced by a heralding signal after a photon detection event. i.e., "click". Most of the entanglement generation protocols are probabilistic, meaning that it may not be possible to generate entanglement over all elementary links at the same time. However, after generating entanglement over an elementary link, one can store it using quantum memories until entanglement is established in neighboring links as well. Once entanglement is generated over neighboring links, it is distributed via entanglement swapping by performing, for example, Bell state measurement between adjacent quantum memories.

Using fiber-based quantum repeaters, it should be possible to distribute entanglement up to a few thousand kilometer range. For global distances, however, we may require quantum networks that incorporate quantum satellite, i.e., low-earth orbit satellites (alone or in combination with quantum repeaters) or geostationary satellites.

1.9 Quantum memory

Many approaches to designing quantum repeaters are based on linear optics and atomic ensembles as quantum memories [18, 19]. These schemes require the collective excitation of atomic ensembles. Hence, it is relatively easy to control the coupling between memory and photons. However, when using linear optics, due to its intrinsic limitation (see Sec.1.4), entanglement distribution rates of these protocols are relatively low. On the other hand, it is possible to overcome this limitation using single-emitter-based quantum repeaters and perform entanglement swapping deterministically (see Chapters 3 and 5).

Over the last few years, several experimental groups have addressed single rare-earth ions [20, 21, 22, 23], making it possible to envision a scalable quantum repeater scheme using them. Therefore, in this thesis, we focus on the quantum repeater protocols based on single emitters and, more specifically, individual rare-earth ions.

- **Storage time:** Within the main requirements of a quantum memory is storing entanglement for a certain amount of time (referred to as storage time). In principle, in the context of quantum communication, longer storage time will increase the maximum transmission distance. In this thesis, we encode qubit states into the ground state energy levels of ions. Therefore, the spin coherence time defines the storage time of the ion (see also sections 3.3 and 5.3 for more information).

In chapter 5, we discuss a repeater protocol that uses two species of ions, one as a communication qubit to generate entanglement over elementary links, and one as a memory qubit to store entanglement. To generate entanglement between remote ions, we first generate entanglement between each ion and a spontaneously-emitted photon. Then, we perform a Bell state measurement on the emitted photons in a station located half-way between the ions (to make the scheme more robust against some errors such as detector and photon loss we repeat this process twice [24]). It means that the communication qubit's storage time should be at least twice the time it takes for the photon to travel to the middle station plus a classical signal to go back the same distance to inform us about the result of the measurement. On the other hand, after generating entanglement over an elementary link, the quantum memory should be able to store entanglement until it is also created across the adjacent link (in section 3.4 we will discuss this waiting time in detail). Later, in Chapter 5, we use a single species of ions (rather than a doubly doped crystal) to design our second repeater protocol. Therefore, in this case the ion's coherence time should be long enough to cover the entanglement generation and waiting times required before performing entanglement swapping.

- **Fidelity and efficiency:** In quantum communication, it is also crucial for quantum memories to allow the implementation of entanglement swapping with a high fidelity and efficiency. In the context of entanglement swapping between two quantum memories, for example, efficiency is the success probability of performing it (how often it succeeds). Therefore, the efficiency or the scheme's repeatability directly affects the entanglement distribution rate of a repeater protocol. Fidelity, on the other hand, shows how close the imperfect final state is to the ideal state after performing a Bell state measurement or any other quantum operations. It is, therefore, a measure of how well a quantum state is maintained. In section 4.6.1, we discuss the fidelities of three different schemes to implement a two-qubit gate, which could be used to perform entanglement swapping between two quantum memories.

Chapter 2

Physical system

Both quantum repeater protocols described in this thesis rely on the use of rare-earth (RE) ions. Therefore, in this chapter, we explain the main features of rare-earth ions (including erbium and europium) that are important for the development of our proposed quantum repeaters.

2.1 Rare-earth ions

The rare-earth elements (also known as lanthanide series) are 15 metallic elements with atomic numbers between 57 (lanthanum) to 71 (lutetium). The electron configuration of these elements is $[\mathrm{Kr}]\,4d^{10}\,5s^2\,5p^6\,4f^n\,5d^1\,6s^2$ where $n = 0, 2, \cdots, 14$. Rare-earth ions doped into crystals usually lose their three outer electrons (i.e. the $5d$ and two $6s$ electrons) and occur as triple-positive ions. In these ions, the $4f$ shell is to some extent shielded from the crystal environment by the outer 5s and 5p shells which have larger radial distributions. As a result, even when doped into crystals, these ions keep many of the optical properties of free ions, e.g., they have a weak interaction with the environment. Therefore, the $4f - 4f$ transitions are less subject to the decoherence at low-temperature [25].

When an ion is doped into a crystal, the electrostatic crystal field splits its energy states depending on the number of $4f$ electrons and the crystal symmetry. Hence, RE ions divide into two groups; ions with an odd number of $4f$ electrons (also called Kramers ions) and ions with an even number of $4f$ electrons (non-Kramers ions) [26]. The magnetic properties of Kramers and non-Kramers ions are different. Because of the unpaired electron, Kramers ions tend to have significant magnetic moments on the order of the Bohr magneton μ_B. As a result, they are more susceptible to interact with the environment, e.g., through the magnetic dipole-dipole interaction. Ions belonging to this group are Er^{3+}, Yb^{3+}, Nd^{3+}, Sm^{3+}, Dy^{3+} and Ce^{3+}. On the other hand, weaker magnetic interactions in non-Kramers ions result in slower spin-relaxation rates and longer coherence times in these ions compared to the Kramers ions. Eu^{3+}, Pr^{3+}, Tm^{3+}, Pm^{3+}, Tb^{3+} and Ho^{3+} belong to this category.

In free ions, the energy eigenstates have a $2J + 1$ fold degeneracy, where J is the total angular momentum. However, when the ion is doped into a crystal, depending on the crystal symmetry and the number of $4f$ electrons, the crystal field splits energy levels with the same J but different m_j. Kramers ions with an unpaired electron can be split into at most $J+1/2$ energy levels (so-called Kramers doublets). However, for non-Kramers ions, the crystal field totally removes the J degeneracy and split it into $2J + 1$ level.

2.1.1 Homogeneous broadening

The homogeneous linewidth, Γ_h, is a measure of the intrinsic spectral linewidth for an individual ion, i.e., the frequency interval in which an individual ion absorbs or emits radiation. The homogeneous linewidth is connected to the coherence lifetime (also known as optical phase memory), T_2 as:

$$\Gamma_h = \frac{1}{\pi T_2}. \tag{2.1}$$

The coherence time T_2 is the time in which a quantum state keeps its phase. The coherence time can be at most twice the population lifetime T_1. The latter is the average time for an ion in an excited state to decay into a lower-lying state. The homogeneous linewidth is therefore bounded by the excited state lifetime T_1 of the relevant transition ($\Gamma_h \geq 1/2\pi T_1$).

In certain ion-host combinations where all other dephasing processes are minimized, it is possible to approach this ultimate limit. For instance, for erbium and europium ions doped into yttrium orthosilicate crystal, the homogeneous linewidth can reach the order of Hertz [27, 28, 29].

In general the main processes, which could lead to the homogeneous line broadening, are interactions between the dopant ions [30, 31], electron and nuclear spin fluctuations of the host ions, and lattice phonons [32]. Interaction between rare-earth ions with each other in the host material can be suppressed by increasing the average distance between the ions through the spin ensemble dilution [33]. Choosing host materials with small or zero nuclear magnetic moments, on the other hand, can minimize the fluctuating field caused by flipping of nuclear spins of neighboring atoms [34]. Besides, applying a magnetic field is also able to decrease spin flipping around the ion, for example, through the frozen-core (see Sec 3.5) [35, 36]. Finally, density of lattice phonons can be reduced by decreasing the temperature to a few Kelvin or less [33].

Information on the homogeneous linewidth can be obtained from the decay of the two-pulse photon echo. In this method, using the first pulse (which is ideally a $\pi/2$ pulse), we create a coherent superposition of the ground and excited states. Following the first pulse, the different ions get out of phase as ions have a slightly different resonant frequency (see next section for more information). After a time t_2, a second pulse (which is ideally a π pulse) is applied to reverse all phases. Then, the phase of each ion continues to evolve until at a time $2\,t_2$, when all ions are in phase again, and the photon echo is produced. By measuring the echo intensity as a function of pulse delay, one can extract information about the coherence time T_2, and therefore the homogeneous linewidth.

2.1.2 Inhomogeneous broadening

Rare-earth ions feel slightly different crystal fields at different positions of a host crystal. This spatial dependency of the crystal field usually happens because of the manufacturing

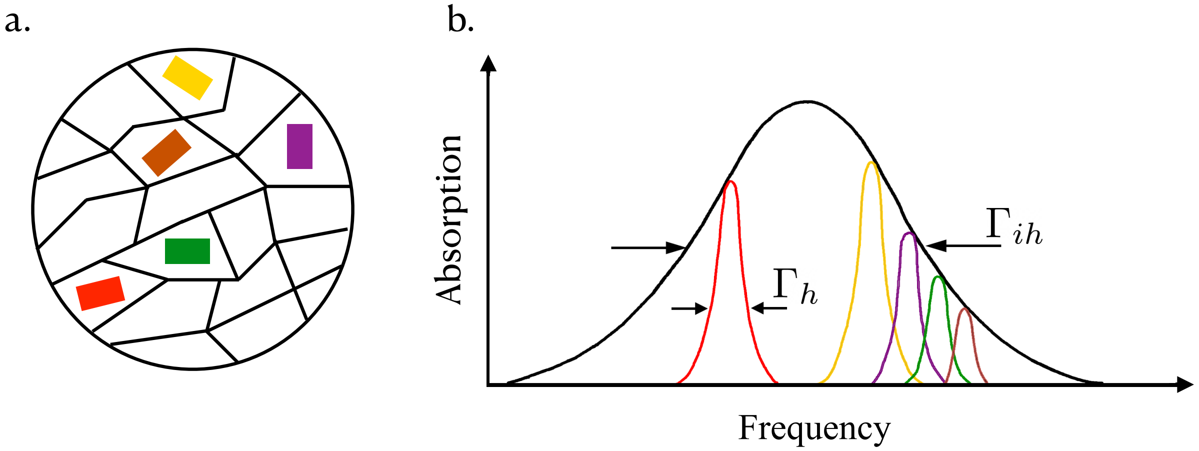

Figure 2.1: Inhomogeneous broadening. **a.** Ions in the host crystal experience different local environments. **b.** Number of ions with respect to the optical transition frequencies of ions. The sum of the homogeneous broadening of individual ions, Γ_h, forms the inhomogeneously broadened absorption line Γ_{ih}. This figure is reproduced from Ref.[37].

imperfections, the random distribution of the dopants, and also the different size of the doped ion compared to the host ion it is replacing in the crystal. Hence, the optical transition frequencies of individual ions are also slightly different (see Fig. 2.1). This variation in the transition frequencies results in the inhomogeneous broadening of an absorption line. The width of the total frequency interval in which an ensemble of ions can collectively absorb or emit radiation is called inhomogeneous linewidth, Γ_{ih}. The inhomogeneous linewidth depends strongly on the host crystal, and up to the first order is independent of temperature. In general, the inhomogeneous broadening increases by increasing the dopant concentration. The number of addressable frequency channels is given by the ratio Γ_{ih}/Γ_h. The rate is especially important as it determines the number of available spectral modes that can be used for information storage (see Sec.3.4 for more information).

2.1.3 Er^{3+}:YSO

Triple-positive erbium ions have eleven electrons in their $4f$ shell with the ground state $^4I_{15/2}$ and the lowest excited state of $^4I_{13/2}$. Therefore, these states have a 16 (corresponding

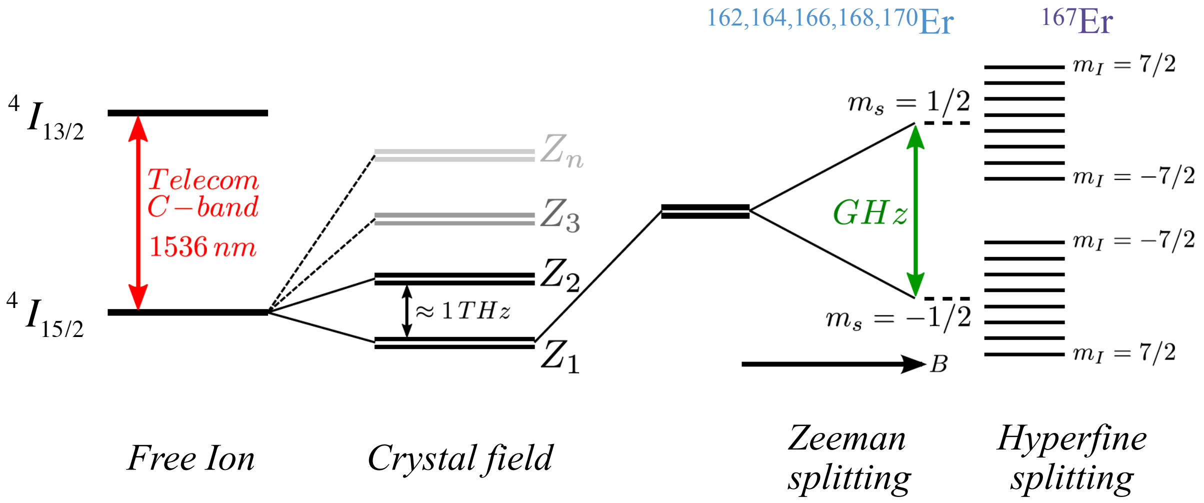

Figure 2.2: Ground state energy levels of erbium ions in a host crystal. The optical transition frequency of this ion is in the telecom wavelengths, where absorption loss in optical fibres is minimum. This figure is reproduced from Ref.[38].

to $J = 15/2$) and 14 (corresponding to $J = 13/2$) fold degeneracy, respectively. The host crystal we focus on in this thesis is yttrium orthosilicate Y_2SiO_5 (YSO) because of the small magnetic moments of its constituents (see section 3.5 for more information). When doped into the YSO crystal, Er ions replace yttrium (Y^{3+}) ions of the host. The crystal field splits the degeneracy of the energy levels and form eight doublets in the ground and seven doublets in the excited states. At low temperatures, only the lowest doublet of the ground state is populated. This doublet is described with an effective spin $S_{eff} = 1/2$, which is a fictitious angular momentum. In the presence of an external magnetic field, the Zeeman splitting happens, and each Kramers doublets splits into two levels. Figure 2.2 shows the ground state doublets and Zeeman splitting of erbium ions.

$^{167}Er^{3+}$ is the only stable isotope of erbium with a non-zero nuclear spin $I = 7/2$. For this isotope, due to hyperfine and quadrupole (i.e., second-order hyperfine) interactions with the crystal field [25], the electronic ground state doublets split further into 16 hyperfine sub-levels each with nuclear magnetic numbers $m_I = -7/2 \cdots 7/2$, as shown in Fig.2.2. This splitting happens even in the absence of an external magnetic field due to the low symmetry of the crystal.

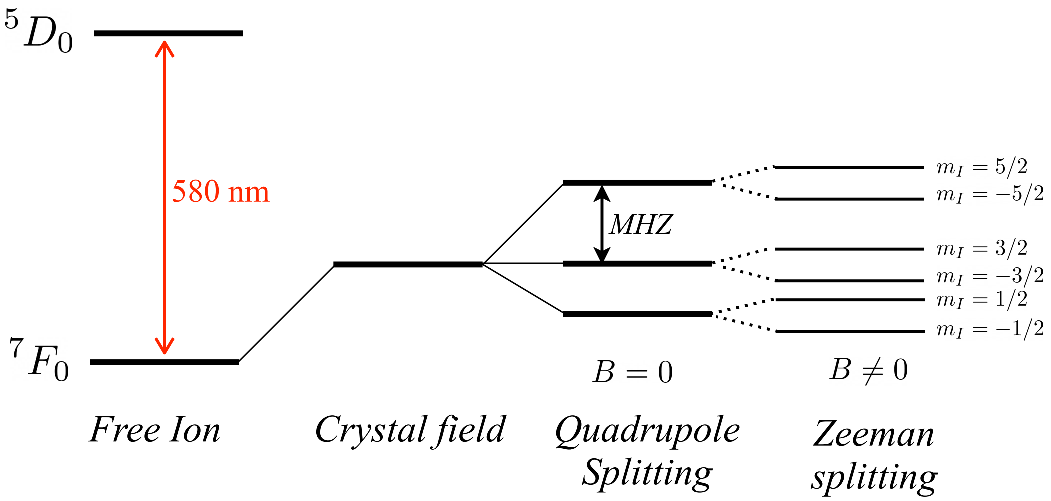

Figure 2.3: Ground state energy levels of europium ion doped a crystal.

Erbium is an attractive ion because of its optical transition frequency at the optimal wavelength for telecommunication fibers, i.e., the separation between the lowest doublets in the ground state and the lowest doublet of the excited state corresponds to a wavelength of ≈ 1536 nm [39].

2.1.4 Eu^{3+}:YSO

Europium is a non-Kramer rare-earth ion that has two isotopes, ^{151}Eu and ^{153}Eu, both with a $I = 5/2$ nuclear spin. Triple-positive europium ions have 6 electrons in their $4f$ shell. When doped into the YSO crystal, this ion also substitutes for Y^{3+} ions of the host. A free europium ion has a ground state energy level $^7F_0$. Therefore, after doping into a crystal, the crystal field will not split the ground state further. At zero external magnetic field, however, nuclear electric quadruple interactions split the crystal field singlets into three non-degenerate hyperfine levels in both of the ground and excited states. When an external magnetic field is imposed on the ion-doped crystal, doubly degenerate hyperfine energy levels split further into nuclear Zeeman levels [25]. The ground state energy levels of the europium ion are shown in Fig. 2.3.

Europium ions are known for their long coherence and relaxation times between the hyperfine levels. For example, when doped into the YSO crystal, the coherence time of this ion is measured to be six hours, and its relaxation time could be several days [40, 33]. Hence, this ion is an excellent candidate for storage applications. In section 3.3.2, we explain how to utilize europium ions as memory qubits to store entanglement.

Chapter 3

Paper 1: Quantum repeaters with individual rare-earth ions at telecommunication wavelengths

3.1 Preface

Global quantum networks will enable many applications from secure quantum communication to quantum internet in the long term. Here we propose an approach to quantum repeaters architecture as an essential ingredient of a future quantum network combining individual erbium and europium ions, which serve as spin-photon interfaces and long-term memories, respectively.

This work was done in collaboration with several co-authors. I contributed to this publication by proposing the quantum repeater scheme and performing the entanglement mapping and repeater rate calculations. I also wrote the first draft of the manuscript.

Quantum repeaters with individual rare-earth ions at telecommunication wavelengths

Quantum 2, 93 (2018)

F. Kimiaee Asadi, N. Lauk, S. Wein, N. Sinclair, C. O'Brien, and C. Simon

Institute for Quantum Science and Technology,and Department of Physics** & **Astronomy, University of Calgary, 2500 University Drive NW, Calgary, Alberta T2N 1N4, Canada

Abstract

We present a quantum repeater scheme that is based on individual erbium and europium ions. erbium ions are attractive because they emit photons at telecommunication wavelength, while europium ions offer exceptional spin coherence for long-term storage. Entanglement between distant erbium ions is created by photon detection. The photon emission rate of each erbium ion is enhanced by a microcavity with high Purcell factor, as has recently been demonstrated. Entanglement is then transferred to nearby europium ions for storage. Gate operations between nearby ions are performed using dynamically controlled electric-dipole coupling. These gate operations allow entanglement swapping to be employed in order to extend the distance over which entanglement is distributed. The deterministic character of the gate operations allows improved entanglement distribution rates in comparison to atomic ensemble-based protocols. We also propose an approach that utilizes multiplexing in order to enhance the entanglement distribution rate.

3.2 Introduction

Entanglement is a key requirement for many applications of quantum science. These include, for example, quantum key distribution [41], global clock networks [42], long-baseline telescopes [4], and the quantum internet [5, 6]. However, due to transmission loss the direct transmission of entanglement over distances of more than several hundred kilometers is practically impossible using current technology. The use of a quantum repeater has been suggested to reduce (or eliminate) the impact of loss in order to establish entanglement between distant locations. [7]. In many quantum repeater schemes, entanglement is first distributed between two locations that are separated by a short distance, referred to as an elementary link. Then, the range of entanglement is extended to successively longer distances by performing entanglement swapping operations between the entangled states that span each elementary link. Due to the availability and diversity of component systems and the strong light-matter coupling offered by atomic ensembles, many quantum repeater proposals use sources of entanglement, ensemble-based quantum memories, and linear optics-based entanglement swapping operations [18]. However, the success probability of linear optics-based entanglement swapping (without auxiliary photons) cannot exceed 50%, which has a compounding effect for more complex quantum networks. The use of auxiliary photons to improve the entanglement swapping probability is possible [43, 44], but adds complexity and compounds errors, thereby restricting their use in practice. Single-emitter-based quantum repeaters, on the other hand, offer the possibility to outperform ensemble-based repeaters by using deterministic swapping operations [45]. Impressive demonstrations of certain parts of a single-emitter quantum repeater schemes have been performed using atom-cavity systems [46, 47], color centers in diamond [24, 48], trapped ions [49, 50], donor qubits in silicon [51], as well as quantum dots [52, 53].

Over the years, crystals doped with rare earth (RE) ions have attracted considerable attention for their use in electromagnetic signal processing applications that range from quantum memories [54, 55] to biological imaging [56]. Narrow optical and spin homogeneous linewidths, their convenient wavelengths as well as their ability to be doped into solid-state crystals are some of the most desired properties of RE ions. Compared to nitrogen-vacancy centers in diamond [57] and quantum dots [58], they also exhibit smaller spectral diffusion [59, 60, 61], and have a reduced sensitivity to phonons.

Among the different RE ions, Er^{3+} is attractive due to its well-known optical transition (around 1.5 μm) in the conventional telecommunication wavelength window, in which absorption losses in optical fibers are minimal. Another unique aspect of certain RE ions is the presence of hyperfine levels that feature long lifetimes, which allows for long-term quantum state storage [62, 63, 64, 65]. In particular, a coherence lifetime of six hours was reported in a europium-doped yttrium orthosilicate crystal ($^{151}Eu^{3+}$:Y_2SiO_5) [40]. Motivated by these properties, we propose and analyze a quantum repeater protocol that is based on individual RE ions in which Er^{3+} ions are used to establish entanglement over elementary links and $^{151}Eu^{3+}$ ions are employed to store this entanglement.

One disadvantage of RE ions is their weak light-matter coupling, which has mostly precluded their use as single quantum emitters. However, optical detection and addressing of single RE ions has recently been shown by multiple groups [22, 66, 21, 23, 20]. Moreover, very recently Dibos et al. [66] demonstrated an enhancement in the emission rate of a single Er^{3+} ion in Y_2SiO_5 by a factor of more that 300 using a silicon nanophotonic cavity. Strong coupling of ensembles of Nd ions was previously demonstrated using nanophotonic cavities fabricated from Y_2SiO_5 [22] and yttrium orthovanadate [67] hosts. In light of these results, for our scheme we propose to couple single RE ions to a high-finesse cavity in order to enhance the light-matter coupling and thus to increase the collection efficiency as well as the indistinguishability of the emitted single photons.

The paper is organized as follows. In Sec. 3.3 we introduce our proposal and discuss the required components as well as the underlying principles. The entanglement distribution rates and possible implementations are discussed in Secs. 3.4 and 3.5. We conclude and provide an outlook in Sec. 3.6.

3.3 Quantum repeater protocol

The goal of our repeater scheme is to generate entanglement between nodes that are separated by a long distance by swapping entanglement that is established between nodes that are separated by smaller distances. Each node consists of a Y_2SiO_5 crystal containing an Er^{3+} ion that features an enhanced emission rate of its telecommunication transition due to a high-finesse cavity, and a nearby $^{151}Eu^{3+}$ ion that acts as a quantum memory due to its long spin coherence lifetime (note that, in principle, our proposed scheme is equivalent to use an external deterministic photon source in combination with single-particle quantum memories that can absorb and re-emit photons [68, 69]). Entanglement is then transferred, or gates are performed, between nearby atoms using electric dipole-dipole coupling [70, 71]. Our proposal has some similarity to a scheme that involves the excitation of electron spins in nitrogen-vacancy centers to generate entanglement between nodes, nuclear spins of carbon atoms for storage, and gates that are performed using a magnetic dipole-dipole coupling [72]. We emphasize that our (electric dipole) approach to implementing gates is quite different than previous approaches, as are many of the physical properties of the system (in addition to the emission wavelength).

In the first step, entanglement between pairs of neighboring Er^{3+} ions is created (see Fig.3.1 (a)) which illustrates this step for the i-th and i+1-th ions) by first creating local entanglement between the spin state of each ion and a spontaneously-emitted single photon. Then, by performing a joint Bell-state measurement (BSM) on photons that are spontaneously-emitted by neighboring Er^{3+} ions, the spin state of these ions is projected onto a maximally-entangled state. This procedure is the same as that used to create entanglement between two remote nitrogen-vacancy centers in diamond [73, 24].

Next, the quantum state of each Er^{3+} ion is mapped to a nearby $^{151}Eu^{3+}$ ion for storage by exploiting a non-vanishing permanent electric dipole moment, a common feature of many RE ions that are doped into solids. This mapping is achieved using a mutual electric dipole-dipole interaction between close-lying Er^{3+} and $^{151}Eu^{3+}$ ions. The small nuclear magnetic

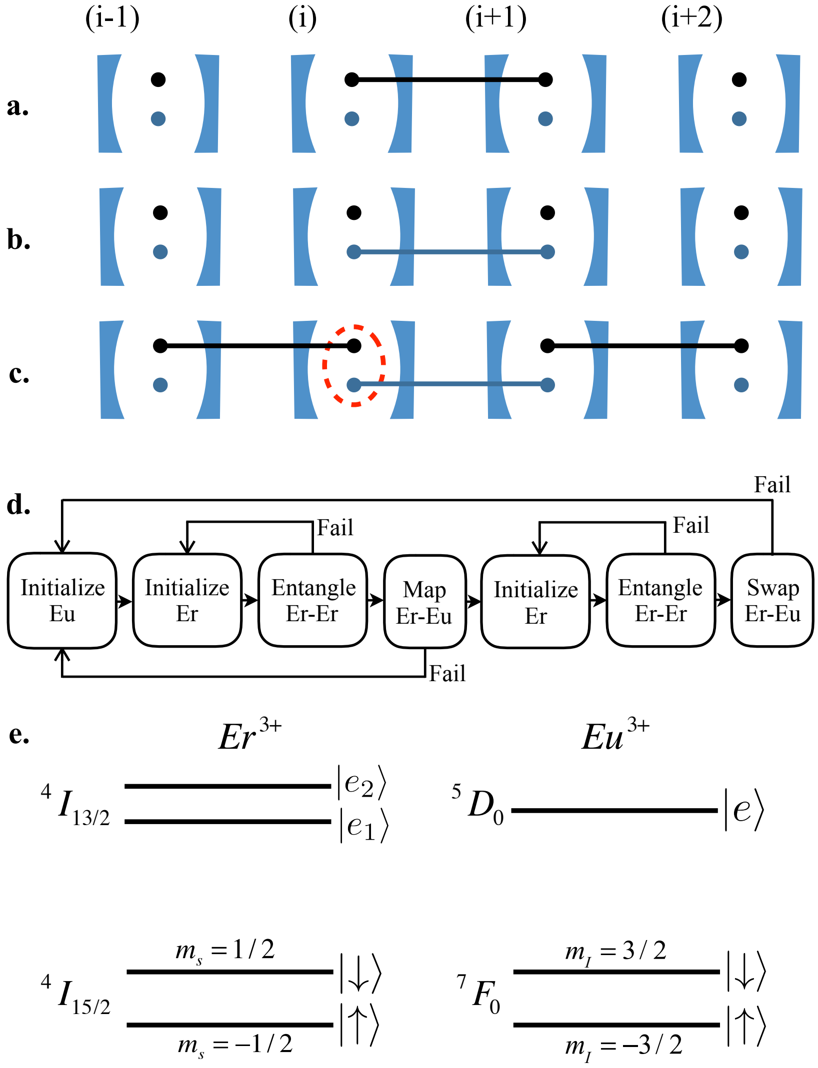

Figure 3.1: In each cavity, the blue and black dots represent individual $^{151}\mathrm{Eu}^{3+}$ and Er^{3+} ions, respectively. In order to distribute entanglement to the nodes that are situated at each end of a long channel, first a) entanglement between two neighboring Er^{3+} ions is created via the detection of two photons; b) the quantum state of each Er^{3+} ion is then mapped to a nearby $^{151}\mathrm{Eu}^{3+}$ ion using an electric dipole interaction; c) using two-photon detection, Er^{3+} ions are used again to establish entanglement between the other neighboring Er^{3+} ions. Finally, we extend the entanglement distance by performing entanglement swapping using an electric dipole interaction between nearby ions (red circle). d) Flow-chart that depicts our scheme. e) Simplified energy level structure of Er^{3+} and $^{151}\mathrm{Eu}^{3+}$ ions in the presence of an external magnetic field. The electronic Zeeman levels of Er^{3+}, and nuclear hyperfine levels of $^{151}\mathrm{Eu}^{3+}$, are split. We encode qubit states $|\uparrow\rangle$ and $|\downarrow\rangle$ in the $m_s = -\frac{1}{2}$ and $m_s = \frac{1}{2}$ $\left(m_I = -\frac{3}{2}\text{ and } m_I = \frac{3}{2}\right)$ levels for the Er^{3+} ($^{151}\mathrm{Eu}^{3+}$) ion, respectively.

moment of $^{151}\mathrm{Eu}^{3+}$ results in a magnetic-dipole coupling that is orders of magnitude smaller than the electric-dipole coupling, thus our scheme allows for much shorter gate durations in comparison to those based on magnetic interactions [72]. Another advantage of the proposed scheme is the ability to dynamically control the interaction optically by bringing the ion to the excited state and back to the ground state. This allows for the realization of deterministic two-qubit gate operations.

The mapping allows the Er^{3+} ions to be re-initialized so that new elementary links can be created between them. Fig.3.1(c) illustrates this processes for the (i − 1)th and (i)th nodes. Immediately after generating entanglement between (the other) neighboring Er^{3+} ions, the entanglement distance is extended by performing entanglement swapping between each of the closely-lying Er^{3+} and $^{151}\mathrm{Eu}^{3+}$ ions. As a result, the outer nodes becoming entangled. Fig. 3.1 (d) depicts a flow chart of our scheme. Photon loss and errors might cause some steps in the protocol to fail.

As will be discussed in Sec. II A–C, the generation of entanglement between Er^{3+} ions, the mapping of entanglement to the $^{151}\mathrm{Eu}^{3+}$ ions, and the entanglement swapping steps, all rely on the detection of single photons that are spontaneously emitted from the Er^{3+} ions. However, the lifetime of the $^4\mathrm{I}_{15/2} \leftrightarrow {}^4\mathrm{I}_{13/2}$ telecommunication transition of Er^{3+}:$\mathrm{Y}_2\mathrm{SiO}_5$ is relatively long $T_1 = 11.4$ ms [25] with radiative lifetime being even longer $T_{rad} = 54$ ms [74], which necessitates the need for a high-finesse cavity to enhance the emission rate. Nonetheless, the cavity will also significantly increase the probability of collecting the emitted photons as compared to emission into free space. We emphasize that the repetition rate of the protocol (i.e., the number of attempts of the protocol per unit time) is limited by the communication time between distant nodes (assuming the initialization time of the ions is negligible. See Sec.5.5 for more information), which means that there is no need for very fast emission. Next we discuss each of the steps of the protocol in detail.

3.3.1 Entanglement generation

Our scheme considers several remote cavities that each contain a single pair of close-lying Er^{3+} and $^{151}\mathrm{Eu}^{3+}$ ions. Note that there may be other RE ions within each cavity, but we assume that we can address a single such close-lying pair. See also section3.5 below. An externally-applied magnetic field splits the degenerate electronic ground levels of Er^{3+} via the Zeeman effect. We refer to the resultant $m_s = -\frac{1}{2}$ and $m_s = \frac{1}{2}$ Zeeman levels as the qubit states $|\uparrow\rangle$ and $|\downarrow\rangle$, respectively (see Fig. 3.1 (e)).

To generate entanglement between distant Er^{3+} ions that are separated by a long distance L_0, we follow the scheme of Barret and Kok [73, 24] (see also Fig. 3.1 (d)). First, each Er^{3+} ion is prepared in one of the qubit states (here $m_s = -\frac{1}{2}$; denoted $|\uparrow\rangle$). After this initialization step, a $\frac{\pi}{2}$ microwave (MW) pulse rotates each Er^{3+} ion into a superposition of $|\uparrow\rangle$ and $|\downarrow\rangle$ states. The application of a brief laser pulse that is resonant with the $|\uparrow\rangle \leftrightarrow |e_2\rangle$ transition, followed by spontaneous emission, will entangle each qubit state with the emitted photon number. That is, when the qubit state is $|\uparrow\rangle$ ($|\downarrow\rangle$) there will be 1 (0) emitted photon(s). The spontaneously-emitted photons are then directed to a beam splitter located in between the ions using optical fibers. A single-photon detection at one of the two beam splitter output ports projects the Er^{3+} ions onto an entangled state.

A possible loss in the fiber can lead to a situation where both Er^{3+} ions emit a photon but only one photon is detected while the other is lost. In this case, the ions are left in a product state rather than an entangled state. To exclude this possibility, immediately after the first excitation-emission step of each Er^{3+} ion, a π MW pulse inverts each qubit state. Then a second excitation pulse is applied. The detection of two consecutive single photons at the beam splitter will leave the qubits in an entangled state:

$$|\psi\rangle^{\pm}_{\mathrm{Er}} = \frac{1}{\sqrt{2}}(|\uparrow\downarrow\rangle \pm |\downarrow\uparrow\rangle). \tag{3.1}$$

Here the + (-) sign corresponds to the case in which the same (different) detector(s) received

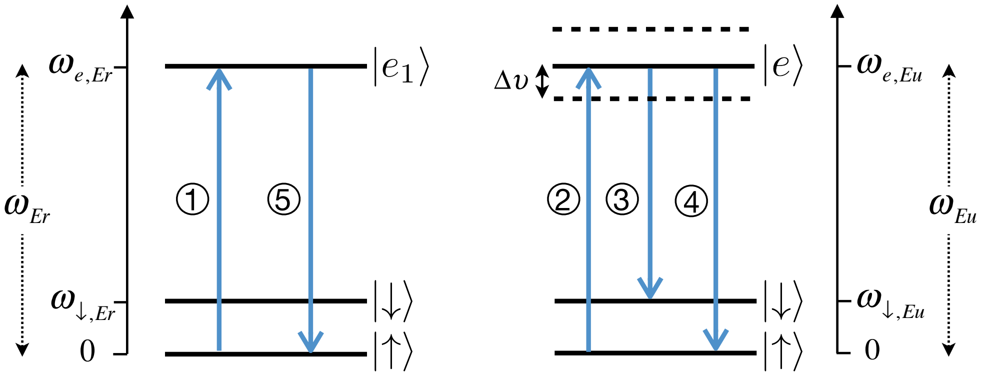

Figure 3.2: General pulse sequence of π-rotations to perform a controlled logic gate between nearby Er^{3+} and $^{151}Eu^{3+}$ ions. The numbers indicate the sequential time ordering of the pulses. For this gate, the Er^{3+} spin state acts as the control qubit and the $^{151}Eu^{3+}$ spin state acts as the target. A π pulse excites the Er^{3+} ion if it is in the state $|\uparrow\rangle$. When this occurs, pulses 2, 3 and 4 are not resonant with the $^{151}Eu^{3+}$ ion, leaving its state unaffected. Pulse 5 then brings the Er^{3+} ion back to its original state. On the other hand, when Er^{3+} is in the state $|\downarrow\rangle$, pulses 1 and 5 will be ineffective and hence it will remain in the ground state. Instead pulses 2, 3 and 4 will now be resonant with the $^{151}Eu^{3+}$ ion and (optically) swap its spin-state

a photon.

3.3.2 Controlled logic

After successful entanglement of the two distant Er^{3+} ions we transfer this entanglement to the neighboring $^{151}Eu^{3+}$ ions for a long-term storage. Efficient entanglement mapping between neighboring rare-earth ions can be employed by performing CNOT gate operations and single qubit rotations and read-out. Here we first explain the underlying mechanism and general scheme for how to implement a CNOT gate in our system, and in Sec.3.3.3 we will discuss in more detail how to swap entanglement between the ions using this gate.

Due to a lack of site symmetry when doped into a crystal, a RE ion can have a permanent electric dipole moment that is different depending on whether the ion is in its ground or optically excited state. The difference in the permanent dipole moments affects the optical transition frequency of other nearby RE ions via the Stark effect due to a modified local electric field environment. It is possible to dynamically control the shift in the transition frequency of one ion by optically exciting its neighboring ion. Based on this interaction, we can perform a controlled-NOT (CNOT) operation between nearby RE ions [75]. The modification of the transition frequency $\Delta\nu$ of a $^{151}\mathrm{Eu}^{3+}$ ion by an Er^{3+} ion due to the mutual electric dipole-dipole interaction is given by [76]:

$$\Delta\nu = \frac{\Delta\mu_{\mathrm{Er}}\Delta\mu_{\mathrm{Eu}}}{4\pi\epsilon\epsilon_0 h r^3}\left((\hat{\mu}_{\mathrm{Er}}\cdot\hat{\mu}_{\mathrm{Eu}}) - 3\,(\hat{\mu}_{\mathrm{Er}}\cdot\hat{r})\,(\hat{\mu}_{\mathrm{Eu}}\cdot\hat{r})\right), \tag{3.2}$$

where r is the distance between the ions, and $\Delta\mu$ is the change of the permanent electric dipole moment of each ion, h is the Planck constant, ϵ_0 is vacuum permittivity, and ϵ is the dielectric constant (note that we assume the effect of the Stark shift on the qubit states is negligible).

To perform a CNOT gate between the nearby Er (control) ion and Eu (target) ion, a sequence of five π pulses is applied (see Fig.(3.2)). First a π pulse is applied to the Er^{3+} ion on resonance with the $|\uparrow\rangle \leftrightarrow |e_1\rangle$ transition. From here, two cases must be considered: either the state of the Er^{3+} ion is $|\uparrow\rangle$ or it is $|\downarrow\rangle$.

If the Er^{3+} ion is in state $|\uparrow\rangle$, it will be excited by pulse 1. This changes the permanent electric dipole moment of the Er^{3+} ion, and thus its local electric field. Consequently, the transition frequency of the nearby $^{151}\mathrm{Eu}^{3+}$ ion will be shifted by $\Delta\nu$. For the case that this frequency shift is large enough (that is, the $^{151}\mathrm{Eu}^{3+}$ ion is sufficiently close to the Er^{3+} ion), the $^{151}\mathrm{Eu}^{3+}$ ion will be unaffected by pulses 2, 3 and 4, thereby remaining in its initial ground state (see Sec. 3.5.2 for more discussion). Finally, pulse 5 will bring Er^{3+} ion back to its initial state. Hence, in this case, the pulse sequence does not modify the initial state of the ion pair system.

On the other hand, if the Er^{3+} ion is initially in $|\downarrow\rangle$, then pulses 1 and 5 will have no effect on the Er^{3+} ion. Since the Er^{3+} ion will not be excited, optical pulses 2, 3 and 4 will be resonant with the transitions of the $^{151}\mathrm{Eu}^{3+}$ ion, and the pulse sequence will optically flip the two spin states of the $^{151}\mathrm{Eu}^{3+}$ ion.

3.3.3 Entanglement mapping and distribution

Both the ground and excited states of $^{151}\mathrm{Eu}^{3+}$ have three doubly-degenerate nuclear hyperfine levels. With the application of a magnetic field, each doublet $\left(m_I = \pm\frac{1}{2}, \pm\frac{3}{2}, \pm\frac{5}{2}\right)$ will be split. For our proposal, we denote the $m_I = -\frac{3}{2}$ and $\frac{3}{2}$ hyperfine levels [40] as the $^{151}\mathrm{Eu}^{3+}$ ion qubit states, $|{\uparrow}\rangle$ and $|{\downarrow}\rangle$, respectively (see Fig. 3.1 (e)). To map the state of each $^{168}\mathrm{Er}^{3+}$ ion onto a nearby europium ion, we first perform a CNOT gate between them. In our scheme, the $^{151}\mathrm{Eu}^{3+}$ ion is initially prepared in one of the ground state levels (here $|{\uparrow}\rangle$) using optical pumping. In this special case where the initial state of the europium is fixed, pulse 4 does not affect the system and can be neglected (i.e., we only need to transfer the population from the state $|{\uparrow}\rangle$ to $|{\downarrow}\rangle$ using pulses 2 and 3 if the state of the erbium is $|{\downarrow}\rangle$). This reduces the total gate time and improves the state mapping fidelity (see Sec. 3.5.2).

After considering the phases that are acquired by performing the CNOT gate on the ions in neighboring nodes (labeled here as 1 and 2 instead of (i) and (i + 1)), the final state is

$$|\psi\rangle^{\pm}_{\mathrm{Er,Eu}} = \frac{1}{\sqrt{2}}\left(|{\uparrow\downarrow}\rangle_{\mathrm{Er_1,Er_2}}\,|{\uparrow\downarrow}\rangle_{\mathrm{Eu_1,Eu_2}} \pm e^{i\phi}\,|{\downarrow\uparrow}\rangle_{\mathrm{Er_1,Er_2}}\,|{\downarrow\uparrow}\rangle_{\mathrm{Eu_1,Eu_2}}\right), \tag{3.3}$$

where

$$\phi = (\omega_{\downarrow,\mathrm{Er_2}} - \omega_{\downarrow,\mathrm{Er_1}})\tau + (\omega_{\mathrm{Eu_2}} - \omega_{\mathrm{Eu_1}})\tau_2 + (\omega_{\downarrow,\mathrm{Eu_2}} - \omega_{\downarrow,\mathrm{Eu_1}})(\tau_3 + \tau_4) +$$
$$k_{\downarrow\mathrm{Eu_1}} x_{\mathrm{Eu_1}} - k_{\downarrow\mathrm{Eu_2}} x_{\mathrm{Eu_2}},$$

and x is the distance the photon travels between each $^{151}\mathrm{Eu}^{3+}$ ion and the beam splitter, $k_{\downarrow\mathrm{Eu}} = \frac{\omega_{\downarrow,\mathrm{Eu}}}{c}$ is the wavenumber, τ_j is the time elapsed after application of the j^{th} pulse and τ is the total time duration that is needed to perform a CNOT gate. Since these phases are known, they can be compensated by applying local operations on the ions.

To conclude the mapping step, a $\frac{\pi}{2}$ microwave (MW) pulse is applied to rotate each Er^{3+} qubit. This is followed by a state measurement of both nearest-neighbor Er^{3+} ions, see also Sec. IV below. This projects the $^{151}\mathrm{Eu}^{3+}$ ions onto an entangled state. Depending on the outcome of these measurements, the entangled state between remote $^{151}\mathrm{Eu}^{3+}$ ions would be

$|\psi^+\rangle$ or $|\psi^-\rangle$. For example, in the case that we begin with $|\psi\rangle^+_{\mathrm{Er}}$ (given in Eq. 3.1), after performing the gate, MW rotation, and measurement, if both Er ions are found in the state $|\uparrow\rangle$, the entangled state between remote $^{151}\mathrm{Eu}^{3+}$ ions is $\frac{1}{\sqrt{2}}\left(|\uparrow\downarrow\rangle_{\mathrm{Eu_1,Eu_2}} + |\downarrow\uparrow\rangle_{\mathrm{Eu_1,Eu_2}}\right)$.

Once entanglement is established in neighboring elementary links, we perform a joint measurement on both ions at each intermediate node to distribute entanglement (see Fig. 3.1 (c)). In our scheme, it is possible to perform entanglement swapping deterministically using the permanent electric dipole-dipole interaction.

To perform the desired entanglement swapping, first a CNOT gate is applied in which Er^{3+} serves as the control qubit and $^{151}\mathrm{Eu}^{3+}$ as the target qubit (similarly as before). Here, both ions are in a superposition state and so all 5 pulses of the CNOT gate sequence are required. Then the Er^{3+} ion is measured in the diagonal (X) basis. Next, another CNOT operation is performed but now the target and control qubits are exchanged. Finally the Er^{3+} ion is measured in the logical (Z) basis. This 'reverse' CNOT gate is performed in order to avoid directly measuring the spin state of $^{151}\mathrm{Eu}^{3+}$ ion optically (the optical lifetime of $^{151}\mathrm{Eu}^{3+}$ is longer than the Er^{3+} spin coherence lifetime). Fig.(3.2) shows the pulse sequence needed to perform the first CNOT gate between the ions.

Based on the outcomes of the measurements on each Er^{3+} ion, the outer nodes will be projected onto one of the four Bell states. To be more precise, when performing entanglement swapping between $\mathrm{Er_i}$ and $\mathrm{Eu_i}$, if only one of the state measurements of $\mathrm{Er_i}$ is $|\uparrow\rangle$, the state of $\mathrm{Er_{i-1}}$ and $\mathrm{Eu_{i+1}}$ will project onto the $|\psi^+\rangle$ or the $|\psi^-\rangle$ Bell state. On the other hand, if both measurements of $\mathrm{Er_i}$ are $|\uparrow\rangle$ or both $|\downarrow\rangle$, the state will project onto the $|\phi^+\rangle$ or the $|\phi^-\rangle$ Bell state.

To verify or utilize the entanglement that is generated between the distant ions, a measurement must be performed on the endpoint nodes. Our protocol results in an entangled state of the Er^{3+} ion at the first node with the $^{151}\mathrm{Eu}^{3+}$ ion at the last node. A measurement of the Er^{3+} ion can be performed by direct optical excitation. A measurement of the $^{151}\mathrm{Eu}^{3+}$ ion spin can be performed by using the nearby Er^{3+} as a readout ion. This is done by mapping the $^{151}\mathrm{Eu}^{3+}$ state to Er^{3+} using gate operations (also see section 3.5.3 for further details).

3.4 Entanglement generation rates and multiplexing

In our scheme, the success probability of generating an entangled state between two neighboring Er^{3+} ions that are separated by a distance L_0 is $p_t = \frac{1}{2}\eta_t^2 p^2 \eta_d^2$, where $\eta_t = e^{-\frac{L_0}{2L_{att}}}$ is the transmission probability of a photon through optical fiber and $L_{att} \approx 22$ km (which corresponds to a loss of 0.2 dB/km), η_d is the detection efficiency, and p is the success probability of emitting a single photon into a cavity mode. Similarly, the success probability of mapping the state of an Er^{3+} ion onto a nearby $^{151}\mathrm{Eu}^{3+}$ ion is $p_m \approx p\eta_d$, because it requires one optical read-out of each Er^{3+} ion. Therefore, the average time to generate entanglement in an elementary link and perform the state mapping steps is

$$\langle T \rangle_{L_0} = \frac{L_0}{c}\left(\frac{1}{p_t p_m^2}\right), \tag{3.4}$$

where $c = 2 \times 10^8 \frac{\mathrm{m}}{\mathrm{s}}$ is the speed of light in fiber.

The average time that is required to distribute entanglement over two neighboring elementary links, which corresponds to a distance $L = 2L_0$, can be estimated as follows. First, entangled pairs of $^{151}\mathrm{Eu}^{3+}$ ions are generated over an elementary link and, once successful, Er^{3+} ions are then generated in a neighboring elementary link. Thus, the probability of establishing entanglement for both links is

$$p_0 = \left(\frac{1}{P_A} + \frac{1}{P_B}\right)^{-1}, \tag{3.5}$$

where $P_A = p_t$ and $P_B = p_t p_m^2$ represent the success probability of generating entanglement between Er^{3+} and $^{151}\mathrm{Eu}^{3+}$ ions, respectively. Then, entanglement is extended by performing a BSM between the close-lying Er^{3+} and $^{151}\mathrm{Eu}^{3+}$ ions at the center node. The success probability for the entanglement swapping step is $p_s \approx p^2\eta_d^2$ because it requires two optically-induced spin read-outs of an Er^{3+} ion. Consequently, the average time to distribute entanglement over a distance $2L_0$ is

$$\langle T\rangle_{2L_0} = \frac{L_0}{c}\frac{1}{p_0 p_s}. \tag{3.6}$$

Accordingly, the average time to distribute an entangled pair over a distance $L = 2^n L_0$, with n denoting the number of nesting levels, is [45, 18]:

$$\langle T\rangle_{L} = \left(\frac{3}{2}\right)^{n-1}\frac{L_0}{c}\frac{1}{p_0 p_s^n}. \tag{3.7}$$

The factor 3/2 for each of the next nesting levels, which is a good approximation for the exact result [18], can be understood in following way.

In contrast to the first nesting level, a successful entanglement distribution for higher nesting levels does not require waiting for a success in one link before the establishment of entanglement in another link can be attempted; rather, the establishment of entanglement can be attempted in both links simultaneously. For example, if a goal is to distribute entanglement over the distance $4L_0$, entanglement must be generated in two neighboring links each of length $2L_0$ before entanglement swapping is performed. If the average waiting time for a success in one link of length $2L_0$ is $\langle T\rangle_{2L_0}$, entanglement will be established in one of two links after $\langle T\rangle_{2L_0}/2$. Then, after another $\langle T\rangle_{2L_0}$ time duration, entanglement will be established in the other link. Hence, the average time to establish entanglement in the two neighboring links is $3\langle T\rangle_{2L_0}/2$. The same arguments hold for the next nesting levels, resulting in a factor $\left(\frac{3}{2}\right)^{n-1}$ for n nesting levels.

Multiplexing can be employed to significantly enhance the rate of entanglement distribution. Referring to the encoding of several individual qubits, each into their own distinguishable modes, multiplexing has been utilized for some quantum repeater proposals [18, 77, 78, 79]. As outlined in Fig. 3.3, we consider an array of m cavities in which each

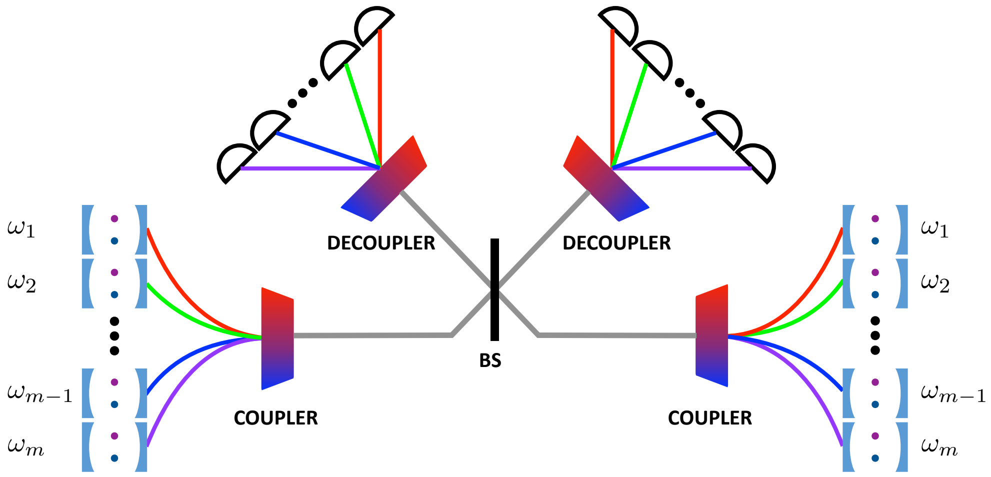

Figure 3.3: Our multiplexed scheme consists of 2^n+1 nodes that span the total channel distance L. Each node consists of an array of m cavities that emit photons which feature differing carrier frequencies. The carrier frequency of each photon is determined by a frequency translation device. A coupling element (COUPLER) ensures that each photon traverses a common channel to a Bell-state measurement station that consists of a beam splitter, decoupling element (DECOUPLER), and $2m$ single photon detectors. This set-up allows m entanglement generation protocols to be operated in parallel.

cavity emits a photon that features a distinguishable resonance frequency from the rest. This can be accomplished using frequency translation (see Sec. IV for more details). Using a coupler device, each photon is directed into a common fiber and is directed towards a BSM station that is composed of similarly-designed decouplers and single-photon detectors. Benefiting from the distribution of entanglement into m parallel modes, the probability that at least one entangled state is distributed over the entire channel is $1-(1-P_t)^m$, which can be made unity for a sufficiently high m. Here, $P_t = (2/3)^{n-1}p_0p_s^n$ is the success probability of distributing entanglement over a distance L using a qubit that is encoded into a single mode. Further details of this set-up are described in Sec.3.5.4.

The entanglement distribution rate of our scheme is plotted as a function of distance for $n = 3$ in Fig. 3.4 and compared to that employing the well-known DLCZ scheme [19], which uses ensemble-based memories, as well as that using direct transmission with a single-photon source which produces photons at 10 GHz. This 10 GHz photon rate is an optimistic rate for the direct transmission of photons. The rate that we assume for a single photon source is much faster than the rate for the proposed repeater because they have different limitations. Even though the photon rate of our scheme (which depends on the cavity characteristics and the optical lifetime of the Er^{3+} ion) is much lower, the time scale for the repeater is actually determined by the communication time L_0/c which is even longer. Note that the direct transmission scheme can also be interpreted as the Pirandola bound [80] for a repetition rate of 10/1.44=6.9 GHz. The performance of our protocol and the DLCZ scheme with $m = 100$ multiplexed channels is also shown Fig. 3.4. For more information on other approaches see Ref. [18]. In this review paper, the multiplexed DLCZ outperformed the other repeater protocols considered (see Fig. 18 of ref.[18]). As will be discussed in Sec. IV B, the use of even more than $m = 100$ parallel spectral channels is possible.

Fig. 3.4 shows that our use of deterministic gates is advantageous for the rate. The scaling of the DLCZ scheme with distance is slightly better than that of our scheme due to the requirement of detecting only one photon for each elementary entanglement creation step (rather than two photons for our scheme). However, this comes at the significant expense of requiring phase stabilization for the long-distance fiber links.

3.5 Implementation

For our scheme, we consider ion beam-milled Y_2SiO_5 photonic crystal cavity systems that have been weakly-doped with $^{168}Er^{3+}$ and $^{151}Eu^{3+}$ ions [81, 67, 82]. Co-doped crystals may be grown from the melt [82], or individual RE ions may be implanted into single Y_2SiO_5 crystals [83]. After a milling step, the output of the cavity can be coupled to an optical waveguide using, e.g., microscopy [84], bonding [85] or a pick-and-place technique [86], with the latter having been used to heterogeneously interface InAs/InP quantum dots with Si waveguides. Despite the lack of on-demand control of the position and relative orientation of each ion [83], a suitable Er-Eu ion pair can be identified by performing laser-induced fluorescence spectroscopy. This involves exciting each Er^{3+} ($^{151}Eu^{3+}$) ion with a laser and

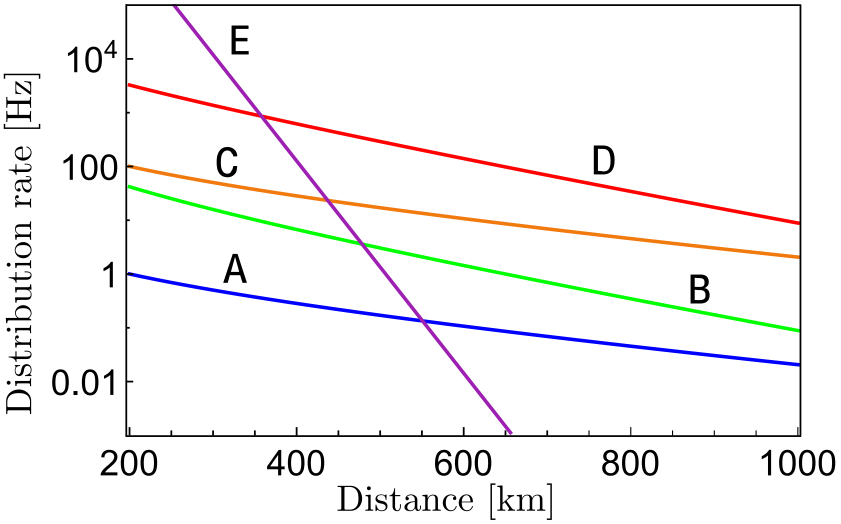

Figure 3.4: A comparison of the entanglement distribution rate for various schemes. Direct transmission scheme using a 10 GHz single-photon source (E) is compared with original DLCZ protocol (A) and our scheme (B) using 8 elementary links, each of length L_0. Also shown are the rates that correspond to the multiplexed versions of DLCZ (C) as well as our scheme (D) with $m = 100$ using the same number of elementary links. We assume that the detection efficiency and the success probability of emitting a single photon by an ion is $p = \eta_d = 0.9$, and in the case of DLCZ, a storage efficiency of $\eta_m = 0.9$. The repetition rate for each repeater protocol is set by the communication time L_0/c.

measuring the spectral shift of the resultant fluorescence from other $^{151}\text{Eu}^{3+}$ (Er^{3+}) ions due to the aforementioned electric-dipole coupling (see Sec. 3.3.3) [82]. Note that measurements using a 0.02%Er:1%Eu:Y_2SiO_5 bulk crystal revealed the optical transition frequency of sets of Er^{3+} ions that lie within approximately one nanometer from adjacent Eu^{3+} ions [82]. These results suggest that the transition frequencies of suitable Er-Eu pairs can be rapidly distinguished from other spectator ions.

The magnetic field applied in the $D_1 - D_2$ plane at 135 degrees relative to the D_1 axis results in the decay of the excited Er^{3+} ion back into the initial spin state via spontaneous emission with a probability of higher than 90%[87], and a Zeeman-level lifetime of about 130ms was measured for a magnetic field of 1.2 mT at 2.1 K temperature[87]. At large external magnetic fields of 1 T or more and temperatures below 3 K, one-phonon direct process is the dominant spin-relaxation mechanism and the temperature and magnetic field dependence of the relaxation rate could be approximated by [88]:

$$R(B) = R_0 + \alpha_D g^3 B^5 \coth(\frac{g\mu_B B}{2kT}) \tag{3.8}$$

where α_D is the anisotropic constant, μ_B is the Bohr magneton, and k is the Boltzmann constant. The field independent contribution R_0 can be attributed to cross-relaxations with paramagnetic impurities in the crystal and hence depends strongly on the crystal purity. Extrapolating from Refs [88, 87], the spin relaxation time would be about 40ms at 20mK for an external magnetic field of 1T at the 135° in $D_1 - D_2$ plane. At this magnetic field, however, the splitting of the Zeeman levels would be too large to address it with microwave pulses and optical Raman pulses should be applied instead.

For an ensemble-doped Er^{3+}:$\mathrm{Y_2SiO_5}$ the spin coherence lifetime at mK temperatures and external magnetic fields of few hundred mT can be as short as $\sim 7\ \mu$s [89]. However, for an ensemble-doped Er^{3+}:$\mathrm{Y_2SiO_5}$ crystal spin flip-flop processes are one of the main sources of decoherence, the spin coherence lifetime of a single Er^{3+} ion in $\mathrm{Y_2SiO_5}$ is largely determined by spin-spin magnetic dipole interactions. The magnetic moments of the constituent spins of $\mathrm{Y_2SiO_5}$ are small: $-0.137\mu_N$, $-0.5\mu_N$, and $-1.89\mu_N$ for ^{89}Y, ^{29}Si, and ^{17}O respectively. Compared to yttrium ions, ^{29}Si and ^{17}O have low isotopic natural abundances, so we assume the contribution of these isotopes to be negligible and only consider the Er-Y interactions. In a large enough magnetic field compared to the Er-Y coupling strength, the magnetic moment of Er^{3+} will detune the closest-proximity Y ions from resonance with those further away. This well-known effect referred to as the “frozen core” has been observed and results in weaker decoherence of the Er^{3+} ion by nearby Y ions [90, 91, 35]. Hence, for a single $^{168}\mathrm{Er}^{3+}$ in $\mathrm{Y_2SiO_5}$, the presence of a strong magnetic field (a few hundred milli-tesla up to a few tesla) may increase the spin coherence lifetime into the milliseconds range. Note that, further increasing the external field will increase the splitting between the Zeeman levels, making the system more subject to photon assisted transitions (which in turn decreases both of the spin coherence time and lifetime of the ion). However, for the $^{167}\text{Er}^{3+}$ (the only stable isotope of the erbium with non-zero nuclear spin), increasing the external magnetic field will increase the nuclear spin coherence time by freezing out the electron spin dynamics [92]. Therefore, one can use nuclear spin states of the $^{167}\text{Er}^{3+}$ as qubit states with relatively high coherence time (see chapter 5).

To further increase the spin coherence lifetime, dynamical decoupling immediately after the second optical excitation step is necessary. While this has not been demonstrated in $\text{Er}^{3+}\text{:Y}_2\text{SiO}_5$, it is a widely-employed method, and has been used to extend coherence lifetimes in Ce-doped yttrium aluminum garnet [93] as well as nitrogen-vacancy centers [72].

Spin polarization of up to 90% in $\text{Er}^{3+}\text{:Y}_2\text{SiO}_5$ has been realized by using stimulated emission and spin-mixing methods [94]. The efficiency of spin polarization is determined by a competition between decay of the ground-level population relative to the optical pumping efficiency of the ion. Since the latter will be enhanced due to the cavity-induced decay rate, we expect a near-unity Er^{3+}-spin polarization for our scheme. Since the ground state lifetime of $^{151}\text{Eu}^{3+}$ is several hours, spin polarization can be achieved by performing continuous optical pumping of all but one of the ground states.

In Y_2SiO_5, RE ions can occupy two crystallographically inequivalent sites with C_1 symmetry. Due to this lack of symmetry, the orientation of the dipole moments and their magnitudes, and hence their dipole-dipole interaction strengths, are unknown. Previous measurements of the linear Stark shift of $\text{Er}^{3+}\text{:Y}_2\text{SiO}_5$ [95] allow the calculation of the projection of the electric-dipole moment difference onto the direction of the externally applied electric field to be approximately $0.84 \times 10^{-31}\text{Cm}$ [96]. The dipole moment difference for $^{151}\text{Eu}^{3+}\text{:Y}_2\text{SiO}_5$ can be as high as $\Delta\mu_{Eu} = 0.81 \times 10^{-31}\text{Cm}$ [97], resulting in the shift of the transition frequency of 10 and 0.01 MHz for $r_{ij} = 1$ and 10 nm, respectively. As a comparison, the magnetic dipole-dipole interaction between Er^{3+} magnetic moment, which can be as high as $\mu_{Er} = 14.65\ \mu_B$ [98], and ^{151}Eu magnetic moment with its intrinsic value of $\mu_{Eu} = 3.42\ \mu_N$ [99] is much weaker and amounts to 363 and 0.363 kHz for $r_{ij} = 1$ and 10 nm, respectively.

3.5.1 Cavity

The cavity serves three main purposes in this proposal. It improves the quantum efficiency, enhances the single-photon indistinguishability, and increases the rate of Er^{3+} emission. To achieve these benefits, the cavity must provide a significant Purcell enhancement to the $|e_2\rangle \longrightarrow |\uparrow\rangle$ transition of Er^{3+}.

In the context of RE ions, Purcell factors of several hundred have been achieved [66, 22], and up to 10^3 seems to be a reasonable goal [100]. The Purcell factor can be written: $P = (\gamma/\gamma_r)C$, where $1/\gamma$ is the excited state lifetime, γ_r is the radiative decay rate, and C is the cavity cooperativity. The cavity-enhanced quantum efficiency (probability of emitting a photon into the cavity mode) is then given by: $p = \eta P/(1 + \eta P)$, where $\eta = \beta\gamma_r/\gamma$ is the Er^{3+} spin-conserving quantum efficiency, and β is the probability of an excited ion to relax into the initial spin state via the spontaneous emission. For Er^{3+}:$\mathrm{Y_2SiO_5}$, $\beta = 0.9$, $\gamma = 2\pi \times 14$ Hz, and $\gamma_r = 2\pi \times 3$ Hz [74], resulting in $\eta = 0.19$. For $P = 100$, a cavity quantum efficiency of $p = 0.95$ is possible. Increasing the Purcell factor to $P = 1000$ allows $p = 0.995$.

The single-photon indistinguishability is a metric that quantifies the quality of interference between photons that originate from the same quantum emitter. Without a cavity, the single-photon indistinguishabilty can be defined as $I_1 = T_2/2T_1 = \gamma/(\gamma + 2\gamma^\star)$ where $\gamma^\star$ is the optical pure dephasing rate [101] (i.e., the pure dephasing can degrade the coherence of the emitted photons by the ion). The dephasing can be caused by processes that change the optical transition energy on a timescale that is faster than the decay rate of the transition. For an ensemble of 0.0015% Er^{3+}:$\mathrm{Y_2SiO_5}$ we have $T_1 = 11.4$ms [25] and optical T_2 is around 200μs at 1 T and a temperature of a few K [102]. This would imply $I_1 = 0.009$ without a cavity, which would require significant spectral filtering to achieve successful entanglement generation. For a single-photon emitter inside a cavity, one can derive the degree of indistinguishability of photons from the probability of two-photon interference in a Hong-Ou-Mandel experiment as [101, 103]

$$I_1 = \frac{\int_0^\infty \int_0^\infty |\langle \hat{a}^\dagger(t+\tau)\,\hat{a}(t)\rangle|^2 dt d\tau}{\int_0^\infty \int_0^\infty \langle \hat{a}^\dagger(t+\tau)\,\hat{a}(t+\tau)\rangle\,\langle \hat{a}^\dagger(t)\,\hat{a}(t)\rangle\, dt d\tau}, \tag{3.9}$$

where $\hat{a}$ ($\hat{a}^\dagger$) is the cavity mode annihilation (creation) operator. Therefore, in our system, the Purcell-enhanced single-photon indistinguishability can be approximated by: $I_1 = (1+\eta P)/(\zeta + 1 + \eta P)$, where $\zeta = 2T_1/T_2^\star = 2T_1/T_2 - 1$ is the dephasing ratio. Therefore, with Purcell factors $P = 1000$ and $P = 20,000$ the single-photon indistinguishability would be $I_1 = 0.63$ and $I_1 = 0.97$, respectively. In a large magnetic field, however, $T_2 = 4$ ms was measured at a few K [102]. For an ensemble-doped Er^{3+}:$\mathrm{Y_2SiO_5}$ spin flip-flop processes are the dominant decoherence mechanism and applying a large magnetic field can freeze these processes. As a result we have a long optical T_2. The flip-flop process can also be suppressed by reducing the Er^{3+} concentration. Therefore in our system, where we assume very low dopant concentration, we still can expect to have optical coherence times of the order of a few ms even at lower magnetic fields (hundreds of mT). With $P = 100$ and $T_2 = 4$ms, $I_1 = 0.82$ is possible, which could be further improved by attempting to spectrally filter the narrow $2\pi \times 1.4$ kHz bandwidth photons. With $P = 1000$, $I_1 = 0.98$ could be achieved without spectrally filtering the $2\pi \times 14$ kHz photons (corresponding to a duration of 11 μs).

3.5.2 CNOT gate

To perform the CNOT gate, it is necessary for Er^{3+} to remain excited for a time that is long enough to apply three π-pulses to $^{151}\mathrm{Eu}^{3+}$. This implies that each Er^{3+} ion must be excited to a different Zeeman level ($|e_1\rangle$) than the level that is coupled to the cavity ($|e_2\rangle$). This can be done if the Zeeman splitting between $|e_1\rangle$ and $|e_2\rangle$ is much larger than the cavity linewidth. In this section, for Er^{3+} we use $|e\rangle_{\mathrm{Er}} = |e_1\rangle$.

To quantify the fidelity of the CNOT gate and state transfer procedures, we use a model nine-level system where both Er^{3+} and $^{151}\mathrm{Eu}^{3+}$ are represented by three-level systems with two lower-energy spin states ($|\uparrow\rangle$, $|\downarrow\rangle$) and a single excited state ($|e\rangle$) (see Fig. 3.2). We use the dipole-interaction Hamiltonian:

$$H = \Delta\nu \sigma^{+}_{\mathrm{Er}\uparrow}\sigma^{-}_{\mathrm{Er}\uparrow}\sigma^{+}_{\mathrm{Eu}\uparrow}\sigma^{-}_{\mathrm{Eu}\uparrow} + \sum_{k,l}\frac{\Omega_{k,l}}{2}\left(\sigma^{+}_{k,l}+\sigma^{-}_{k,l}\right), \tag{3.10}$$

where $\Delta\nu$ is the dipole interaction strength and $\Omega_{k,l}$ is the Rabi frequency for transition $\{k,l\}$ for $l \in \{\uparrow,\downarrow\}$, $k \in \{\mathrm{Er},\mathrm{Eu}\}$. Without loss of generality, we choose $\Delta\nu > 0$ and $\Omega_{k,l} > 0$. The master equation is

$$\dot{\rho} = -i[H,\rho] + \sum_{k,l}\gamma_{k,l}\mathcal{D}(\sigma^{-}_{k,l})\rho + \frac{\gamma^{\star}_{k}}{2}\mathcal{D}(\sigma^{+}_{k,l}\sigma^{-}_{k,l})\rho + \sum_{k}\frac{\chi_k}{2}\mathcal{D}(\sigma_{z,k})\rho, \tag{3.11}$$

where $\mathcal{D}(\sigma)\rho = \sigma\rho\sigma^{\dagger} - \sigma^{\dagger}\sigma\rho/2 - \rho\sigma^{\dagger}\sigma/2$. The operators are defined as $\sigma^{+}_{k,l} = |e\rangle\langle l|_k$, $\sigma^{-}_{k,l} = (\sigma^{+}_{k,l})^{\dagger}$, and $\sigma_{z,k} = (|\uparrow\rangle\langle\uparrow|_k - |\downarrow\rangle\langle\downarrow|_k)/2$. The rate $\gamma_{k,l}$ is the decay rate for transition $\{k,l\}$, $\gamma^{\star}_{k}$ is the optical pure dephasing rate, and χ_k is the spin decoherence rate for ion k.

To solve for the Er-Eu state after applying the five-pulse CNOT gate sequence, we first assume that each π-pulse is a square pulse and that they are applied to the system sequentially with no time delay between pulses. In this case, the time taken to apply each π-pulse is given by $T_{k,l} = \pi/\Omega_{k,l}$. We also assume that $\Omega_{k,l}$ and $\Delta\nu$ are much larger than any dissipative rate so that we can treat the dissipation perturbatively.

We then define the zero-order (reversible) superoperator $\mathcal{L}_0$ where $\mathcal{L}_0\rho = -i[H,\rho]$. Then we define the first-order (irreversible) perturbation superoperator $\mathcal{L}_1$ as $\mathcal{L}_1\rho = \dot{\rho} - \mathcal{L}_0\rho$. From this, we define the rotation superoperator $\mathcal{R}_{k,l}(\theta)$ corresponding to the pulse where $\Omega_{k,l} \neq 0$ and $\Omega_{k',l'} = 0$ for all $k' \neq k$ and $l' \neq l$. This superoperator is given by

$$\mathcal{R}_{k,l}(\theta) = e^{\mathcal{L}_0\frac{\theta}{\Omega_{k,l}}}\left[1 + \int_0^{\frac{\theta}{\Omega_{k,l}}} d\tau e^{-\mathcal{L}_0\tau}\mathcal{L}_1 e^{\mathcal{L}_0\tau}\right], \tag{3.12}$$

which is accurate to first-order in $\gamma_{k',l'}, \gamma^{\star}_{k'}, \chi_{k'} \ll \Omega_{k,l}, \Delta\nu$ for all k' and l'.

To simulate the entanglement swapping between $^{151}\mathrm{Eu}^{3+}$ and Er^{3+}, we begin with an initial superposition state ρ_0 where $|\psi\rangle = (|\uparrow\rangle + |\downarrow\rangle)_{\mathrm{Er}}(|\uparrow\rangle + |\downarrow\rangle)_{\mathrm{Eu}}$ and $\rho_0 = |\psi\rangle\langle\psi|$. Then after applying the CNOT pulse scheme, the final state is

$$\rho = \mathcal{R}_{\mathrm{Er},\uparrow}(\theta)\mathcal{R}_{\mathrm{Eu},\uparrow}(\theta)\mathcal{R}_{\mathrm{Eu},\downarrow}(\theta)\mathcal{R}_{\mathrm{Eu},\uparrow}(\theta)\mathcal{R}_{\mathrm{Er},\uparrow}(\theta)\rho_0,$$

where ideally $\theta = \pi$; however, we set $\theta = \pi + \epsilon$ to simulate a π-pulse with a small rotation deviation $|\epsilon| \ll \pi$ caused by a non-ideal pulse area. The total time taken to apply this sequence is $T_{\mathrm{gate}} = 2T_{\mathrm{Er},\uparrow} + 2T_{\mathrm{Eu},\uparrow} + T_{\mathrm{Eu},\downarrow}$.

For a high fidelity gate, the pulse durations must be small so that the gate is fast and qubit states do not dephase during the sequence. This favors larger Rabi frequencies. On the other hand, it is also necessary that the three Eu pulses do not excite the $^{151}\mathrm{Eu}^{3+}$ spin state if Er^{3+} is excited. One way to achieve this is to set $\Omega_{\mathrm{Eu},l}$ to satisfy the detuning condition $\Omega^2_{\mathrm{Eu},l}/\Delta\nu^2 \ll 1$ so that there is little chance for off-resonant excitation. However, since $\Delta\nu$ cannot be arbitrarily large (the separation between Er and Eu cannot be arbitrarily small), the detuning criteria necessitates a very slow gate, which cannot provide a high fidelity.

Alternatively, the detuning condition can be circumvented if $\Omega_{\mathrm{Eu},l}$ is chosen so that the Eu pulses perform an effective 2π rotation on the Eu spin state when Er is excited, but still perform a π-pulse when Er is not excited. This can be accomplished by requiring that $\Omega_{\mathrm{Eu},l}$ satisfies the effective Rabi frequency relation $\sqrt{\Delta\nu^2 + \Omega^2_{\mathrm{Eu},l}} = 2\Omega_{\mathrm{Eu},l}$. This sets $\Omega_{\mathrm{Eu},l} = \Delta\nu/\sqrt{3}$. As a consequence of fixing the Rabi frequency, an accurate characterization of the dipole interaction strength for each Er-Eu pair is necessary to achieve a high fidelity. This is because any mischaracterization $\delta\nu$ from the true value $\Delta\nu - \delta\nu$ will cause a deviation from the desired 2π rotation. To account for this, we also consider a perturbation of the fidelity for deviation $\Delta\nu \to \Delta\nu - \delta\nu$ where we assume $|\delta\nu| \ll \Delta\nu \propto \Omega_{k,l}$.

The effective 2π pulse leaves a relative phase between the $^{151}\mathrm{Eu}^{3+}$ ground-state spins of $\varphi = -\pi(2-\sqrt{3})/2$. If Er^{3+} is in $|\downarrow\rangle$, then only π-rotations are applied to $^{151}\mathrm{Eu}^{3+}$. Hence, in this case, there is no acquired relative phase from the detuned pulses. However, if the state is $|\uparrow\downarrow\rangle$, $^{151}\mathrm{Eu}^{3+}$ will be affected by the third pulse performing an effective 2π rotation, and so $|\uparrow\downarrow\rangle$ will acquire a relative phase of φ. Likewise, if the state is $|\uparrow\uparrow\rangle$, $^{151}\mathrm{Eu}^{3+}$ will be affected by the second and fourth pulses performing an effective 2π rotation, and so $|\uparrow\uparrow\rangle$ will acquire a relative phase of 2φ. Hence, in the absence of dissipation and using perfect square π-pulses, the expected final state is

$$|\psi_f\rangle = \frac{1}{2}\left(|\downarrow\downarrow\rangle + |\downarrow\uparrow\rangle + e^{i\varphi}|\uparrow\downarrow\rangle + e^{i2\varphi}|\uparrow\uparrow\rangle\right) \tag{3.13}$$

Since the expected acquired phase $\varphi = -\pi(2-\sqrt{3})/2$ is known, and independent of the dipole interaction strength $\Delta\nu$, it can be tracked or corrected and so we use $|\psi_f\rangle$ as the final state when calculating the fidelity.

We use the above expressions for ρ and $|\psi_f\rangle$ to compute the fidelity $F_{\mathrm{CNOT}} = |\langle\psi_f|\,\rho\,|\psi_f\rangle|$. For simplicity, we choose to set $\Omega_{\mathrm{Er},l} = \Omega_{\mathrm{Eu},l} = \Omega = \Delta\nu/\sqrt{3}$; however, $\Omega_{\mathrm{Er},l}$ is not restricted by the dipole interaction strength and could be made larger than Ω to further decrease the total gate time and increase fidelity. The solution F_{CNOT} to first-order in $\gamma_{k,l}, \gamma_k^\star, \chi_k \ll \Omega \propto \Delta\nu$ for all k, l and second-order in $\epsilon \ll \pi$ and $\xi = \delta\nu/\Delta\nu \ll 1$ is

$$F_{\mathrm{CNOT}} \simeq 1 - T_{\mathrm{CNOT}}\Gamma - \epsilon^2 - \frac{13\pi}{16}\epsilon\xi - \frac{43\pi^2}{128}\xi^2 \tag{3.14}$$

Here $T_{\mathrm{CNOT}} = 5\pi/\Omega = 5\pi\sqrt{3}/\Delta\nu$ is the total gate time and Γ is the effective dissipation rate:

$$\Gamma \simeq \frac{1}{80}\left[31\gamma_{\mathrm{Er}} + 17\gamma_{\mathrm{Er}}^\star + 8\chi_{\mathrm{Er}} + 11\gamma_{\mathrm{Eu}} + 8\gamma_{\mathrm{Eu}}^\star + 17\chi_{\mathrm{Eu}}\right], \tag{3.15}$$

where we define $\gamma_k = \gamma_{k\uparrow} + \gamma_{k\downarrow}$. To obtain the reverse CNOT fidelity, it is only necessary to swap the dissipative parameters for Er^{3+} and $^{151}\mathrm{Eu}^{3+}$.

For a dipole interaction strength of $\Delta\nu = 2\pi \times 46$ kHz corresponding to an Er-Eu separation of about 6 nm, the CNOT gate time can be as small as $T_{\mathrm{CNOT}} = 94\,\mu$s. To estimate the fidelity, we use the parameters $\gamma_{\mathrm{Er}} = 2\pi \times 3$ Hz, $\gamma^{\star}_{\mathrm{Er}} = 2\pi \times 8$ Hz, $\gamma_{\mathrm{Eu}} = 2\pi \times 1.3$ Hz, and $\gamma^{\star}_{\mathrm{Eu}} = 2\pi \times 19$ Hz estimated from Ref. [74]; also $\chi_{\mathrm{Er}} \simeq 2\pi \times 80$ Hz and $\chi_{\mathrm{Eu}} \simeq 0$. In this case, for a small π-pulse over-rotation of $\epsilon \simeq \pi/64$ and a dipole interaction strength over-estimation of 2% ($\xi \simeq 0.02$), the fidelity is $F_{\mathrm{CNOT}} = 0.986$. The reverse CNOT fidelity is slightly smaller due to the spin dephasing of Er: $F_{\text{R-CNOT}} = 0.980$.

This method can also be used to compute the fidelity of state transfer from Er^{3+} to $^{151}\mathrm{Eu}^{3+}$. In this case, we remove the fourth pulse ($\mathcal{R}_{\mathrm{Eu},\uparrow}$) and use the initial state $|\psi\rangle = (|\uparrow\rangle + |\downarrow\rangle)_{\mathrm{Er}} |\uparrow\rangle_{\mathrm{Eu}}$. The expected final state is $|\psi_f\rangle = |\downarrow\downarrow\rangle + e^{i2\varphi} |\uparrow\uparrow\rangle$. In this case, the fidelity is similar to the CNOT gate (Eq. (3.14)):

$$F_{\mathrm{ST}} \simeq 1 - T_{\mathrm{ST}}\Gamma - \frac{5}{8}\epsilon^2 - \frac{3\pi}{16}\epsilon\xi - \frac{21\pi^2}{256}\xi^2 \tag{3.16}$$

where $T_{\mathrm{ST}} = 4\pi/\Omega = 4\pi\sqrt{3}/\Delta\nu$. The effective dissipation rate was found to be very similar to Eq. (3.15), but depends less strongly on $^{151}\mathrm{Eu}^{3+}$ dissipation:

$$\Gamma \simeq \frac{1}{80}\left[29\gamma_{\mathrm{Er}} + 16\gamma^{\star}_{\mathrm{Er}} + 9\chi_{\mathrm{Er}} + 11\gamma_{\mathrm{Eu}} + 7\gamma^{\star}_{\mathrm{Eu}} + 9\chi_{\mathrm{Eu}}\right]. \tag{3.17}$$

Using the same parameters as above, the fidelity of state transfer is $F_{\mathrm{ST}} = 0.989$.

3.5.3 State measurement

The spin readout of Er^{3+} is performed by optical excitation. Since only the $|\uparrow\rangle - |e_2\rangle$ transition is coupled to the cavity, optical excitation will result in a presence or absence of a photon emission depending on the state of the Er^{3+} ion. The measurement of the $^{151}\mathrm{Eu}^{3+}$ ion can be performed through its nearby Er^{3+} ion as a readout ion, provided that the Er^{3+} ion is initially prepared in the $|\uparrow\rangle$ state. Performing spin readout of the $^{151}\mathrm{Eu}^{3+}$ ion in the Z basis is then achieved by optically exciting the $^{151}\mathrm{Eu}^{3+}$ ion ($|\uparrow\rangle$ to $|e\rangle$ transition) followed by exciting the Er^{3+} ion ($|\uparrow\rangle$ to $|e_1\rangle$ transition). The Er^{3+} ion will excite to $|e_1\rangle$ (remain in ($|\uparrow\rangle$) if the state of the $^{151}\mathrm{Eu}^{3+}$ ion is $|\downarrow\rangle$ ($|\uparrow\rangle$) due to the permanent electric dipole-dipole interaction which shifts the Er^{3+} optical resonance. To readout in the X basis, a $\frac{\pi}{2}$ MW pulse should be applied to the $^{151}Eu^{3+}$ ion in order to rotate the ground-state spins before the optical excitation step.

State measurement of each Er^{3+} ion requires the detection of an emitted photon. Due to the Purcell effect, as discussed in Sec. 3.5.1, the emission of a single photon from the ion is highly preferential into the cavity mode. For a high quality cavity, the probability that the photon emits into the cavity tends to unity. Therefore, the detection probability will be limited by coupling losses and single photon detectors, which can have detection efficiency as high as 95%, as has been demonstrated in superconducting detectors [104, 105]. To do better than this limit, it is necessary to pump the Er^{3+} ion into a cycling transition such that many photons will be emitted by the cavity, and eventually detected. Using such a cycling transition, detection probability can be as high as 98.7% [100]. The detection efficiency is not 100% in this case because there is a small chance for the ion to decay into a different state than the initial state, thus ending the photon cycling [106]. This chance grows linearly with the number of cycles before detection.

3.5.4 Spectrally-multiplexed implementation

Our spectral multiplexing scheme relies on the possibility that many spectral channels can be operated in parallel. This requires that, in one node, different cavities emit photons that feature different carrier frequencies. This can be accomplished by frequency translation. Noise-free translation over tens of gigahertz [79, 107] can be achieved by using voltage-swept, commercially-available, waveguide electro-optic modulators that can be optically-coupled to the output port of each cavity. After frequency translation, the output can be coupled to a common spatial mode (e.g. a waveguide or fiber) by using a tunable ring resonator filter that features resonance linewidths as narrow as 1 MHz [108]. Arrayed waveguides or fiber-Bragg gratings may also be used, however they are bulky and their resonance linewidths are currently not at the MHz level. The modulators and filters may be fabricated on a single chip, offering the possibility of low loss and up to 10^4 spectral modes. The Bell-state measurement station consists of a beamsplitter, two sets of ring resonator filters which are identical to that used at the nodes, and an array of superconducting nanowire-based photon detectors, chosen due to their combination of high-efficiency and low noise properties [105].

3.6 Conclusion

Our proposal for a quantum repeater which is based on individual RE ions promises the deterministic establishment of high-fidelity entanglement over long-distances at a rate which exceeds that corresponding to the direct transmission of photons. Our scheme utilizes some of the most desirable features of RE-ion-doped crystals, specifically emission within the low-loss telecommunications window (Er^{3+}) and the hours-long nuclear spin coherence lifetime ($^{151}\mathrm{Eu}^{3+}$:$\mathrm{Y_2SiO_5}$) that is needed to perform long-distance transmission and swapping of entanglement. Moreover, control logic gates between close-lying individual $^{151}\mathrm{Eu}^{3+}$ and Er^{3+} ions allow the quasi-deterministic swapping of entanglement by means of a permanent electric dipole-dipole interaction. The multiplexed version of our scheme improves the entanglement distribution rate by at least a factor of 100 over that of the single-mode version of our repeater.

So far, we have only discussed a single entanglement generation attempt per communication time L_0/c. However, one can also trigger the source many times in every communication time interval, i.e., temporal multiplexing [18]. In this case, we require memories that can store multiple temporal modes [109]. In general, the best-case scenario is to use both temporal and spectral multiplexing in the same system.

Looking forward, it is interesting to consider the possibility of employing individual $^{167}\mathrm{Er}^{3+}$ ions instead of Er-Eu ion pairs for a telecommunication wavelength quantum repeater. In the presence of strong magnetic fields, $^{167}\mathrm{Er}^{3+}$:$\mathrm{Y_2SiO_5}$ features a nuclear spin coherence lifetime in the one-second range [92], allowing the possibility of entanglement generation and storage using the same ion, pairs (or small ensembles) of Er^{3+} ions. One of the main challenges for future work in this direction is to devise a scheme whereby individual Er^{3+} ions may be addressed and coupled within a single cavity. This could be achieved by using magnetic dipole-dipole interactions in a similar spirit to what has been demonstrated using nitrogen vacancy centers and carbon spins in diamond [72], or by using the cavity mode to mediate the interaction. Another interesting direction is the possibility of long-term storage using host-ion spins such as yttrium in Y_2SiO_5 [110].

ACKNOWLEDGMENTS

The authors would like to thank M. Afzelius, P. Barclay, P. A. Bushev, C. W. Thiel and W. Tittel for helpful discussions. This work was supported by the Natural Sciences and Engineering Research Council (NSERC) through its Discovery Grant program, the CREATE grant 'Quanta', and through graduate scholarships, by the University of Calgary through an Eyes High postdoctoral fellowship, by Alberta Innovates Technology Futures (AITF) through graduate scholarships, and by the Defense Advanced Research Projects Agency (DARPA) through the Quiness program (Contract No. W31P4Q-13-1-0004).

Chapter 4

Paper 2: Cavity-assisted controlled phase-flip gate

4.1 Preface

Future quantum networks will require interfaces between stationary qubits (e.g. spins in solids) and flying qubits (photons), as well as the ability to perform gates between the stationary qubits in the individual network nodes. In order to be efficient, spin-photon interfaces typically require high-quality cavities. It is then very natural to ask whether such cavities can also be used to mediate gates between spins. Here, we propose three different methods for realizing such gates. We focus on schemes that do not require the strong coupling regime, which opens up their utilization in a wider range of physical systems.

In this work, I conceived the idea, and building on earlier work, selected the three schemes to develop. The first two authors jointly advanced the theory and wrote the first draft of the manuscript.

Cavity-assisted controlled phase-flip gate

Phys. Rev. A 102, 013703 (2020)

F. Kimiaee Asadi, S. Wein, and C. Simon

Institute for Quantum Science and Technology,and Department of Physics* & *Astronomy, University of Calgary, 2500 University Drive NW, Calgary, Alberta T2N 1N4, Canada

Abstract

Cavity-mediated two-qubit gates, for example between solid-state spins, are attractive for quantum network applications. We propose three schemes to implement a controlled phase-flip gate mediated by a cavity. The main advantage of all these schemes is the possibility to perform them using a cavity with high cooperativity, but not in the strong coupling regime. We calculate the fidelity of each scheme in detail, taking into account the most important realistic imperfections, and compare them to highlight the optimal conditions for each scheme. Using these results, we discuss which quantum system characteristics might favor one scheme over another.

4.2 Introduction

Building a global quantum network or "quantum internet" [5, 6, 111] will enable many applications such as secure communication, enhanced sensing, and distributed quantum computing. Establishing a quantum network requires interfaces between stationary qubits (e.g. superconducting qubits, trapped ions, or spins in solids) and flying qubits (photons). The various quantum internet applications also require local gates between stationary qubits. For example, two-qubit gates are necessary for entanglement storage and swapping for quantum repeater protocols [18], and a basic operation for generating and manipulating entangled states for quantum computation [112]. So far, to perform two-qubit gates, different types of interactions including magnetic and electric dipole-dipole interactions [113, 75, 114] and phonon-mediated couplings [115] have been employed.

To be efficient, interfaces between stationary and flying qubits often need cavities. It is natural to explore if cavity-assisted interactions can also be used to perform two-qubit gates [116, 117, 118, 119, 120]. Using cavity quantum electrodynamics (QED), one can perform two-qubit phase-flip gates between qubits encoded in two modes of the electromagnetic field (photonic qubits) [121], between a quantum system and a cavity mode [122], and also between two individual quantum systems (e.g., ions, atoms etc.) inside a cavity [116, 117, 118]. Of those, the latter is of great interest due to its wide-range of applications. Unlike electric and magnetic dipole-dipole interactions, cavity-mediated interactions do not require quantum systems to be very close to each other.

Although the strong coupling regime of cavity QED has been observed for some solid-state systems such as quantum dots [123, 124, 125] and superconducting qubits [126], achieving a true strong coupling regime with vacuum Rabi splitting remains an outstanding challenge in other solid-state systems that are quite attractive from a quantum internet perspective. For example, rare earth ions (REIs) are attractive because of their convenient wavelengths, narrow optical transitions, and long coherence times, but have weak dipoles [127]. Defect centers in diamond are also attractive because of their excellent coherence (even at room temperature in the case of the NV center); however, fabricating high-quality cavities in diamond is not straightforward.

In this paper, we propose three different cavity mediated approaches to perform controlled phase-flip gates between two individual quantum systems. All of these schemes require only a high cooperativity cavity-emitter system. Therefore, even using materials or quantum emitters that are unlikely to reach the strong coupling regime, the following schemes are applicable. We calculate explicit solutions for the fidelity of these gates in detail and compare their advantages and disadvantages.

In the first scheme, we propose to perform two-qubit controlled phase-flip gates by scattering a single photon off of a cavity-qubit system. This approach has been discussed before in the context of a strong coupling regime [116, 128], but not in the so-called 'bad cavity' regime that we also consider. For the second scheme, we discuss how to use a dissipative cavity coupling to perform a controlled phase-flip gate via a virtual photon exchange. This interaction has been explored in microwave and optical systems [129, 119, 117], but to our knowledge, the specific details and fidelity calculations for a cavity QED phase-flip gate using this interaction are not presented in the literature. Finally, inspired by a proposed scheme in Ref. [118], we propose a third scheme that can perform a controlled phase-flip gate between qubits with unequal optical transition frequencies using a Raman-assisted virtual photon exchange interaction. In addition, for each scheme, we provide for the first time a complete picture of the high-fidelity regime of operation that takes into account finite cavity cooperativity, and we compute each scheme's robustness to qubit decoherence and imprecise control of detunings. Moreover, we compare these three schemes using a consistent approach to highlight the advantages and disadvantage of each scheme in the context of their application to different solid-state emitters.

4.3 Methods

The starting point for each scheme is to consider a pair of individual quantum systems (A and B) placed in a cavity. For each system, we employ two of the lowest energy levels (e.g., hyperfine or Zeeman levels) to encode one qubit within states $|\uparrow\rangle$ and $|\downarrow\rangle$. Depending on the protocol we also require one or two additional excited or ground states. In all of these schemes we require a high-cooperativity cavity $C = 4g^2/\kappa\gamma \gg 1$ where κ is the cavity decay rate, g is the cavity coupling rate, and γ is decay rate of the quantum system excited state(s). High cooperativity is achievable in both the bad-cavity regime where $\kappa \gg g \gg \gamma$ and the strong-coupling regime where $g \gg \kappa \gg \gamma$.

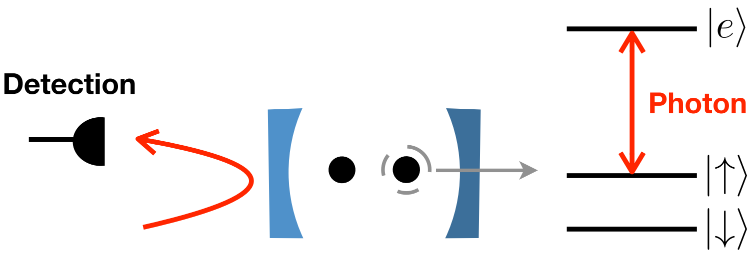

Figure 4.1: Scheme illustration and energy level diagram of both quantum systems in the photon scattering scheme. The $|\uparrow\rangle$ and $|\downarrow\rangle$ ground states represent the qubit states and $|e\rangle$ is the excited state of the system. The $|\uparrow\rangle$–$|e\rangle$ transition of both systems is resonant with the cavity whereas the $|\downarrow\rangle$–$|e\rangle$ transition is either far-detuned or uncoupled from the cavity.

4.3.1 Photon scattering

Cavity-assisted photon scattering is one way to perform a controlled phase-flip gate between qubits in the same cavity by scattering a single photon off of the qubit-cavity system and detecting it. Although it is not necessary to detect the photon after reflection, doing so can herald the gate, which drastically improves the gate fidelity for realistic single photon sources.

Performing a phase-flip gate using this scheme has already been discussed in the strong coupling regime [116, 128, 130, 131]. Moreover, based on this scheme, a theoretical investigation of the entanglement generation has been studied [132]. Here, for the first time we present the fidelity calculation for this gate in both bad-cavity and strong-coupling regimes. We also analyze infidelity due to possible spectral wandering of the incident single photon and imperfect quantum systems resonance conditions.

In this scheme, we use a single sided cavity and two 3-state quantum systems with a Λ system (i.e., two ground states $|\uparrow\rangle$ and $|\downarrow\rangle$ and an excited state $|e\rangle$). For both quantum systems, the $|\uparrow\rangle$–$|e\rangle$ transition is resonant with the cavity and the $|\downarrow\rangle$–$|e\rangle$ transition does not interact with the cavity, as shown in Fig. 4.1. In systems where both qubit states can interact with the excited state for the same polarization (e.g., rare earth ions), $|\downarrow\rangle$–$|e\rangle$ should be far-detuned from the cavity frequency [100].

We denote the state of the photon by $|p\rangle$. If both qubits are in the state $|\downarrow\rangle$, the photon enters and then exits the cavity unhindered. This reflection of the photon from inside the cavity causes the joint state of the qubit-photon system to acquire a π-phase shift. On the other hand, if either or both of the qubits are in the state $|\uparrow\rangle$, the cavity mode becomes modified and the photon will not be impedance matched. In this case, the cavity acts as a mirror and the photon does not enter the cavity but reflects from the out-coupling mirror of the cavity. Under the correct cavity and photon conditions, the phase of the qubit-photon system remains unchanged for these three cases.

This phase-flip gate can also be described by a unitary operator $U = e^{i\pi|\downarrow\downarrow\rangle\langle\downarrow\downarrow|\otimes|p\rangle\langle p|}$, meaning that there would be a phase-flip in the system only if both ions are in the state $|\downarrow\rangle$. As a result the states $|\uparrow\uparrow\rangle|p\rangle$, $|\uparrow\downarrow\rangle|p\rangle$ and $|\downarrow\uparrow\rangle|p\rangle$ remain unchanged but $|\downarrow\downarrow\rangle|p\rangle$ changes to $-|\downarrow\downarrow\rangle|p\rangle$. At the end, we can detect the reflected photon to herald the gate.

In the strong coupling regime, the impedance mismatch can be described simply by a frequency shift (vacuum Rabi splitting). However, in the bad cavity regime, the resonant systems cause a phase shift that destroys the constructive interference of the photon inside the cavity within a narrow frequency window; therefore, the photon will not enter the cavity (see ref. [100]).

In the regime where $C \gg 1$ we find that the total gate fidelity of this scheme is well-approximated by

$$F_{\text{gate}} = 1 - \frac{5}{4C} - \frac{\delta_p^2 + \sigma_p^2}{8\gamma^2 C^2}\left[11 - 20\left(\frac{2g}{\kappa}\right)^2 + 12\left(\frac{2g}{\kappa}\right)^4\right] - \frac{(\delta_{\epsilon_A} - \delta_{\epsilon_B})^2}{4\gamma^2 C} - \Gamma T, \tag{4.1}$$

where σ_p is the spectral standard deviation of an incident photon with a Gaussian intensity profile, δ_p is the mean cavity-photon detuning, and δ_{ϵ_k} for $k \in \{A, B\}$ is the detuning of the k^{th} system's optical transition from the cavity resonance. We also introduce Γ as the effective qubit decoherence rate that is a weighted average of decoherence rates from system-specific processes that are smal2l compared to cavity dissipation and spontaneous emission. Here $T = 8\pi\sqrt{2\ln 2}/\sigma_p$ is the gate time, which we define to be twice the FWHM duration of the photon for this scheme. This effective rate is at least given by the qubit decoherence time: $\Gamma \geq 1/2T_2$. Equation (4.1) is valid to first order in C^{-1} and ΓT; and to second order in $\delta_{\epsilon_k}/\gamma$, $\delta_p/\gamma C$, and $\sigma_p/\gamma C$. See Appendices 4.6 and 4.6.3 for detailed calculations.

The second term in equation (4.1) shows the infidelity due solely to a finite cavity cooperativity, the third term shows the spectral mode matching sensitivity of the incident single photon, the fourth term captures the degradation when either of the quantum systems $|\uparrow\rangle$ transitions are not exactly resonant with the cavity, and the last term captures a linear scaling due to a small effective qubit decoherence rate.

For shorter photons, the larger bandwidth can exceed the narrow spectral range over which the destructive interference occurs within the cavity. This degrades the fidelity of the phase-flip gate. On the other hand, for very long photons, the gate becomes so slow that qubit decoherence can dominate and degrade the gate fidelity. These two competing processes limit high-fidelity operation to a range of gate times (see Fig. 4.2.a) with an optimal gate time given by $T_o^3 = (352\pi^2 \ln 2)/(\gamma^2 C^2 \Gamma)$ in the bad-cavity limit.

We find that there is a non-trivial relationship between the regime of operation and robustness against photon detuning (see Fig. 4.2.b and 4.2.c). In addition, since the photon detuning infidelity scales as δ_p^2, averaging the fidelity over a Gaussian spectral wandering profile with standard deviation $\sigma^\star$ simply results in $\sigma^\star$ replacing δ_p in equation (4.1). Hence, the effect of photon detuning captured in equation (4.1) and shown in Fig. 4.2 also demonstrates the effect of random spectral wandering of the incident photon.

Far in the bad cavity regime where $g/\kappa \ll 1$, the system is very resilient to photon detuning and finite bandwidth effects. In this regime, the spectral window where a phase flip can occur is small, scaling by g^2/κ [100]; however, mode matching so that the photon enters the cavity when the quantum systems are off resonant is relatively simple to accomplish due to the large cavity bandwidth. In contrast, in the strong-coupling regime where $g/\kappa \gg 1$, the spectral window for the phase flip is larger, but mode matching becomes much more difficult to achieve and so the fidelity is more sensitive to the photon spectral properties.

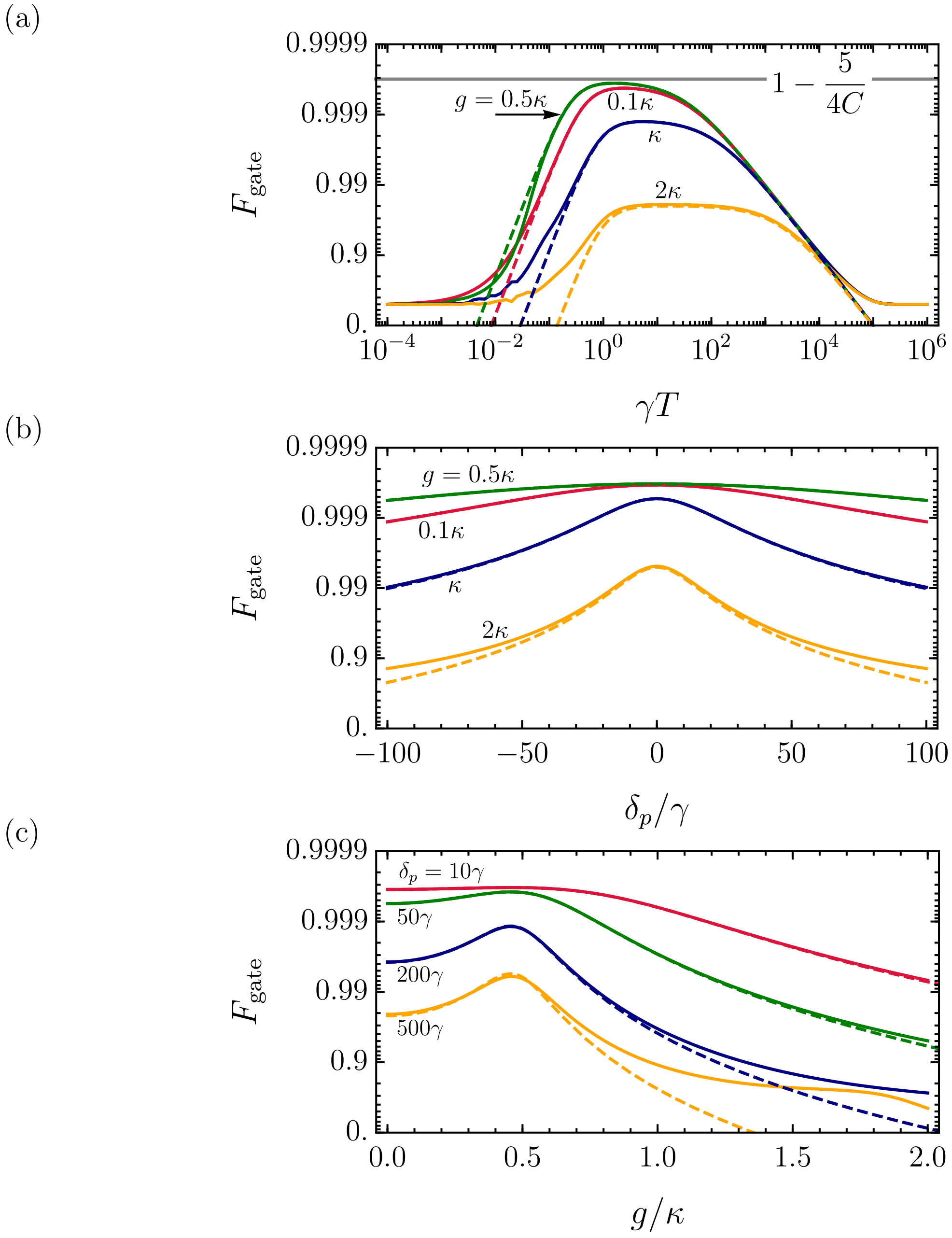

Figure 4.2: Fidelity of the photon scattering phase gate as a function of (a) the gate time T, (b) the photon-cavity detuning δ_p for a given cavity regime, and (c) the cavity regime for a given photon-cavity detuning. Here we set the cavity cooperativity to $C = 4000$, quantum system detunings to $\delta_{\epsilon_A} = \delta_{\epsilon_B} = 0$, the effective dephasing to $\Gamma/\gamma = 10^{-5}$, and for (a): $\delta_p = 30\gamma$, and (b, c): $T = 2/\gamma$. The ratio of cavity coupling rate g to cavity dissipation rate κ gives the regime of operation with $g/\kappa \ll 1$ and $g/\kappa \gg 1$ indicating the bad-cavity and strong-coupling regimes, respectively. The solid lines show the numerical solution without expanding around small $\delta_p/\gamma C$, $\sigma_p/\gamma C$, and large C. The dashed lines correspond to the analytic approximation given by equation (4.1). For the numerical simulation, we assume that the effective decoherence rate Γ exponentially degrades the coherence of the reduced spin density matrix as opposed to using the linear correction as in the analytic approximation.

Although the bad-cavity regime is surprisingly robust against spectral wandering, photon detuning, and finite bandwidth effects, we find that the most robust regime is the so-called 'critical regime' where $2g \simeq \kappa$ [133] (see Fig. 4.2.b).

4.3.2 Simple virtual photon exchange

Another type of a cavity-assisted interaction between qubits can be achieved by the exchange of virtual cavity photons when the quantum systems' optical transitions are resonant but dispersively coupled to a cavity mode [129, 119, 117]. Using this interaction, we provide a description of how to perform a phase-flip gate as well as detailed calculations on the fidelity of the gate.

For our analysis, we consider two 4-state quantum systems; each system has two ground states $|\downarrow\rangle$ and $|\uparrow\rangle$ and two excited states $|e_1\rangle$ and $|e_2\rangle$. Since the systems' optical transitions are dispersively coupled to a symmetric cavity, there is no energy exchange with the cavity. To have a phase-flip gate between qubits, first we bring the $|\uparrow\rangle$–$|e_2\rangle$ transition of the first system into resonance with the $|\downarrow\rangle$–$|e_1\rangle$ transition of the second system using a magnetic flux or an AC Stark pulse [119, 134]. Next, a π-pulse (P_1) is applied to one of the systems to bring it to the excited state, as shown in Fig. 4.3.a. After a time delay, another optical π-pulse (P_2) is applied to bring the excited quantum system back to its initial state.

To understand how this process performs a phase flip gate between qubits, we have shown the level diagram of the two-qubit system in the product space in Fig. 4.3.b. If the two-qubit system is in the state $|\downarrow\downarrow\rangle$ or $|\downarrow\uparrow\rangle$, pulses P_1 and P_2 are ineffective and hence the qubits will be unaffected. If the state is $|\uparrow\uparrow\rangle$, then P_1 excites system A to the excited state $|e_2\rangle$. So far as the splitting between the states $|e_2 \uparrow\rangle$ and $|\uparrow e_2\rangle$ is large enough, there will be no interaction between them. Applying another π-pulse P_2 to system A, will then return it to the ground state and leave $|\uparrow\uparrow\rangle$ unaffected. However, if the state is $|\uparrow\downarrow\rangle$, after exciting system A to the excited state, the degenerate states $|e_2 \downarrow\rangle$ and $|\uparrow e_1\rangle$ interact via the virtual exchange of a cavity photon which adiabatically performs a π phase flip on the state. At the end, the

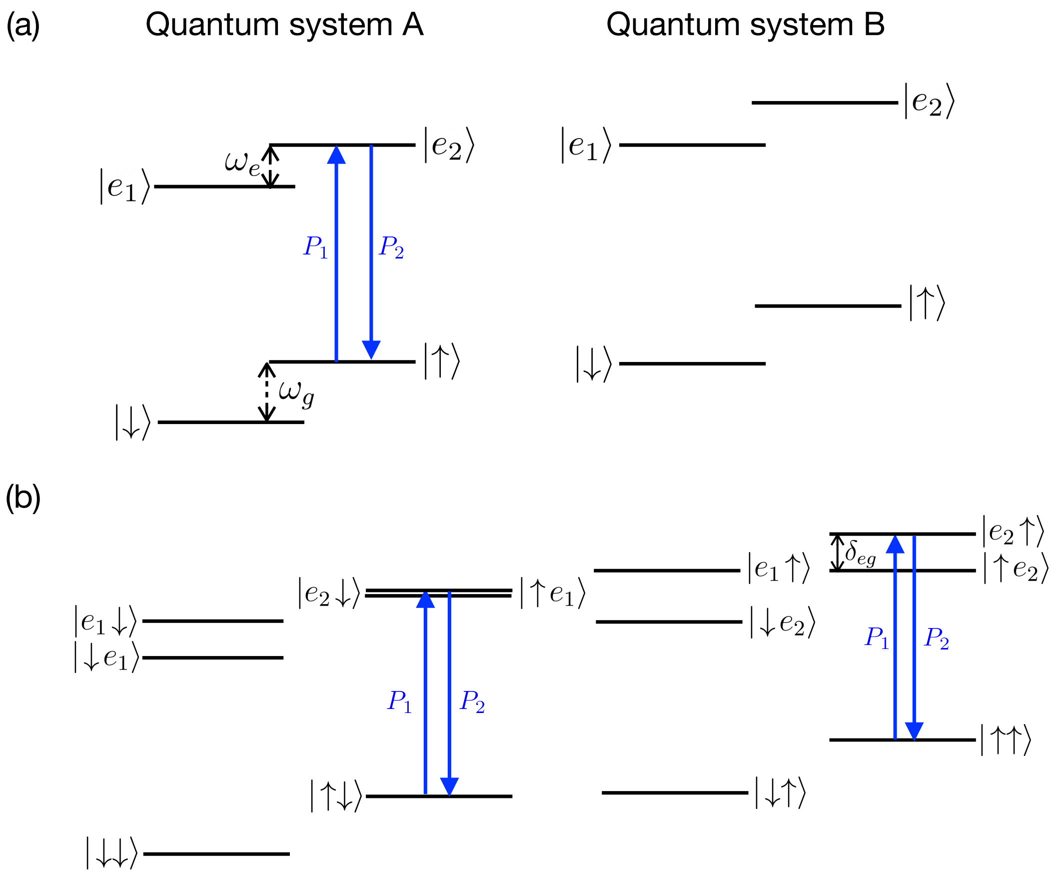

Figure 4.3: (a) Energy level diagram of the simple virtual photon exchange phase gate. The $|\uparrow\rangle$–$|e_2\rangle$ transition of system A is brought into resonance with the $|\downarrow\rangle$–$|e_1\rangle$ transition of system B. To perform a phase-flip gate, we apply a pair of optical π pulses with a time delay on system A. b) Level diagram in the product space. The splitting between $|e_2\uparrow\rangle$ and $|\uparrow e_2\rangle$ states is equal to the difference between the ground and excited states splittings $\delta_{eg} = |\omega_e - \omega_g|$. The interaction between the states $|e_2\downarrow\rangle$ and $|\uparrow e_1\rangle$ performs a phase flip gate in the system. However, high fidelity can only be achieved when δ_{eg} is large enough so that the $|e_2\uparrow\rangle$ and $|\uparrow e_2\rangle$ states are not interacting.

optical pulse P_2 brings system A back to its initial state but with a relative phase $-|{\uparrow\downarrow}\rangle$.

The virtual interaction can be controlled by detuning the quantum system optical frequencies away from each other. That is, when the detuning between the optical transitions is much more than the cavity coupling strength, the qubit-qubit interaction can be made negligible and the gate will not be successful.

We define $\Delta_k = \omega_C - \omega_k$ as the detuning between the cavity and the $|{\uparrow}\rangle \rightarrow |e_2\rangle$ transition of the k^{th} quantum system. In the high cooperativity regime, the cavity detuning $\Delta = \Delta_A \simeq \Delta_B + \delta_{eg}$ dictates the gate fidelity F_{gate} and gate time $T = \pi\Delta/g^2$, where $\delta_{eg} = |\omega_{\text{e}} - \omega_{\text{g}}|$ is the difference between ground-state and excited state splittings. If the detuning is too small, the excited system can emit a photon into the cavity mode, which can subsequently decay. Hence the fidelity becomes limited by the cavity dissipation rate κ. However, if the detuning is too large, T is also large, which causes the system to relax before the gate is complete. Hence the fidelity becomes limited by γ. The maximum gate fidelity of the simple virtual photon exchange is achieved between these extremes at a detuning of $2\Delta = \kappa\sqrt{C}$ (see Fig. 4.4) and is well-approximated by

$$F_{\max} = 1 - \frac{\pi}{\sqrt{C}} - \frac{3\pi^2}{32}\left[\left(\frac{T_o\Delta_\epsilon}{2\pi}\right)^2 + \left(\frac{2\pi}{T_o\delta_{eg}}\right)^2 - \frac{12}{C}\right] - \Gamma T_o, \tag{4.2}$$

where $T_o = 2\pi/\gamma\sqrt{C}$ is the optimal gate time, Γ is the effective decoherence rate, and $\Delta_\epsilon = \omega_B - \omega_A - \delta_{eg}$ is a small detuning between the systems' optical transitions. Equation (4.2) is valid to first order in C^{-1} and ΓT_o, and also to second order in $T_o\Delta_\epsilon$ and $(T_o\delta_{eg})^{-1}$. See Appendices 4.6 and 4.6.3 for detailed calculations and the expression for F_{gate} that includes dependence on Δ and κ.

From the above solution we can note that the maximum fidelity is ultimately limited by the cavity cooperativity. However, we can also see that this maximum can only be reached if the optical transition of the systems are resonant to within a precision dictated by the inverse gate time: $\Delta_\epsilon \ll 2\pi T_o^{-1}$. In addition, there should not be any other optical transitions

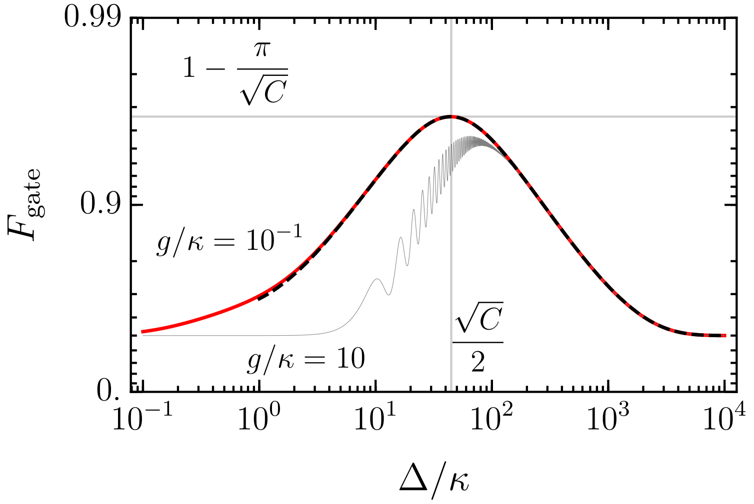

Figure 4.4: Fidelity of the simple virtual photon exchange phase gate F_{gate} as a function of the cavity detuning Δ/κ. The analytic solution in the adiabatic regime given in Appendix B (black dashed curve) matches closely with the numerically exact solution in the weak coupling regime (solid red curve) with $g/\kappa = 10^{-1}$ and accurately predicts the maximum fidelity $F_{\max}$ at $2\Delta = \kappa\sqrt{C}$. High fidelity can also be achieved if the system is not too far into the strong-coupling regime (gray solid curve) with $g/\kappa = 10$, but it is less optimal. Here $\Delta_\epsilon = 0$, $\delta_{eg} \to \infty$, and $C = 8000$.

coupled to the cavity within $\delta_{eg} \gg 2\pi T_o^{-1}$. If either or both of these conditions are violated, it may be beneficial to choose a detuning that better optimizes the gate fidelity.

This simple virtual photon exchange scheme operates most optimally in the bad-cavity regime. In the strong-coupling regime, Rabi oscillations begin to occur when the cavity detuning is not large enough. This effect pushes the optimal detuning further away and forces the fidelity to be more limited by decay from the excited state (see Fig. 4.4).

4.3.3 Raman virtual photon exchange

A controlled phase-flip gate can also be performed between distant qubits by virtual excitation of the cavity mode via a Raman coupling. Performing two-qubit gates using the Raman coupling has been discussed in Ref. [135] for quantum dots. Later, Ref. [118] proposed an improved version of the latter scheme for trapped ions, which is more efficient in terms of the number of operations. However, there is a challenge related to shelving the qubit state in

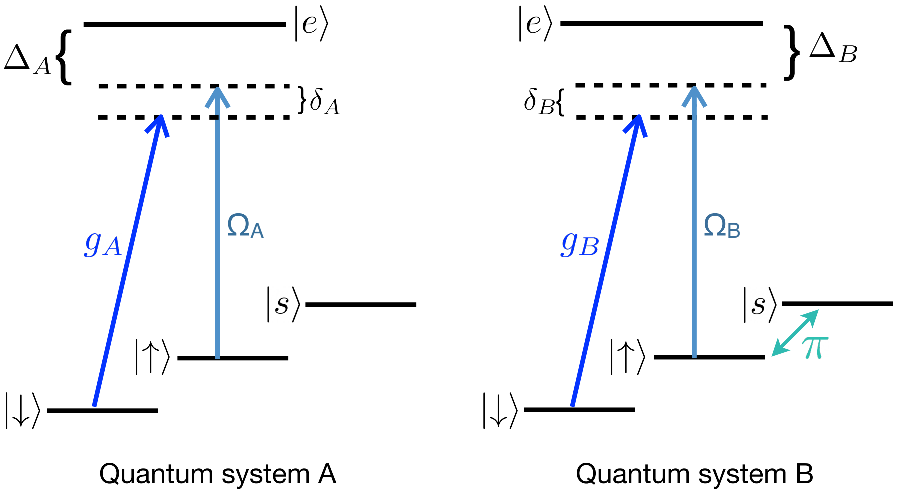

Figure 4.5: Energy-level diagrams and pulse sequence for the Raman virtual photon exchange phase gate. For each system, we establish the near two-photon resonance process using a classical laser field with Rabi frequency Ω_k and the cavity-mode with cavity coupling rate g_k, for $k \in \{A, B\}$. A MW π pulse shelves qubit B into the state $|s\rangle$. Then, laser A (B) applies a 2π pulse on qubit A (B). Another MW π pulse then brings qubit B back to its original state.

Ref. [118] (see below for more information). Here, we discuss and fully analyze our modified scheme that overcomes that challenge without limiting our analysis to a specific system. Using our proposed scheme, one may perform a controlled phase-flip gate between qubits in quantum systems with unequal optical transitions using a two-photon resonance between a driving laser and a vacuum cavity field.

For our analysis, we consider two 4-level quantum systems each containing three ground states that includes two qubit states $|\uparrow\rangle$ and $|\downarrow\rangle$ and a shelving state $|s\rangle$ in addition to an excited state $|e\rangle$. The systems are dispersively coupled to a far-detuned cavity with a high cooperativity. For each system, we drive the Raman transition between qubit ground states via the vacuum cavity field and a driving field with Rabi frequencies g_k and Ω_k, respectively, for system $k \in \{A, B\}$ as shown in Fig. 4.5. The detuning Δ_k is assumed to be large compared to the Rabi frequencies Ω_k so that the excited state will not be populated by the driving fields. For a fixed cavity frequency ω_c, if the driving fields are tuned to satisfy the resonance condition $\delta_A = \delta_B = \delta$, then an effective coupling between $|\uparrow\downarrow\rangle$ and $|\downarrow\uparrow\rangle$ is induced.

To perform the gate, first a microwave (MW) π pulse is applied to shelve qubit B (i.e., target qubit) to the shelving state $|s\rangle$. Next, the driving fields A and B are turned on to induce the Raman coupling. During the adiabatic Raman process, the qubits interact through the cavity mode via a virtual photon interaction. Once the Raman process is complete, another MW π pulse brings qubit B back to the state $|\uparrow\rangle$. The result of this gate transforms $|\uparrow\downarrow\rangle$ into $-|\uparrow\downarrow\rangle$ without affecting the relative phases of the remaining qubit product states.

In the following, we assume that $g_A = g_B = g$; however, we discuss how to compensate for unequal cavity couplings in Appendix B. For high fidelity operation, it is necessary to satisfy four main conditions: (1) the two-photon resonance detuning δ must be larger than the cavity linewidth κ, (2) the gate time given by $T = \pi\delta\Delta_A\Delta_B/g^2\Omega_A\Omega_B$ must not exceed the lifetime of the shelved state, (3) the driving field intensities should not exceed any detunings $\Omega_k \ll \Delta_k, \delta$, and (4) the system should be in the bad-cavity regime $g < \kappa$.

The maximum gate fidelity of the Raman virtual photon exchange in the high cooperativity regime is achieved under the condition that $2\delta = \kappa\sqrt{C}$, and is well approximated by

$$F_{\max} = 1 - \frac{\pi}{\sqrt{C}} - \frac{\pi^2}{16}\left[\left(\frac{T_o\delta_\epsilon}{2\pi}\right)^2 + \frac{\Delta_\epsilon^2}{\Delta^2} - \frac{18}{C}\right] - \Gamma T_o, \tag{4.3}$$

where $T_o = (\Delta/\Omega)^2(2\pi/\gamma\sqrt{C})$ is the optimal gate time, $\Omega = \Omega_A = \Omega_B\sqrt{\Delta_B/\Delta_A} \simeq \Omega_B$ is the optimal Rabi frequency condition, Δ_k is the detuning between the k^{th} quantum system's optical transition and the driving field, Γ is the effective decoherence rate that includes decoherence caused by the shelving state decay rate $\gamma_s \ll \gamma$, and $\delta_\epsilon = |\delta_A - \delta_B| \ll \delta$ is a small two-photon resonance error. This expression is valid to first order in C^{-1} and ΓT_o, and also to second order in $T_o\delta_\epsilon$ and $\Delta_\epsilon/\Delta = |\Delta_A - \Delta_B|/\Delta$, where $\Delta = (\Delta_A + \Delta_B)/2 \simeq \Delta_A \simeq \Delta_B$. See Appendices 4.6 and 4.6.3 for detailed calculations and the full expression for F_{gate} that includes the dependence on δ and κ.

The Raman scheme exchange is slower than the simple exchange by a factor of $(\Omega/\Delta)^{-2} \gg 1$, which must be large so that the excited states $|e\rangle_k$ are only virtually populated. Although the gate is slower, it gains the advantage of being much less sensitive to γ. In fact, these two factors seem to exactly cancel to give the same cooperativity scaling. However, as a consequence of the Raman scheme being slower, it can also suffer a lot from the decay of $|s\rangle$. Therefore, for high fidelity operation, it is necessary to shelve $|{\downarrow}\rangle_B$ into a metastable state where $\gamma_s \ll \gamma$ so that $\gamma_s/\gamma \ll (\Omega/\Delta)^2 \ll 1$. In this regime, the first-order correction due to the shelving decoherence is $-\gamma_s T/8$. Thus the effective decoherence rate Γ must include at least a contribution of $\gamma_s/8$.

Similar to the simple virtual photon scheme, the Raman scheme has a fairly strict resonance condition scaling by T_o^{-1}. That is, for high fidelity operation, it is necessary that the two-photon resonance be satisfied more precisely than the inverse gate time: $\delta_\epsilon \ll 2\pi T_o^{-1}$.

The main advantage of the Raman scheme is that the gate fidelity is robust against unequal optical transitions. Since the maximum fidelity depends only on the relative detuning difference $\Delta_\epsilon = |\Delta_A - \Delta_B|$ compared to the magnitude $|\Delta|$, there is an inherent trade off between gate time and system spectral separation. The larger the difference between the system transitions, the larger both cavity detunings must be to maintain the same fidelity. This, in turn, increases the overall optimal gate time. However, Δ cannot be increased indefinitely because the fidelity will eventually become limited by decoherence. By considering the bounds on the regime of high-fidelity (see figure 4.6), we find that the spectral separation that will give a maximum fidelity no less than $1 - 2\pi/\sqrt{C}$ is $\Delta_\epsilon = \kappa\gamma/(\pi\Gamma\sqrt{8})$, which corresponds to $\Omega = 2\Delta\sqrt{\Gamma/\gamma}$ and $2\Delta = \Delta_\epsilon\sqrt{\pi\sqrt{C}}$ (see Appendix 4.6.3). This limit on Δ_ϵ implies that, for $\Gamma/\gamma \ll 1$, the spectral separation of the systems can be many times larger than the cavity linewidth without significantly degrading the fidelity.

Let us note that in Ref. [118] the state $|{\downarrow}\rangle$ of one qubit is shelved in the excited state $|e\rangle$. Doing so causes an additional unwanted phase evolution on the shelved state due cavity Lamb and AC Stark shifts that cannot be reduced below the desired interaction rate without violating the adiabatic criteria. As a consequence, there does not exist a regime where the gate can be performed. We solved this issue by proposing to shelve the qubit into a

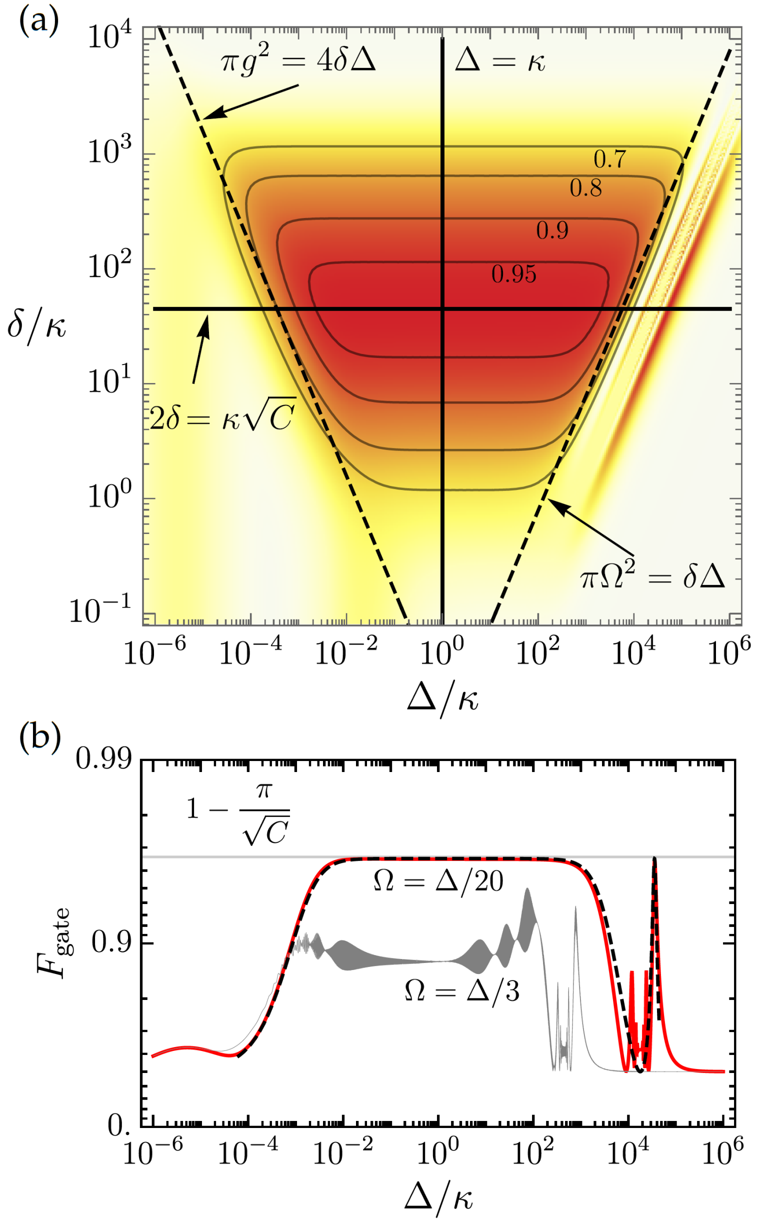

Figure 4.6: (a) Numerically-simulated fidelity of the Raman-induced virtual photon exchange phase gate F_{gate} as a function of detunings δ and Δ for a fixed $\Omega = \Delta/20$ and $g/\kappa = 10^{-1}$. The analytic bounds on the regime of high fidelity are marked with dashed black lines. The cross-section along $\Delta = \kappa$ is identical to the fidelity curve plotted in figure 4.4; but in the Raman scheme, δ has the same function as the cavity detuning in the simple exchange scheme. The maximum fidelity occurs along the ridge $2\delta = \kappa\sqrt{C}$ (solid black horizontal line). (b) Cross-section along the $2\delta = \kappa\sqrt{C}$ line. The fidelity oscillates rapidly for larger values of Ω/Δ (gray solid curve) as the driving laser begins to induce coherence between the ground and excited states and the adiabatic evolution breaks down. The red and gray lines are numerically computed while the black dashed line shows the analytic solution detailed in the appendix. Other parameters are $\delta_\epsilon = 0$, $\Delta_A = \Delta_B$, $\Gamma = 0$, and $C = 8000$.

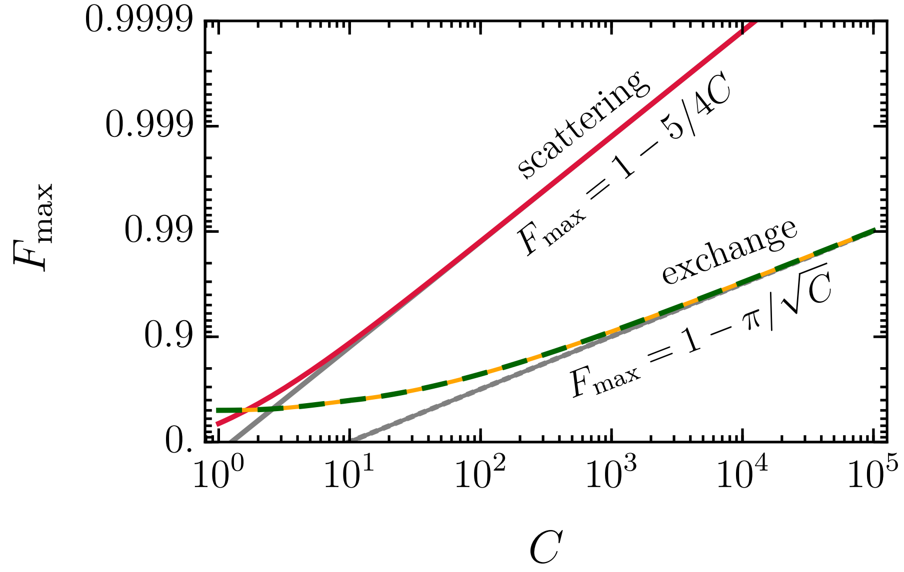

Figure 4.7: Cooperativity-limited fidelity $F_{\max}$ for phase gates based on photon scattering and virtual photon exchange. The simple photon exchange (orange line) and Raman photon exchange (dashed green line) have the same $F_{\max}$ values. The straight gray lines represent the $F_{\max}$ scaling in the limit of large C. These first-order approximations underestimate the maximum fidelity when the cooperativity is low, but still give a good estimate when the fidelity is larger than 0.8.

metastable ground state that is uncoupled to the cavity, and then we demonstrated that a large high-fidelity regime exists.

4.4 Results and Discussion

4.4.1 Scheme comparison

The maximum fidelity scaling with cavity cooperativity is very different for the scattering scheme compared to the virtual photon exchange schemes (see Fig. 4.7). In the photon scattering scheme the detection of the output photon heralds the gate and makes its fidelity independent of all sources of photon loss. Therefore, this scheme has the highest maximum fidelity with a scaling of $1 - 5/4C$. However, as a result of heralding, this scheme is probabilistic. On the other hand, the maximum fidelity of the virtual photon exchange schemes scales like $1-\pi/\sqrt{C}$, but these schemes realize deterministic gates that do not rely on single-photon generation and detection.

For each scheme, an increase in qubit decoherence will reduce the maximum attainable fidelity. To partially mitigate this effect, it is possible to reduce the total gate time. However, reducing the gate time below the optimal value will also reduce the fidelity. These two opposing effects create an intermediate optimal gate time that maximizes fidelity as a function of the effective decoherence rate of the qubits. This decoherence-limited maximum fidelity and corresponding optimal gate time have noticeably different trends for each scheme (see Fig. 4.8). In the following, we discuss other pros and cons for each scheme in more detail.

Photon scattering.— This scheme requires two nearly-identical quantum systems that must both have transitions resonant with the cavity. Having individual spectral control may require spatial resolution of the systems, which is a disadvantage for nanoscale devices. An advantage for this scheme is that the systems are not optically excited when performing the gate. Hence, this scheme could be of interest in systems with lower cavity cooperativity and some optical pure dephasing. Quantum dot devices are particularly suited to this scheme for the latter reasons, but also because a similar device could be used to efficiently generate the required single photons, providing a cohesive platform. RE ions may also be promising candidates for this scheme. Single RE emitters have been observed [22], and when coupled to a high quality factor cavity the system could provide a cavity-cooperativity large enough to achieve fast controlled phase-flip gates with a high fidelity.

The probability of heralding will depend on the efficiency of available indistinguishable single-photon sources and detectors. On-demand sources with high photon indistinguishability and single-photon purity have been demonstrated [136, 137, 138]. In addition, highly efficient on-demand sources should become increasingly available with advances in deterministic fabrication [139]. The best commercially available sources provide an efficiency of around $10\%-30\%$ in practice, but these values are likely to improve in the near future [140]. Single-photon detector efficiency is also improving [104, 141]; superconducting single-photon nanowire detectors with efficiencies exceeding 90% are becoming widely available. The overall success probability could be improved significantly if the photon source, detector, and cavity are all integrated on-chip [142, 143]. It is also possible to extend the scheme to perform non-local gates between multiple qubit-cavity systems (i.e., remote cavities). This ability can help with scalable quantum computing by naturally providing a connection between multiple qubits.

Simple virtual photon exchange.— As with the scattering scheme, this scheme also requires the ability to tune the systems' optical transitions into resonance. This can be accomplished, for example, by using an AC Stark effect provided that systems are spatially resolved or by using a large electric or magnetic field gradient if they are not spatially separated. However, after tuning the systems, spatial resolution is still required to excite only one system to the excited state without affecting the other qubit. To avoid this requirement, it might be possible to excite one system before tuning them into resonance. As a result, the time it takes to tune the systems into resonance should be much faster than the phase evolution time of the system yet slow enough to remain adiabatic. Otherwise, the phase evolves while tuning the systems, which may limit the gate fidelity.

This scheme benefits from the exchange of virtual photons; therefore, the cavity induced relaxation can be avoided. However, a limiting factor of the scheme is still the excited state lifetime of the systems. To perform the gate, it is necessary for the excited system to remain excited for a time that is long enough compared to the gate time. Otherwise, the system decays before the phase-flip gate takes place. This effect is the primary cause of the reduced cooperativity-limited fidelity of $1 - \pi/\sqrt{C}$ compared to the scattering scheme. On the other hand, the simple exchange scheme can be very fast, reducing the impact of qubit dephasing. This scheme is particularly suited to systems with little optical pure dephasing and small phonon sidebands, such as the group-IV defects in diamond [144] and rare-earth ions [145, 28].

It is also possible to perform this scheme using a Λ system. However, in the 4-level

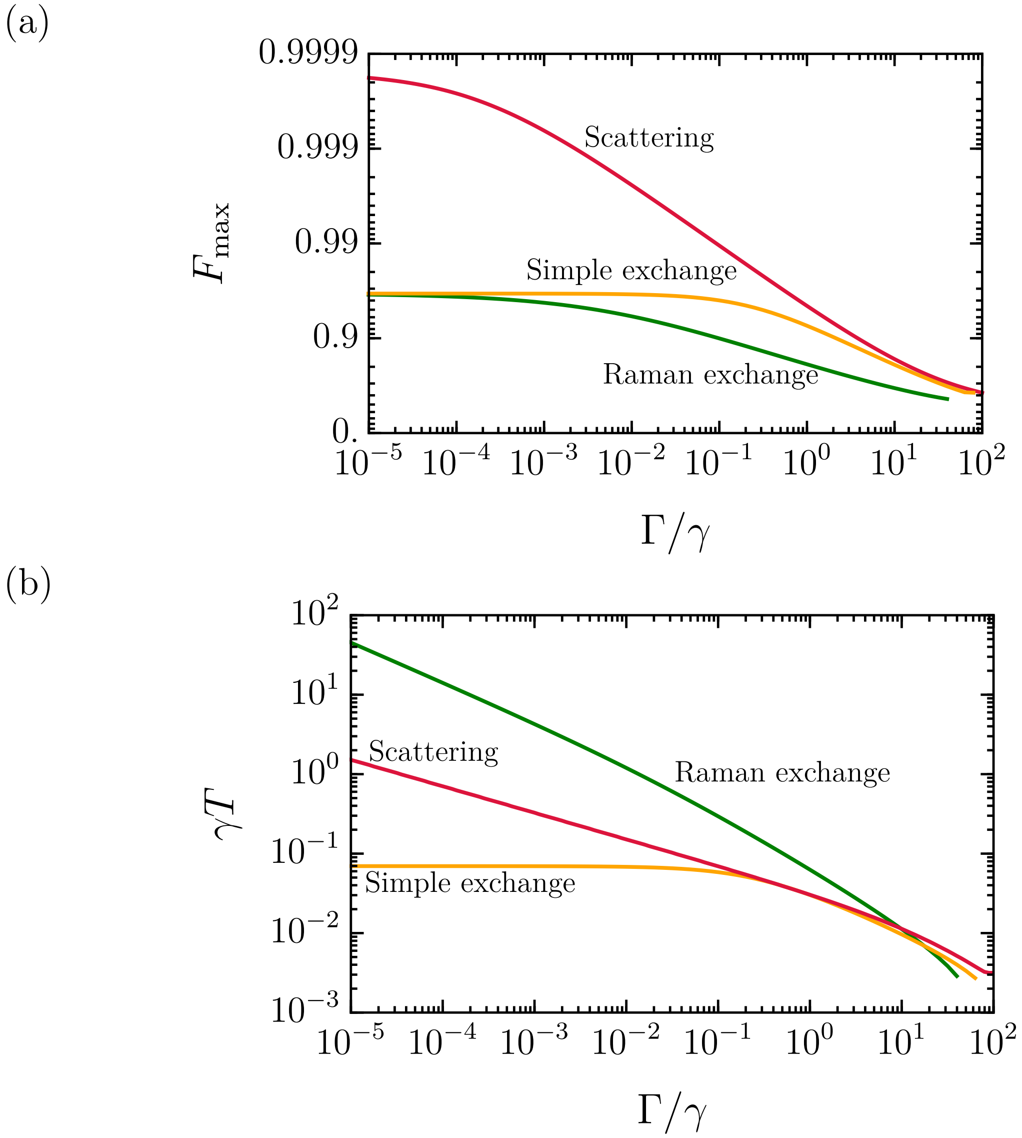

Figure 4.8: (a) Maximum fidelity F_{max} as a function of effective qubit decoherence rate Γ for the scattering scheme (red curve), simple virtual photon exchange scheme (orange curve), and the Raman virtual photon exchange scheme (green curve) using a system in the bad-cavity regime $g/\kappa = 10^{-1}$ with a cooperativity of $C = 8000$. (b) Gate time corresponding to the maximum fidelity in panel (a).

system that we have presented, tuning opposite transitions into resonance can prevent the requirement for the spatial resolution in systems with different polarization for opposite transitions, provided that both transitions can still be coupled to the same cavity mode.

Raman virtual photon exchange.— The main advantage of this scheme is the ability to adjust the frequency and intensity of driving fields A and B to allow for a difference between the optical transition frequencies of the systems. As a downside, this method requires an additional metastable state to shelve one qubit. In addition, for a large κ, the optimal detuning δ must be quite large. This could be a major limitation for some systems with multiple close optical transitions, such as rare earth ions.

With the correct parameters, the Raman scheme can be performed while maintaining the spectral resolution of the system optical transitions. This is a huge advantage for solid-state microcavity systems where emitters are often quite different and their close proximity may not allow for spatial addressing. The main trade-off for this advantage is an increase in total gate time compared to the simple virtual photon exchange, making it more susceptible to decoherence of the metastable state.

The target qubit can either be shelved in a metastable state in the ground state or in a second uncoupled excited state. However, it is preferable to shelve the qubit in a ground state as the decoherence rate of the ground states are usually less than the excited states. A spin-triplet ground-state system with a relatively long spin-coherence time and good optical properties, such as in a neutrally-charged silicon-vacancy center in diamond [146], would provide the ideal structure for this scheme.

In systems where shelving is not feasible, one could establish a Raman coupling directly between the two quantum systems [147], rather than a Raman coupling for each of the qubits individually, as explained in our protocol. Such a scheme would require a weak external laser field ($\Omega < g$) and spatial-separated nearly-identical quantum systems.

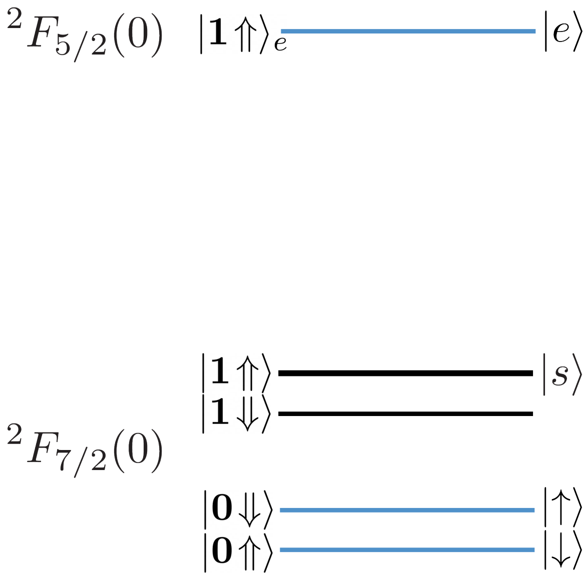

Figure 4.9: Energy level structure of ^{171}Yb:YVO in the presence of an external magnetic field along the c-axis of the crystal. Here, $|\mathbf{0}\rangle \equiv |m_s = 1/2\rangle$ and $|\mathbf{1}\rangle \equiv |m_s = -1/2\rangle$ are electron spin states and $|\Uparrow\rangle \equiv |m_I = 1/2\rangle$ and $|\Downarrow\rangle \equiv |m_I = -1/2\rangle$ are nuclear spin states. We use the $|\mathbf{0}\Downarrow\rangle$, $|\mathbf{0}\Uparrow\rangle$ and $|\mathbf{1}\Uparrow\rangle$ hyperfine states as the qubit states $|\uparrow\rangle$ and $|\downarrow\rangle$ and the shelving state $|s\rangle$ respectively.

4.4.2 Comparison of all three gate schemes for ^{171}Yb:YVO

We consider ^{171}Yb ions doped into a yttrium orthovanadate (YVO) crystal as an example system to compare the three different gates. The energy level structure of this ion in the presence of an external magnetic field is shown in Fig. 4.9. Note that, the figure only shows the lowest excited state level. Here, we refer to the two lowest ground state hyperfine levels as the qubit states $|\downarrow\rangle$ and $|\uparrow\rangle$.

For an ensemble of ^{171}Yb ions in YVO, the excited state decay rate is $\gamma = 2\pi \times 596$ Hz [148]. In addition, the spin coherence time of $T_2 = 6.6$ ms has been measured (for $B = 440$ mT) [148]. For a single Yb coupled to a YVO photonic crystal cavity, it has been shown that the spin coherence time can be further increased to 30 ms using a Carr-Purcell-Meiboom-Gill (CPMG) decoupling sequence [149].

In the following, we estimate the maximum gate fidelity and the corresponding gate time for each scheme when assuming $g/\kappa = 10^{-1}$ and $C = 50\ 000$.

Photon scattering.— Considering $\Gamma = 1/(2T_2)$, where $T_2 = 6.6$ ms, $T = 1/\gamma$, $\delta_p = 30\gamma$ and $\delta_{\epsilon_A} = \delta_{\epsilon_B} = 0$, the fidelity of the photon reflection scheme is $F_{\max} = 0.98$ and the gate time is $T = 267\ \mu$s.

Simple virtual photon exchange.— As discussed previously in Sec. 4.4, it is also possible to perform the simple virtual photon exchange scheme using a Λ type system. Here we consider a three level system and, to perform the gate we bring the $|\uparrow\rangle - |e\rangle$ transitions of the two ions into resonance with each other (instead of tuning opposite transitions). In this case, considering $\delta_{eg} = 0.2$ GHz [148], $\Gamma = 1/(2T_2) + \gamma^\star/2$ (here $\gamma^\star = 9$ KHz is calculated by the relation $\gamma^\star = 1/T_{2,O} - \gamma/2$ where $T_{2,O} = 91\ \mu$s is the optical coherence time for $B = 500$ mT [148]), and $\Delta_\epsilon = 0$ we get $F_{\max} = 0.952$ and $T = 7.5\ \mu$s.

Raman virtual photon exchange.— For this scheme, we consider the $|\mathbf{1} \Uparrow\rangle$ hyperfine ground state as the shelving level as shown in Fig. 4.9. Assuming $\Gamma = 1/(2T_2)$, $\delta_\epsilon = 0$, $\Delta_A = \Delta_B$ and $\Omega = 0.1\Delta$, the optimal fidelity and the gate time are $F_{\max} = 0.93$ and $T = 750\ \mu$s, respectively.

Increasing the cavity cooperativity will increase the fidelity and decrease the gate time of the simple and Raman virtual photon exchange schemes further. On the other hand, to improve the fidelity and the gate time of the photon scattering scheme, a photon with a smaller FWHM duration is required. Although the properties and level structure of ^{171}Yb:YVO allows performing all three schemes, the most suitable scheme for this system should be selected according to the gate requirements and experimental restrictions. As an example, if the optical transition frequencies of Yb ions are unequal, one should perform the gate using the Raman scheme. The simple virtual exchange scheme, on the other hand, is the best option to perform a fast gate. And finally, the photon scattering scheme can lead to a probabilistic but high fidelity gate.

4.5 Conclusion

Using the cavity-assisted interactions, we proposed and compared three schemes to perform controllable phase-flip gates between two qubits. The first scheme works better for systems with an integrated design and when performing a high fidelity gate is more important than a deterministic gate. If one looks for a deterministic gate, however, either the simple or Raman virtual photon exchange schemes should be considered. In cases where the quantum systems are not resonant, the Raman exchange is the best scheme. On the other hand, the simple exchange can be suitable for systems with more severe qubit dephasing but little pure dephasing of the optical transition.

Looking forward, our promising results on the photon scattering gate may provide further motivation for integrating sources and cavities on chip. Moreover, the fidelity of the simple and Raman virtual photon exchange schemes could be improved using the quantum Zeno effect [150]. In this technique, by observing possible photons emitted by the cavity at frequent time intervals using an efficient single-photon detector, the system can be forced to follow the adiabatic evolution [151]. Detecting a leaked photon also indicates a failed gate and improves fidelity.

Developing quantum information processing nodes using cavity-mediated gates is an important step towards the implementation of quantum networks. By outlining the benefits and limitations of different approaches to this goal, we provided a framework to identify and tailor two-qubit gate schemes for a given system. This will accelerate the development of platforms that could form the basis for a future quantum internet.

Acknowledgments

The authors thank I. Craiciu, A. Faraon, S. Goswami, H. Ollivier, and T. Zhong for helpful discussions. This work was supported by the Natural Sciences and Engineering Research Council of Canada (NSERC) through its Discovery Grant, Canadian Graduate Scholarships and CREATE programs, and by Alberta Innovates Technology Futures (AITF).

4.6 APPENDIX

APPROACH

4.6.1 Fidelity

For each scheme, we define two initially independent quantum systems that each include qubit states denoted $|{\uparrow}\rangle$ and $|{\downarrow}\rangle$. The total two-qubit space is spanned by the four cannonical product space states $|{\uparrow\uparrow}\rangle$, $|{\uparrow\downarrow}\rangle$, $|{\downarrow\uparrow}\rangle$, and $|{\downarrow\downarrow}\rangle$. In our analysis, we define the gate fidelity F_{gate} to be the fidelity after applying the gate operations to the initial product state $|\psi(0)\rangle = (1/2)(|{\uparrow}\rangle + |{\downarrow}\rangle)_A \otimes (|{\uparrow}\rangle + |{\downarrow}\rangle)_B$:

$$F_{\text{gate}} = \sqrt{\langle\psi(T)|\,\hat{\rho}(T)\,|\psi(T)\rangle}, \tag{A1}$$

where $\rho(T)$ (or $|\phi(T)\rangle\langle\phi(T)|$ in the case of a pure state) is the imperfect final state and $|\psi(T)\rangle$ is the expected ideal pure state after applying the gate operation with duration time T. For example, if the gate operation takes $|{\downarrow\downarrow}\rangle \longrightarrow -|{\downarrow\downarrow}\rangle$ relative to the remaining three product states, the ideal state is $|\psi(T)\rangle = (1/2)(|{\uparrow\uparrow}\rangle + |{\uparrow\downarrow}\rangle + |{\downarrow\uparrow}\rangle - |{\downarrow\downarrow}\rangle)$. This choice of initial state serves to represent an average gate fidelity because it takes into account the effect of the gate on each product state amplitude in addition to the relative phases between them. It also represents the fidelity expected when using the gate to generate maximally entangled states. However, certain initial states may result in higher or lower fidelity than this definition predicts. For example, the initial state $|{\uparrow}\rangle_A \otimes (|{\uparrow}\rangle + |{\downarrow}\rangle)_B/\sqrt{2}$ for the above example could have above-average fidelity since it will not experience infidelity due to the imperfect phase-flip operation on $|{\downarrow\downarrow}\rangle$. On the other hand, $|{\downarrow}\rangle_A \otimes (|{\uparrow}\rangle + |{\downarrow}\rangle)_B/\sqrt{2}$ could experience below-average fidelity due to the absence of contribution from the less-stringent evolution on $|{\uparrow\uparrow}\rangle$ and $|{\uparrow\downarrow}\rangle$.

4.6.2 Decoherence

To simplify the analysis and to focus on the intrinsic high-performance limitations for each scheme, we assume that decoherence processes other than cavity dissipation and spontaneous emission occur on a timescale much longer than the gate time. These additional processes include qubit decoherence and possibly pure dephasing of the optical transition. To capture these small effects, we describe the effect of any of these additional processes by a single effective decoherence rate Γ. The exact form of Γ may be different depending on the scheme and on the dominant source of additional decoherence for a system operating under a given scheme. For example, regardless of the scheme, the effective qubit decoherence rate Γ must be at least limited by the qubit relaxation rate $\gamma_{\uparrow\downarrow}$ and pure dephasing rate $\gamma^{\star}_{\uparrow\downarrow}$. Consider the following decoherence master equation:

$$\dot{\rho} = \gamma_{\uparrow\downarrow}\mathcal{D}(\hat{\sigma})\rho(t) + 2\gamma^{\star}_{\uparrow\downarrow}\mathcal{D}(\hat{\sigma}^{\dagger}\hat{\sigma})\rho(t), \tag{A2}$$

where $\mathcal{D}(\hat{\sigma})\hat{\rho} = \hat{\sigma}\hat{\rho}\hat{\sigma}^{\dagger} - \{\hat{\sigma}^{\dagger}\hat{\sigma}, \hat{\rho}\}/2$ for $\hat{\sigma}\left|\uparrow\right\rangle = \left|\downarrow\right\rangle$. If we wish to maintain the coherence of an initial state $\left|\psi(0)\right\rangle = (\left|\uparrow\right\rangle + \left|\downarrow\right\rangle)/\sqrt{2} = \left|\psi(T)\right\rangle$, the fidelity of the final state $\hat{\rho}(T)$ will be

$$\sqrt{\left\langle\psi(T)\right|\hat{\rho}(T)\left|\psi(T)\right\rangle} \simeq 1 - \Gamma T, \tag{A3}$$

when expanding to first order in $\gamma_{\uparrow\downarrow}T \ll 1$ and $\gamma^{\star}_{\uparrow\downarrow}T \ll 1$ where $\Gamma = \gamma_{\uparrow\downarrow}/8 + \gamma^{\star}_{\uparrow\downarrow}/4$. In most real applications, the effective decoherence rate Γ will be dominated by the largest source of additional decoherence for that particular system or scheme-system combination.

4.6.3 Non-Hermitian dynamics

In the virtual photon exchange schemes, we take advantage of non-Hermitian Hamiltonians to include cavity dissipation and spontaneous emission as opposed to solving the full master equation. This allows us to capture the effects of finite cavity cooperativity while still allowing for simple and accurate analytically tractable solutions.

Dynamics from non-Hermitian Hamiltonians cannot capture an increase in population of the ground state due to a decay event. To illustrate this, consider the Master equation

$$\dot{\rho} = -i[\hat{H}, \hat{\rho}] + \gamma\mathcal{D}(\hat{\sigma})\hat{\rho} + \kappa\mathcal{D}(\hat{a})\hat{\rho}, \tag{A4}$$

where we take $\hbar = 1$. This can be rewritten as [152]:

$$\begin{aligned}\dot{\rho} &= -i\left[\hat{H}, \hat{\rho}\right] - \frac{1}{2}\{\gamma\hat{\sigma}^\dagger\hat{\sigma} + \kappa\hat{a}^\dagger\hat{a}, \hat{\rho}\} + \gamma\hat{\sigma}\hat{\rho}\hat{\sigma}^\dagger + \kappa\hat{a}\hat{\rho}\hat{a}^\dagger \\ &= -i\left(\hat{\mathcal{H}}_{\text{eff}}\hat{\rho} - \hat{\rho}\hat{\mathcal{H}}_{\text{eff}}^\dagger\right) + \gamma\hat{\sigma}\hat{\rho}\hat{\sigma}^\dagger + \kappa\hat{a}\hat{\rho}\hat{a}^\dagger,\end{aligned} \tag{A5}$$

where

$$\hat{\mathcal{H}}_{\text{eff}} = \hat{H} - \frac{i}{2}\left(\gamma\hat{\sigma}^\dagger\hat{\sigma} + \kappa\hat{a}^\dagger\hat{a}\right) \tag{A6}$$

is the effective non-Hermitian Hamiltonian that describes the amplitude decay of $\hat{\sigma}$ and $\hat{a}$.

The solution $|\phi(t)\rangle$ under the effective Hamiltonian is the unnormalized pure state trajectory for a successful gate and this trajectory occurs with probability $p = \langle\phi(t)|\phi(t)\rangle$. The terms $\gamma\hat{\sigma}\hat{\rho}\hat{\sigma}^\dagger$ and $\kappa\hat{a}\hat{\rho}\hat{a}^\dagger$ in the master equation cause a recycling of population into the ground state after a decay event. Thus the total master equation solution is given by $\hat{\rho}(t) = |\phi(t)\rangle\langle\phi(t)| + (1-p)\hat{\rho}_{\gamma\kappa}(t)$ where $\hat{\rho}_{\gamma\kappa}(t)$ is the state of the system at time t given that at least one emission event occurred. The final fidelity after completing the gate of duration T is then

$$F_{\text{gate}} = \sqrt{pF_0^2 + (1-p)F_{\gamma\kappa}^2} \tag{A7}$$

where $F_0 = |\langle\phi(T)|\psi(T)\rangle|/\sqrt{p}$ is the fidelity after a successful gate, and the potentially non-zero fidelity after a failed gate is $F_{\gamma\kappa} = \sqrt{\langle\psi(T)|\,\hat{\rho}_{\gamma\kappa}(T)\,|\psi(T)\rangle}$.

By only solving the effective non-Hermitian Hamiltonian part of the master equation, we make the approximation that $F_{\text{gate}} \simeq \sqrt{p}F_0$. This approximation is accurate when $p \simeq 1$ and hence when $\sqrt{p}F_0 \simeq 1$. The precision of this approximation depends on F_0 and $F_{\gamma\kappa}$ for a given implementation. Since $F_{\gamma\kappa} < F_0$ for the schemes we study, this approximation is also valid to explore the cooperativity scaling of the fidelity limits. We comment on the accuracy of this approximation for the specific cases of the virtual photon exchange schemes in the following appendix section.

FIDELITY CALCULATIONS

4.6.1 Photon scattering

In this scheme, the probability that an incident photon excites either qubit is low. Therefore, the quantum Langevin equations for the photon (quantum system) excitation amplitude(s) $a(t)$ ($s_k(t)$, $k \in \{A, B\}$) can be written as [100, 153, 154]

$$\begin{aligned}
\dot{a}(t) &= -\frac{\kappa}{2}a(t) + g_A s_A(t) + g_B s_B(t) - \sqrt{\kappa}a_{\text{in}}(t), \\
\dot{s}_A(t) &= -g_A a(t) + \left(-\frac{\gamma}{2} - i\Delta_A\right) s_A(t), \\
\dot{s}_B(t) &= -g_B a(t) + \left(-\frac{\gamma}{2} - i\Delta_B\right) s_B(t),
\end{aligned} \tag{B1}$$

where $a_{\text{in}}(t)$ is the input photon field, g_k is the cavity coupling rate for the k^{th} quantum system, and Δ_k is the detuning between the $|{\downarrow}\rangle \to |e\rangle$ transition of the k^{th} quantum system and the bare cavity mode. Using the input-output relation $a_{\text{out}} = \sqrt{\kappa}a + a_{\text{in}}$, the ratio of output and input field for a plane wave input is

$$\frac{a_{\text{out}}(\omega)}{a_{\text{in}}(\omega)} = 1 - \frac{\kappa}{\kappa/2 + g_A^2/r_A + g_B^2/r_B - i\omega}, \tag{B2}$$

where $r_k = \gamma/2 + i(\Delta_k - \omega)$ and ω is the plane wave frequency detuning from the cavity resonance. This expression is valid in both the strong-coupling and bad-cavity regimes [100]. Using the above general expression for the photon amplitude of plane wave $|\omega\rangle$, we can write the amplitude $s_{ij}(\omega)$ (where $i, j \in \{\uparrow, \downarrow\}$) expected for each initial qubit product state $|{\uparrow\uparrow}\rangle$, $|{\uparrow\downarrow}\rangle$, $|{\downarrow\uparrow}\rangle$, and $|{\downarrow\downarrow}\rangle$ so that $|ij\rangle\,|\omega\rangle \longrightarrow s_{ij}(\omega)\,|ij\rangle\,|\omega\rangle$. This can be done by setting the Δ_k

zero for $|\uparrow\rangle_k$ and non-zero but large for $|\downarrow\rangle_k$. Under the assumptions that $g_A = g_B = g$ and Δ_A, $\Delta_B \gg \kappa$ (when nonzero) we have

$$\begin{aligned}
s_{\uparrow\uparrow}(\omega) &= \left.\frac{a_{\text{out}}(\omega)}{a_{\text{in}}(\omega)}\right|_{\Delta_A=0,\Delta_B=0} = 1 - \frac{2\kappa(\gamma - 2i\omega)}{2\kappa\gamma C + (\kappa - 2i\omega)(\gamma - 2i\omega)}, \\
s_{\uparrow\downarrow}(\omega) &= \lim_{\Delta_B\to\infty} \left.\frac{a_{\text{out}}(\omega)}{a_{\text{in}}(\omega)}\right|_{\Delta_A=0} = 1 - \frac{2\kappa(\gamma - 2i\omega)}{\kappa\gamma C + (\kappa - 2i\omega)(\gamma - 2i\omega)}, \\
s_{\downarrow\uparrow}(\omega) &= \lim_{\Delta_A\to\infty} \left.\frac{a_{\text{out}}(\omega)}{a_{\text{in}}(\omega)}\right|_{\Delta_B=0} = 1 - \frac{2\kappa(\gamma - 2i\omega)}{\kappa\gamma C + (\kappa - 2i\omega)(\gamma - 2i\omega)}, \\
s_{\downarrow\downarrow}(\omega) &= \lim_{\Delta_B\to\infty,\Delta_A\to\infty} \frac{a_{\text{out}}(\omega)}{a_{\text{in}}(\omega)} = -1 - \frac{4i\omega}{\kappa - 2i\omega}.
\end{aligned} \tag{B3}$$

where $C = 4g^2/\kappa\gamma$. Although we do not present it here, the above set of equations could include finite quantum system detunings for systems A and B by evaluating the ratio $a_{\text{out}}/a_{\text{in}}$ for $\Delta_A = \delta_{\epsilon_A}$ and $\Delta_B = \delta_{\epsilon_B}$ instead of $\Delta_A = 0$ and $\Delta_B = 0$, where appropriate. To illustrate how these amplitudes indicate a controlled phase gate, consider the ideal case where we have a perfect plane wave exactly resonant with the cavity so that $\omega = 0$. Then the amplitudes reduce to

$$\begin{aligned}
s_{\uparrow\uparrow}(0) &= 1 - \frac{2}{2C+1}, \\
s_{\uparrow\downarrow}(0) &= 1 - \frac{2}{C+1}, \\
s_{\downarrow\uparrow}(0) &= 1 - \frac{2}{C+1}, \\
s_{\downarrow\downarrow}(0) &= -1.
\end{aligned} \tag{B4}$$

From this it is clear that when $C \gg 1$ these ratios converge to 1, 1, 1 and -1, respectively.

In reality, some deviation from the ideal conditions are expected. In particular, we consider a finite Gaussian bandwidth photon with a standard deviation σ_p and a possible small cavity resonance error of δ_p. Even though the final spin state is pure for a plane wave, the spin-frequency entanglement captured by the frequency-dependent amplitudes $s_{ij}(\omega)$ causes some reflection-induced spin dephasing. To correct for a finite bandwidth photon, we consider an initial photon state $|p\rangle = \int d\omega f(\omega) |\omega\rangle$ where

$$|f(\omega)|^2 = \frac{1}{\sigma_p\sqrt{2\pi}} e^{-(\omega-\delta_p)^2/2\sigma_p^2}. \tag{B5}$$

For an initial spin state $(1/2)(|\uparrow\rangle + |\downarrow\rangle)_A \otimes (|\uparrow\rangle + |\downarrow\rangle)_B$, the joint spin-photon state after reflection is

$$|\phi(T)\rangle_{\text{sp}} = \frac{1}{2}\int d\omega \sum_{ij} s_{ij}(\omega) f(\omega) |ij\rangle |\omega\rangle . \tag{B6}$$

where we take the total gate time T to be twice the FWHM of the photon duration: $T = 8\pi\sqrt{2\ln 22}/\sigma_p$. The reduced spin density matrix $\hat{\rho}$ can then be obtained by tracing out the state of the photon $\hat{\rho}(T) = \text{Tr}_p\left(|\phi(T)\rangle\langle\phi(T)|_{\text{sp}}\right)$. This gives

$$\hat{\rho}(T) = \frac{1}{4}\int d\omega \sum_{ij}\sum_{kl} s_{ij}(\omega) s^*_{kl}(\omega) |f(\omega)|^2 |ij\rangle \langle kl| . \tag{B7}$$

After a single photon reflects off the cavity, the final state of the two-qubit system can be compared with the ideal state $|\psi(T)\rangle = (1/2)(|\uparrow\uparrow\rangle + |\uparrow\downarrow\rangle + |\downarrow\uparrow\rangle - |\downarrow\downarrow\rangle)$ to give the total gate fidelity F_{gate} from equation (A1). By following this procedure using (B7) to take into account small imperfections due to nonzero δ_p, σ_p, and δ_{ϵ_k}, we derived the total gate fidelity F_{gate} as presented in equation (1) of the main text. This was done analytically by first expanding the amplitudes s_{ij} in terms of small $\omega/C\gamma$ and then integrating over the Gaussian photon profile.

We also note that, in the limit that σ_p and δ_p are small, the amplitudes from equation (B4) immediately give the cooperativity-limited maximum fidelity of

$$F_{\max} = 1 - \frac{1}{C+1} - \frac{1}{4C+2} \simeq 1 - \frac{5}{4C}. \tag{B8}$$

4.6.2 Simple virtual photon exchange

For this scheme, we begin with two four-level systems coupled to a single cavity mode. The general Hamiltonian that governs the evolution is $\hat{H} = \hat{H}_A + \hat{H}_B + \hat{H}_C + \hat{H}_I$. The quantum system $\hat{H}_k$ is given by

$$\hat{H}_k = \omega_k \hat{\sigma}^\dagger_{\uparrow_k} \hat{\sigma}_{\uparrow_k} + (\omega_k - \omega_e)\hat{\sigma}^\dagger_{\downarrow_k} \hat{\sigma}_{\downarrow_k} - \omega_g \hat{\sigma}^\dagger_{\uparrow\downarrow_k} \hat{\sigma}_{\uparrow\downarrow_k}, \tag{B9}$$

where ω_k is the frequency separation between $|\uparrow\rangle_k$ and $|e_2\rangle_k$, ω_e is the separation between $|e_1\rangle_k$ and $|e_2\rangle_k$, and ω_g is the separation between $|\uparrow\rangle_k$ and $|\downarrow\rangle_k$. Also, $\hat{\sigma}_{\downarrow_k} |e_1\rangle_k = |\downarrow\rangle_k$, $\hat{\sigma}_{\uparrow_k} |e_2\rangle = |\uparrow\rangle_k$, and $\hat{\sigma}_{\uparrow\downarrow_k} |\downarrow\rangle_k = |\uparrow\rangle_k$ (see figure 3 of the main text). The cavity homogeneous evolution is $\hat{H}_C = \omega_C \hat{a}^\dagger \hat{a}$ for cavity frequency ω_C, cavity photon anihilation (creation) operator $\hat{a}$ ($\hat{a}^\dagger$), and the interaction part is given by

$$\hat{H}_I = \sum_{j\in\uparrow,\downarrow} \sum_{k\in A,B} g_{j_k} \hat{\sigma}^\dagger_{j_k} \hat{a} + \text{h.c.}, \tag{B10}$$

where $g_{\downarrow_k}$ is the cavity coupling rate of the $|\downarrow\rangle \to |e_1\rangle$ transition to the cavity mode and $g_{\uparrow_k}$ is the cavity coupling rate of the $|\uparrow\rangle \to |e_2\rangle$ transition to the cavity mode. The dissipation is governed by the Lindblad master equation

$$\dot{\rho} = -i[\hat{H}, \hat{\rho}] + \kappa \mathcal{D}(\hat{a})\hat{\rho} + \sum_{k,j} \gamma_{j_k} \mathcal{D}(\hat{\sigma}_{j_k})\hat{\rho} \tag{B11}$$

where $\mathcal{D}(\hat{A})\hat{\rho} = \hat{A}\hat{\rho}\hat{A}^\dagger - \{\hat{A}^\dagger \hat{A}, \hat{\rho}\}/2$, κ is the decay rate of the cavity photon, γ_{j_k} are the decay rates of the $|e_1\rangle_k \to |\downarrow\rangle_k$ and $|e_2\rangle_k \to |\uparrow\rangle_k$ transitions. In the following, we assume $\gamma_{j_k} = \gamma$ for all j and k. The corresponding effective non-Hermitian Hamiltonian is then

$$\hat{\mathcal{H}}_{\text{eff}} = \hat{H} - \frac{i}{2}\left[\kappa \hat{a}^\dagger \hat{a} + \gamma \sum_{k,j} \hat{\sigma}^\dagger_{j_k} \hat{\sigma}_{j_k}\right] \tag{B12}$$

Note that the effective Hamiltonian for dissipation due to γ does not discriminate between events that emit into $|\uparrow\rangle$ or $|\downarrow\rangle$ because the recycling term is neglected. That is, γ here represents the total decay rate of the excited states.

The total cavity-qubit system can be broken into four subsystems defined by the four basis states of the electronic ground states: $\{|\uparrow\uparrow\rangle, |\downarrow\uparrow\rangle, |\uparrow\downarrow\rangle, |\downarrow\downarrow\rangle\}$. To perform a control phase gate using a virtual photon interaction, quantum system A is excited at ω_A so that $|\uparrow\rangle_A \to |e_2\rangle_A$. This implies that $|\uparrow\downarrow\rangle \to |e_2\downarrow\rangle$ and $|\uparrow\uparrow\rangle \to |e_2\uparrow\rangle$. Hence we are concerned with the relative evolution within the two subsystems governed by $H_{\uparrow\downarrow}$ and $H_{\uparrow\uparrow}$. In our analysis, we assume that infidelity due to the fast excitation process $|\uparrow\rangle_A \to |e_2\rangle_A$ is much smaller than the infidelity due to the slower adiabatic virtual photon exchange process; we focus only on the phase rotation component of the protocol.

In the single-excited $\uparrow\downarrow$ subspace with the basis $\{|e_2\downarrow 0\rangle, |\uparrow\downarrow 1\rangle, |\uparrow e_1 0\rangle\}$, $H_{\uparrow\downarrow}$ can be written as

$$\hat{H}_{\uparrow\downarrow} = \begin{pmatrix} 0 & g_{\uparrow_A} & 0 \\ g_{\uparrow_A} & \Delta_A & g_{\downarrow_B} \\ 0 & g_{\downarrow_B} & \Delta_A - \Delta_B - \delta_{eg} \end{pmatrix}, \tag{B13}$$

where $\Delta_k = \omega_C - \omega_k$ and $\delta_{eg} = \omega_e - \omega_g$. In the single-excited $\uparrow\uparrow$ subspace with the basis $\{|e_2\uparrow 0\rangle, |\uparrow\uparrow 1\rangle, |\uparrow e_2 0\rangle\}$, $H_{\uparrow\uparrow}$ can be written as

$$\hat{H}_{\uparrow\uparrow} = \begin{pmatrix} 0 & g_{\uparrow_A} & 0 \\ g_{\uparrow_A} & \Delta_A & g_{\uparrow_B} \\ 0 & g_{\uparrow_B} & \Delta_A - \Delta_B \end{pmatrix}. \tag{B14}$$

The last index of each combined-system state indicates the photon number in the cavity mode.

The evolution of the remaining subsystems is $H_{\downarrow\uparrow} = H_{\downarrow\downarrow} = 0$ for the unexcited states $|\downarrow\uparrow\rangle$ and $|\downarrow\downarrow\rangle$. Note that since only two of the four basis states are evolving in this scheme; we are concerned with only the relative phase between $|\uparrow\downarrow\rangle$ and $|\uparrow\uparrow\rangle$. This is because any global phase for $|\uparrow\downarrow\rangle$ and $|\uparrow\uparrow\rangle$ can be eliminated by moving qubit A into the correct rotating frame. Knowing this, we can simplify the total gate fidelity to $F_{\text{gate}} = (F_\pi + 1)/2$ where $F_\pi = |\langle\phi(T)|\,(|\uparrow\uparrow\rangle - |\uparrow\downarrow\rangle)|/\sqrt{2}$ is the fidelity of the relative π-phase gained between state $|\uparrow\uparrow\rangle$ and $|\uparrow\downarrow\rangle$ for the initial state $|\psi(0)\rangle = (|\uparrow\uparrow\rangle + |\uparrow\downarrow\rangle)/\sqrt{2}$.

In the regime where Δ_k are much larger than the cavity coupling rates, the Hamiltonian $H_{\uparrow\uparrow}$ performs a π-phase rotation on $|e_2 \uparrow 0\rangle$ if $\Delta_A - \Delta_B \simeq 0$. Alternatively, if $\Delta_A - \Delta_B \simeq \delta_{eg}$, $H_{\uparrow\downarrow}$ performs the π-phase on $|e_2 \downarrow 0\rangle$. These two scenarios are equivalent and so, without loss of generality, we focus only on the case where the opposite spin transitions are resonant $\Delta_A - \Delta_B \simeq \delta_{eg}$.

Since the cavity coupling rates may not be equal, it may be necessary to tune Δ_B to offset the different Stark shifts induced on each qubit by the cavity. By adiabatically eliminating the amplitude of state $|\uparrow\downarrow 1\rangle$, the optimal tuning of the unexcited qubit is found to be

$$\Delta_B = \Delta + \frac{g_{\uparrow A}^2 - g_{\downarrow B}^2}{\Delta} - \delta_{eg}, \tag{B15}$$

where we write $\Delta_A = \Delta$ for simplicity. The corresponding excitation time required to achieve a π phase is given by

$$T = \pi \frac{\Delta}{g_{\uparrow A} g_{\downarrow B}}. \tag{B16}$$

High phase gate fidelity for virtual photon exchange is dependent on satisfying four main conditions: (1) the cavity detuning Δ must exceed the decay rate κ of the cavity, (2) the gate time T must not exceed the lifetime of the system excited state $1/\gamma$, and (3) the system should not be far into the strong-coupling regime $g/\kappa \leq 1$. Finally, (4) high fidelity operation depends critically on achieving the one-photon resonance condition. To capture how sensitive the fidelity is to errors in matching the resonance condition in equation (B15), we assume that Δ_B deviates from the ideal condition by some small value Δ_ϵ. That is, $\Delta_\epsilon = \Delta_B - \Delta - (g_{\uparrow A}^2 - g_{\downarrow B}^2)/\Delta + \delta_{eg}$.

The effective non-Hermitian Hamiltonians corresponding to $\hat{H}_{\uparrow\downarrow}$ and $\hat{H}_{\uparrow\uparrow}$ are

$$\begin{aligned}\hat{\mathcal{H}}_{\uparrow\downarrow} &= \hat{H}_{\uparrow\downarrow} - \frac{i}{2}\left(\gamma\,|e_2{\downarrow}0\rangle\langle e_2{\downarrow}0| + \gamma\,|{\uparrow}e_1 0\rangle\langle{\uparrow}e_1 0| + \kappa\,|{\uparrow\downarrow}1\rangle\langle{\uparrow\downarrow}1|\right)\\ \hat{\mathcal{H}}_{\uparrow\uparrow} &= \hat{H}_{\uparrow\uparrow} - \frac{i}{2}\left(\gamma\,|e_2{\uparrow}0\rangle\langle e_2{\uparrow}0| + \gamma\,|{\uparrow}e_1 0\rangle\langle{\uparrow}e_1 0| + \kappa\,|{\uparrow\uparrow}1\rangle\langle{\uparrow\uparrow}1|\right).\end{aligned} \tag{B17}$$

By performing adiabatic elimination on the amplitude of $|{\uparrow\downarrow}1\rangle$ and $|{\uparrow\uparrow}1\rangle$ where we set $d\langle\phi(t)|\uparrow\downarrow 1\rangle/dt = d\langle\phi(t)|\uparrow\uparrow 1\rangle/dt = 0$, we can compute F_π. Although by choosing Δ_B correctly, the unequal cavity coupling rates can be compensated, to minimize the gate time $T \propto (g_{\uparrow_A} g_{\downarrow_B})^{-1}$ it is optimal to have $g_{\uparrow_A} \simeq g_{\downarrow_B} = g$. In this case, we have

$$\begin{aligned}F_\pi &= \frac{1}{2}\left|\langle e_2 \uparrow 0|e^{-iT\hat{\mathcal{H}}_{\uparrow\uparrow}}|e_2 \uparrow 0\rangle - \langle e_2 \downarrow 0|e^{-iT\hat{\mathcal{H}}_{\uparrow\downarrow}}|e_2 \downarrow 0\rangle\right|\\ &= \frac{1}{2}e^{-2\pi\Delta/C\kappa - \pi\kappa/2\Delta}\left|e^{i4\pi g^2/\Delta\delta_{eg}} + \cosh\left[\frac{\pi\kappa}{2\Delta}\right]e^{-i\pi\Delta_\epsilon\Delta/g^2}\right|.\end{aligned} \tag{B18}$$

In the case where $\delta_{eg} \gg g^2/\Delta \gg \Delta_\epsilon$, this can be written as

$$F_\pi = e^{-2\pi\Delta/C\kappa - \pi\kappa/2\Delta}\cosh^2\left[\frac{\pi\kappa}{4\Delta}\right] + \mathcal{O}\left(\Delta_\epsilon^2, \delta_{eg}^{-2}\right). \tag{B19}$$

Then the total gate fidelity is given by $F_{\text{gate}} = (F_\pi + 1)/2$. This expression is maximized for the choice $2\Delta \simeq \kappa\sqrt{C}$ when $g < \kappa$ (see Figure 4 in the main manuscript). Then in the regime where $C \gg 1$, the maximum gate fidelity in the ideal regime can be expanded to the lowest order non-vanishing terms to acquire the result presented in equation (2) of the main text.

If a photon is emitted during the gate and system A collapses to the ground state $|{\uparrow}\rangle_A$ prematurely, then the final pulse used to return system A coherently to the ground state will instead re-excite $|{\uparrow}\rangle_A$. Since system A is in an excited state after a failure, the fidelity $F_{\gamma\kappa}$ vanishes and so the non-Hermitian approximation is exact in this case.

4.6.3 Raman virtual photon exchange

The analysis of the Raman scheme follows similar to the simple virtual photon exchange scheme. However, with the addition of the Raman coupling there are two nested adiabatic processes occurring. To simplify the analysis, we will assume that any infidelity caused by pulses 1 and 2 used to shelve $|{\downarrow}\rangle_B$ are negligible compared to infidelity caused by the much slower Raman interaction.

For this scheme, we begin with two four-level systems coupled to a single cavity mode (see figure 5 of the main text). The general Hamiltonian that governs the evolution is $\hat{H} = \hat{H}_A + \hat{H}_B + \hat{H}_C + \hat{H}_I$. The quantum system $\hat{H}_k$ is given by

$$\hat{H}_k = \omega_k \hat{\sigma}^\dagger_{\uparrow_k} \hat{\sigma}_{\uparrow_k} + \omega_{s_k} \hat{\sigma}^\dagger_{s_k} \hat{\sigma}_{s_k} - \omega_{g_k} \hat{\sigma}^\dagger_{\uparrow\downarrow_k} \hat{\sigma}_{\uparrow\downarrow_k}, \tag{B20}$$

where ω_k is the frequency separation between the $|{\uparrow}\rangle_k$ and $|e\rangle_k$ states, ω_{s_k} is the separation of the shelving state $|s\rangle_k$ and $|{\uparrow}\rangle_k$, and ω_{g_k} is the separation of the $|{\uparrow}\rangle_k$ and $|{\downarrow}\rangle_k$ states. Also, $\hat{\sigma}_{\uparrow_k} |e\rangle_k = |{\uparrow}\rangle_k$, $\hat{\sigma}_{s_k} |s\rangle_k = |{\downarrow}\rangle_k$, and $\hat{\sigma}_{\uparrow\downarrow_k} |{\downarrow}\rangle_k = |{\uparrow}\rangle_k$ (see figure 5 of the main text). The cavity homogeneous evolution is $\hat{H}_C = \omega_C \hat{a}^\dagger \hat{a}$ for cavity frequency ω_C, cavity photon anihilation (creation) operator $\hat{a}$ ($\hat{a}^\dagger$), and the interaction part is given by

$$\hat{H}_I = \sum_{k \in A,B} g_k \hat{\sigma}^\dagger_{\uparrow_k} \hat{\sigma}_{\uparrow\downarrow_k} \hat{a} + \Omega_k \hat{\sigma}^\dagger_{\uparrow_k} e^{it\omega_{L_k}} + \text{h.c.}, \tag{B21}$$

where g_k is the cavity coupling rate of the $|{\uparrow}\rangle \rightarrow |e\rangle$ transition to the cavity mode and ω_{L_k} is the control laser frequency coupling $|{\downarrow}\rangle_k$ and $|e\rangle_k$ via the operator $\hat{\sigma}^\dagger_{\uparrow_k} \hat{\sigma}_{\uparrow\downarrow_k} |{\downarrow}\rangle_k = \hat{\sigma}^\dagger_{\uparrow_k} |{\uparrow}\rangle_k = |e\rangle_k$ with Rabi frequency Ω_k. The dissipation is governed by the Lindblad master equation

$$\dot{\rho} = -i[\hat{H}, \hat{\rho}] + \kappa \mathcal{D}(\hat{a})\hat{\rho} + \sum_k \gamma_k \mathcal{D}(\hat{\sigma}_{\uparrow_k})\hat{\rho} + \sum_k \gamma_{s_k} \mathcal{D}(\hat{\sigma}_{s_k})\hat{\rho}, \tag{B22}$$

where $\mathcal{D}(\hat{A})\hat{\rho} = \hat{A}\hat{\rho}\hat{A}^\dagger - \{\hat{A}^\dagger \hat{A}, \hat{\rho}\}/2$, κ is the decay rate of the cavity photon, γ_k is the decay rate of $|e\rangle_k$, and γ_{s_k} as the decay rate of the shelving state $|s\rangle_k$. The corresponding effective non-Hermitian Hamiltonian is then

$$\hat{\mathcal{H}}_{\text{eff}} = \hat{H} - \frac{i}{2}\left[\kappa \hat{a}^\dagger \hat{a} + \gamma \sum_k \hat{\sigma}^\dagger_{\uparrow_k}\hat{\sigma}_{\uparrow_k} + \gamma_s \sum_k \hat{\sigma}^\dagger_{s_k}\hat{\sigma}_{s_k}\right] \tag{B23}$$

where we have assumed $\gamma_k = \gamma$ and $\gamma_{s_k} = \gamma_s$ for both quantum systems A and B. Recall again that the effective Hamiltonian does not discriminate which ground state recycles the population. In effect, γ_s represents the total decay rate out of $|s\rangle$ into any other state.

As with the virtual photon exchange, we can first break the system into four subsystems associated with the four basis states of the two-qubit space: $\{|\uparrow\uparrow\rangle, |\downarrow\uparrow\rangle, |\uparrow\downarrow\rangle, |\downarrow\downarrow\rangle\}$. After shelving $|\uparrow\rangle_B$ to state $|s\rangle_B$, these states become $\{|\uparrow s\rangle, |\downarrow s\rangle, |\uparrow\downarrow\rangle, |\downarrow\downarrow\rangle\}$. Then the driving fields Ω_A and Ω_B couple $|\downarrow\uparrow\rangle$ and $|\uparrow\downarrow\rangle$. Consequently, the fields also induce a phase on $|\uparrow s\rangle$ due to the AC Stark and cavity Lamb shifts. Since $|s\rangle_B$ is decoupled from the cavity and far-detuned from the driving fields, we only consider the dynamics in the subspaces affecting $|\uparrow\downarrow\rangle$ and $|\uparrow s\rangle$ dictated by $H_{\uparrow\downarrow}$ and $H_{\uparrow\uparrow}$. From the Hamiltonian, we can write $H_{\uparrow\downarrow}$ in the basis $\{|\uparrow\downarrow 0\rangle, |e\downarrow 0\rangle, |\downarrow\downarrow 1\rangle, |\downarrow e\, 0\rangle, |\downarrow\uparrow 0\rangle\}$ as

$$H_{\uparrow\downarrow} = \begin{pmatrix} 0 & \Omega_A & 0 & 0 & 0 \\ \Omega_A & \Delta_A & g_A & 0 & 0 \\ 0 & g_A & -\delta_A & g_B & 0 \\ 0 & 0 & g_B & \Delta_B + (\delta_B - \delta_A) & \Omega_B \\ 0 & 0 & 0 & \Omega_B & \delta_B - \delta_A \end{pmatrix}, \tag{B24}$$

and $H_{\uparrow\uparrow}$ in the basis $\{|\uparrow s\, 0\rangle, |e\, s\, 0\rangle, |\downarrow s\, 1\rangle\}$ as

$$H_{\uparrow\uparrow} = \begin{pmatrix} 0 & \Omega_A & 0 \\ \Omega_A & \Delta_A & g_A \\ 0 & g_A & -\delta_A \end{pmatrix}, \tag{B25}$$

where $\Delta_k = \omega_k - \omega_{L_k}$ and $\delta_k = \omega_{L_k} + \omega_{g_k} - \omega_C$. The last index of each state indicates the photon number in the cavity mode. To obtain these time-independent subsystem Hamiltonians, we have moved into a rotating frame $\hat{H} \to e^{-it\hat{\mathcal{R}}}\hat{H}(t)e^{it\hat{\mathcal{R}}} - \hat{\mathcal{R}}$ defined by

$$\begin{aligned}\hat{\mathcal{R}} = (\omega_C + \delta_B)\hat{a}^\dagger\hat{a} + \sum_k \omega_{L_k}\hat{\sigma}^\dagger_{\uparrow_k}\hat{\sigma}_{\uparrow_k} + \sum_k \omega_{s_k}\hat{\sigma}^\dagger_{s_k}\hat{\sigma}_{s_k} + \omega_{g_B}\hat{\sigma}^\dagger_{\uparrow\downarrow_B}\hat{\sigma}_{\uparrow\downarrow_B} \\ + (\delta_A - \delta_B - \omega_{g_A})\hat{\sigma}^\dagger_{\uparrow\downarrow_A}\hat{\sigma}_{\uparrow\downarrow_A}.\end{aligned} \tag{B26}$$

This rotating frame preserves the desired relative phase evolution between $|\uparrow\downarrow\rangle$ and $|\uparrow\uparrow\rangle$ because it is defined using local operators only.

The evolution in remaining subsystems can be neglected: $H_{\downarrow\uparrow} = 0$ and $H_{\downarrow\downarrow} = 0$ for the states that are not coupled to the driving fields. Similar to the prevous scheme, the total gate fidelity can then be simplified to $F_{\text{gate}} = (F_\pi + 1)/2$ where $F_\pi = |\langle\phi(T)|\,(|\uparrow\uparrow\rangle - |\uparrow\downarrow\rangle)|/\sqrt{2}$ for initial state $|\psi(0)\rangle = (|\uparrow\uparrow\rangle + |\uparrow\downarrow\rangle)/\sqrt{2}$.

At the two-photon resonance ($\delta_A = \delta_B = \delta$), $H_{\uparrow\downarrow}$ will perform a π-phase rotation on $|\uparrow\downarrow\rangle$. However, unlike the the simple exchange scheme, the Raman exchange scheme can operate when Δ_A and Δ_B are not restricted to a fixed relation, allowing for a gate to be performed between two quantum systems that have unequal optical transitions. However, a π phase can only be achieved when Ω_B is selected to compensate for $g_A \neq g_B$ and $\Delta_A \neq \Delta_B$. By adiabatically eliminating the excited state and cavity amplitudes where we set $d\langle\phi(t)|e{\downarrow}0\rangle/dt = d\langle\phi(t)|{\downarrow\downarrow}1\rangle/dt = d\langle\phi(t)|{\downarrow}e\;0\rangle/dt = 0$, the optimal Rabi frequency relation is found to be

$$\Omega_B = \Omega_A\sqrt{\frac{g_A^2 + \delta\Delta_A}{g_B^2 + \delta\Delta_B}} \simeq \Omega_A\sqrt{\frac{\Delta_A}{\Delta_B}}, \tag{B27}$$

corresponding to the time required to achieve a π phase of

$$T = \pi\frac{g_A^2\Delta_A + g_B^2\Delta_B + \delta\Delta_A\Delta_B}{g_A g_B\Omega_A\Omega_B} \simeq \pi\frac{\delta\Delta_A\Delta_B}{g_A g_B\Omega_A\Omega_B}, \tag{B28}$$

assuming $g_k^2 \ll \delta\Delta_k$.

The non-Hermitian parts are given by corresponding decay rates of each state amplitude

$$\begin{aligned}\hat{\mathcal{H}}_{\uparrow\downarrow} &= \hat{H}_{\uparrow\downarrow} - \frac{i}{2}\left(\gamma\left|e{\downarrow}0\right\rangle\left\langle e{\downarrow}0\right| + \kappa\left|{\downarrow\downarrow}1\right\rangle\left\langle{\downarrow\downarrow}1\right| + \gamma\left|{\downarrow}e\,0\right\rangle\left\langle{\downarrow}e\,0\right|\right)\\ \hat{\mathcal{H}}_{\uparrow\uparrow} &= \hat{H}_{\uparrow\uparrow} - \frac{i}{2}\left(\gamma\left|e\,s\,0\right\rangle\left\langle e\,s\,0\right| + \kappa\left|{\uparrow}s\,1\right\rangle\left\langle{\uparrow}s\,1\right|\right)\end{aligned} \tag{B29}$$

where we have assumed that $\gamma_s \ll \gamma, \kappa$. We analyze the fidelity in the case where $g_A = g_B = g$, $\delta_A \simeq \delta_B \simeq \delta$ but $\delta_\epsilon = |\delta_A - \delta_B| \ll \delta$ is nonzero, $\Delta_A \simeq \Delta_B \simeq \Delta$ but $\Delta_\epsilon = |\Delta_A - \Delta_B| \ll \Delta$ is nonzero, and also $\Omega_A \simeq \Omega_B\sqrt{\Delta_B/\Delta_A} \simeq \Omega$. Under these conditions, and after adiabatically eliminating the state amplitudes that are only virtually populated, the fidelity overlap is found to be

$$\begin{aligned}F_\pi &= \left|\left\langle{\uparrow}s\,0\right| e^{-i\mathcal{H}_{\uparrow\uparrow}T}\left|{\uparrow}s\,0\right\rangle - \left\langle{\uparrow\downarrow}0\right| e^{-i\mathcal{H}_{\uparrow\downarrow}T}\left|{\uparrow\downarrow}0\right\rangle\right|\\ &\simeq e^{-2\pi\delta/C\kappa - \pi\kappa/2\delta}\cosh^2\left[\frac{\pi\kappa}{4\delta}\right] + \mathcal{O}\left(\Delta_\epsilon^2, \delta_\epsilon^2, \gamma_s\right),\end{aligned} \tag{B30}$$

where we assume that $C \gg 1$. Notice that this solution mirrors that of the previous scheme but now the two-photon detuning δ plays the same role that the cavity detuning Δ did prior. The maximum cooperativity-limited fidelity is then given when $2\delta = \kappa\sqrt{C}$. In the regime where $C \gg 1$ and $\gamma_s \ll \gamma$, the maximum fidelity can be expressed as

$$F_{\max} = 1 - \frac{\pi}{\sqrt{C}} - \frac{\pi^2}{16}\left[\frac{T_o^2\delta_\epsilon^2}{4\pi^2} + \frac{\Delta_\epsilon^2}{\Delta^2} - \frac{18}{C}\right] \tag{B31}$$

at the optimal gate time of $T_o = (\Delta/\Omega)^2(2\pi/\gamma\sqrt{C})$.

The maximum fidelity given by equation (B31) relies on the satisfaction of adiabatic criteria. Unlike the previous scheme where $C \gg 1$ and $g \leq \kappa$ was enough to ensure adiabatic evolution in the ideal detuning regime, the Raman process places additional constraints on the driving field parameters to achieve adiabatic evolution. Primarily, it is necessary for $\Omega \ll \Delta$. However, the magnitudes of Δ and Ω are also limited by other system parameters. The lower bound on Δ for a given Ω/Δ ratio can be determined by considering the regime $\delta\Delta < g^2$ where cavity Rabi oscillations cause infidelity. This limit can be solved by adiabatically eliminating both the excited state amplitudes and the cavity mode amplitude. Likewise, the upper bound on Δ for a given Ω/Δ ratio can be determined by considering the regime $\delta\Delta < \Omega^2$ where Rabi oscillations induced by the driving field cause infidelity. These limits can be analytically solved by adiabatically eliminating only the excited state amplitudes.

In the ideal regime where $\gamma_s/\gamma \ll 2(\Omega/\Delta)^2$, $\Delta_A \simeq \Delta_B$, and $\delta_\epsilon \ll 2\pi T_o^{-1}$, the total gate fidelity is well-approximated by

$$\begin{aligned} F_{\text{gate}} \simeq & \frac{1}{2}\left(\cos^2\left[\frac{\pi\Omega}{4\Delta}\right]\cos^2\left[\frac{\pi\Omega^2}{2\delta\Delta}\right]\sin\left[\frac{\pi/2}{1+g^2/\delta\Delta}\right]F_\pi + 1\right) \\ \simeq & \, F_{\max} - \frac{\pi^2}{16}\left(\frac{\Omega^2}{2\Delta^2} + \frac{2\Omega^4}{\delta^2\Delta^2} + \frac{g^4}{\delta^2\Delta^2}\right) \end{aligned} \tag{B32}$$

where the additional $-\Gamma T_o$ scaling can be added to account for decoherence infidelity. These extra constraints on the adiabatic evolution are independent of the cavity cooperativity but they do place bounds on the regime where the fidelity is only limited by the cavity cooperativity. In addition, they will place bounds on the gate time. Combining the results from equations (B30) and (B32) provides a very accurate estimate of the fidelity given by the non-Hermitian Hamiltonian, as shown by the black dashed line in figure 4.6 of the main text.

The upper bound on Δ will dictate the maximum possible spectral separation of the optical transitions. In turn, for a fixed Ω/Δ ratio, Δ is limited by the condition $\pi\Delta < \delta(\Delta/\Omega)^2$ needed to maintain adiabatic evolution and the ratio Ω/Δ itself is limited from below by decoherence due to the gate time scaling of $T \propto (\Delta/\Omega)^2$. To solve for the minimum Δ/Ω and maximum Δ corresponding to the maximum Δ_ϵ, we optimize the expression

$$\frac{2\pi\Gamma\Delta^2}{\gamma\Omega^2\sqrt{C}} + \frac{\pi^2\Omega^4}{8\delta^2\Delta^2} + \frac{\pi^2\Delta_\epsilon^2}{16\Delta^2} = \frac{\pi}{\sqrt{C}} \tag{B33}$$

when $2\delta = \kappa\sqrt{C}$, where the first term is the infidelity ΓT_o due to the effective decoherence Γ, the second term captures the condition $\Delta > \Omega$ from equation (B32) to maintain adiabatic evolution, and the third term captures the infidelity from equation (B31) due to spectral separation of the optical transitions. From this expression, we find that the maximum spectral separation that will result in an infidelity less than the cooperativity-limited value is

$$\Delta_\epsilon = \frac{\kappa\gamma}{\pi\Gamma\sqrt{8}}, \tag{B34}$$

which corresponds to $\Omega/\Delta = 2\sqrt{\Gamma/\gamma}$ and $2\Delta = \Delta_\epsilon\sqrt{\pi\sqrt{C}}$. This implies that $\Delta_A/\Delta_B \simeq 1 \pm \sqrt{2/\pi\sqrt{C}}$, which validates the initial assumption that $\Delta_\epsilon \ll \Delta$. The corresponding gate time for these conditions is $T = \pi/(2\Gamma\sqrt{C})$.

In the adiabatic regime, the emission of a photon will collapse the system into the mixed state $\hat{\rho}_{\gamma\kappa} \simeq (1/2)\left|\downarrow\right\rangle\left\langle\downarrow\right|_A \otimes (\left|\downarrow\right\rangle\left\langle\downarrow\right| + \left|\mathrm{s}\right\rangle\left\langle\mathrm{s}\right|)_B$. Hence the fidelity for a failure is $F_{\gamma\kappa} = 1/2$. This implies that the maximum error in the non-Hermitian solution F_{gate} given above is $\sqrt{F_{\mathrm{gate}}^2 + (1 - F_{\mathrm{gate}}^2)/4} - F_{\mathrm{gate}} \sim \pi/4\sqrt{C}$. For example, where the non-Hermitian approximation gives 0.9 (0.99), the true fidelity from the full master equation is not more than 0.93 (0.993).

Chapter 5

Paper 3: Protocols for long-distance quantum communication with single ^{167}Er ions

5.1 Preface

Quantum repeaters, essential components of a future global quantum network, will likely require long-lived quantum memories to store the entanglement. These memories also need to interface with photons in order to allow long-distance transmission of the quantum states. ^{167}Er ions offer both nuclear spin coherence times in the one-second range and photon emission in the low-loss telecommunications window. Here we propose a quantum repeater architecture based on single ^{167}Er ions doped into photonic crystal cavities. We show that our proposal offers excellent performance and relative ease of implementation.

In this work, I proposed the quantum repeater scheme, performed the repeater rate and fidelity calculations and wrote the first draft of the manuscript.

Protocols for long-distance quantum communication with single ^{167}Er ions

Quantum Science and Technology 5, 045015 (2020)

F. Kimiaee Asadi, S. Wein, and C. Simon

Institute for Quantum Science and Technology,and Department of Physics* & *Astronomy, University of Calgary, 2500 University Drive NW, Calgary, Alberta T2N 1N4, Canada

Abstract

We design a quantum repeater architecture using individual ^{167}Er ions doped into Y_2SiO_5 crystal. This ion is a promising candidate for a repeater protocol because of its long hyperfine coherence time in addition to its ability to emit photons within the telecommunication wavelength range. To distribute entanglement over a long distance, we propose two different swapping gates between nearby ions using the exchange of virtual cavity photons and the electric dipole-dipole interaction. We analyze their expected performance, and discuss their strengths and weaknesses. Then, we show that a post-selection approach can be implemented to improve the gate fidelity of the virtual photon exchange scheme by monitoring cavity emission. Finally, we use our results for the swapping gates to estimate the overall fidelity and distribution rate for the protocol.

5.2 Introduction

Future quantum networks will require the ability of long-distance communication [5, 6, 111]. Although we have an existing global fiber optics network for classical communication, the bottleneck for long-distance quantum communication is the unavoidable transmission loss through fibers. Classical communication overcomes this problem by amplifying signals, however, due to the no cloning theorem the use of amplifiers is prohibited in quantum communication. Therefore, to circumvent this exponential decay of transmitted photons, the use of a quantum repeater has been suggested [7, 19]. Quantum repeaters aim to establish entanglement between two distant locations. Most of the quantum repeater protocols that have been proposed so far focus on atomic ensemble-based quantum memories and linear optics for entanglement generation and distribution [18]. This is an attractive route as it requires only a few relatively simple components. However, when using linear optics, the success probability for entanglement swapping cannot exceed 1/2, resulting in relatively low entanglement distribution rates. Using single-emitter-based quantum repeater protocols, on the other hand, one can perform entanglement swapping with a higher success probability[155, 45, 114, 156, 157, 158].

Several works have demonstrated the ability to individually address single rare-earth (RE) ions [20, 23, 21, 22, 66]. RE ions in general have a smaller sensitivity to lattice phonons and experience little spectral diffusion [61] compared to quantum dots and NV centers in diamond. In addition, most other quantum systems, require the use of microwave (MW) to optical transducers e.g., superconducting qubits [158] or the frequency down conversion to telecommunication wavelength, for instance, in defects in diamond and quantum dots [159, 160], to match the low-loss wavelength range of fibers (needless to say that, there are still certain quantum dots such as InAs/InP quantum dot [161], and defects like T-center and G-center defects in silicon [162, 163], which emit photons at telecom wavelengths). However, the erbium (Er) RE ion has a unique feature, which is its ability to emit photons in the conventional telecommunication wavelength window. Moreover, significant enhancements of RE ion emission rates, including Er, have been demonstrated [66, 164, 165, 166, 81].

In ^{168}Er with zero nuclear spin, the relevant coherence time is that of the electronic spin. Therefore, until recently, one challenge for using an ^{168}Er ion as a quantum memory was its short spin coherence time. For a single ^{168}Er ion doped in yttrium orthosilicate Y_2SiO_5

crystal (^{168}Er:YSO) in the presence of a strong magnetic field, a spin coherence lifetime of a few milliseconds is expected in low temperatures, which is not quite long enough for a repeater protocol. Therefore, in our previous work, we proposed a quantum repeater architecture combining an individual ^{168}Er ion and europium (^{151}Eu) RE ion, which serve as a spin-photon interface and long-term memory, respectively [114]. In this scheme to perform a swapping gate using the electric dipole-dipole interaction, Er-Eu ions should be close-lying. Hence, fabricating and identifying suitable Er-Eu ion pairs is a main challenge of this scheme.

Recently, a hyperfine coherence time of 1.3 s has been measured for an ensemble of ^{167}Er:YSO using a strong external magnetic field [92]. Instead of applying a large magnetic field, it is also possible to extend the coherence time using the zero first-order Zeeman (ZEFOZ) technique. For the ^{167}Er ion, transitions with ZEFOZ shift exist with and without the external magnetic field [167]. The long hyperfine coherence time of ^{167}Er suggests that it could serve as both the spin-photon interface emitting telecom photons and the long-lived quantum memory needed to implement a repeater protocol. These advantages, in addition to the narrow optical transitions, have made ^{167}Er:YSO a very promising material platform for quantum communication.

In this paper, we propose and analyze a scheme to design quantum repeaters using single ^{167}Er ions. We consider individual ^{167}Er ions doped into a high quality factor YSO photonic crystal cavity. The presence of the cavity improves the intrinsic low radiative decay rate of the Er ion, increases the single-photon indistinguishability, and enhances the collection of photons into the desired transmission channel. We first explain how to generate entanglement between remote ^{167}Er ions over elementary links. Entanglement swapping between two ions within each cavity is then performed to extend the range of entanglement to successively longer distances. Building on earlier work, we propose two different schemes to perform the entanglement swapping step of the repeater protocol deterministically. In the first scheme the controlled interaction between ions is achieved by the exchange of virtual cavity photons. In the second scheme the interaction is mediated by the electric dipole-dipole interaction between the ions. We also propose a method to improve the fidelity of the first scheme at the cost of some efficiency by monitoring cavity emission in order to post-select successful gates. We then determine the fidelity of each swapping gate scheme and finally estimate the end-to-end fidelity of the proposed single Er repeater protocol.

The paper is organized as follows: In Sec 5.3, we introduce our quantum repeater protocol. Sections 5.4 and 5.5 deal with the estimation of the fidelity and efficiency, and the entanglement generation rate of the repeater protocol, respectively. The implementation of the protocol as well as the advantages and disadvantages of each of the entanglement swapping schemes are discussed in Sec.5.6. We conclude with future directions in Sec. 5.7

5.3 Proposal

Each node consists of an optical cavity fabricated in the YSO host crystal that is doped with a pair of ^{167}Er ions.

In the presence of a strong magnetic field along the D_1 axis and temperature of 1.6 K or less, the ground state electron spin freezes at the lower level. In our scheme, the $m_I = \frac{7}{2}$ and $m_I = \frac{5}{2}$ hyperfine states of the lowest spin state are used as qubit states $|\uparrow\rangle$ and $|\downarrow\rangle$, respectively, as shown in Fig5.1.b. The oscillator strength for $\Delta m_I = -1(+1)$ transitions relative to the $\Delta m_I = 0$ is about 2.5% (3.1%) for transitions involving the $m_I = \frac{7}{2}$ hyperfine state [92]. Therefore, with the use of a cavity, it is possible to utilize an L-type system, where the excited state has a high probability to decay to the initial ground state. This probability can be further increased by using a resonant cavity and therefore, we can ignore the other weak transitions.

5.3.1 Entanglement Generation

To generate entanglement over an elementary link between Er ions in remote cavities, such as Er_i and Er_{i-1}, we follow the same scheme as [73, 24]. Initially, the $|\uparrow\rangle$–$|e\rangle$ transition of

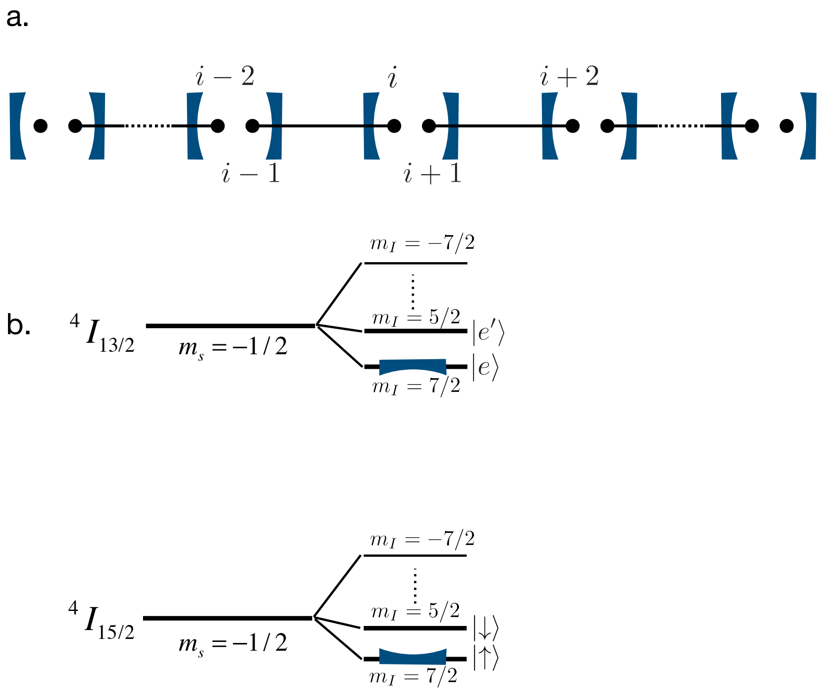

Figure 5.1: **a.** In each cavity there is a pair of ^{167}Er ions (black circles). Black lines represent entanglement between degenerate ions over elementary links. **b.** Energy level structure of the ion. In each ion the $|\uparrow\rangle$–$|e\rangle$ transition is coupled to the cavity.

each ion is coupled to its respective cavity. First, both ions are optically pumped into the $m_I = \frac{7}{2}$ hyperfine ground state.

Using optical Raman pulses, each ion is then prepared in the superposition of $|\uparrow\rangle$ and $|\downarrow\rangle$ states. Ions are then excited to the $|e\rangle$ state using a short laser pulse resonant with the $|\uparrow\rangle$–$|e\rangle$ transition. After sufficient time has passed to allow a possible photon to be emitted through the cavity mode, optical Raman pulses are applied to flip the qubit state. This is followed by another optical excitation to the $|e\rangle$ state to emit a possible photon. The second round of excitation is key to overcoming infidelity caused by photon loss in the fiber in the event that both ions emit a photon. The emitted photons are then collected and transmitted to a beam splitter located half-way in between the ions. The detection of two consecutive single photons will then leave remote ions in an entangled Bell state [168]

$$|\psi^{\pm}\rangle_{Er_i,Er_{i-1}} = \frac{1}{\sqrt{2}}(|\uparrow\downarrow\rangle \pm |\uparrow\downarrow\rangle). \tag{5.1}$$

Here the sign + (-) depends on whether the same (different) detectors detect photons.

5.3.2 Entanglement swapping

After generating entanglement over elementary links, entanglement is swapped between nearby ions within each cavity (e.g., Er$_i$ and Er$_{i+1}$ in Fig. 5.1.a). This can be done by performing a CNOT gate between the ions and then measuring the control (target) ion in the X (Z) basis. Measurement in the Z basis is achieved by the optical excitation of ions from the ground state $|\uparrow\rangle$ to the excited state $|e\rangle$ while this transition is coupled to the cavity. To perform the spin readout in X basis, we need to coherently rotate the ion (to make $|\downarrow\rangle \rightarrow 1/\sqrt{2}(|\downarrow\rangle - |\uparrow\rangle)$ and $|\uparrow\rangle \rightarrow 1/\sqrt{2}(|\uparrow\rangle + |\downarrow\rangle)$) followed by a measurement in the Z basis. Depending on the result of measurements (i.e., $|\uparrow\rangle$ or $|\downarrow\rangle$), and the initial entangled states over elementary links (i.e., $|\psi^{\pm}\rangle$ given in Eq.5.1), the entangled state between the outer nodes will be projected onto a Bell state.

In the following, we analyze two different approaches to achieve the required interaction to perform a CNOT gate between ions. Performing a deterministic gate using the virtual exchange of photons is discussed in the following. We also discuss how monitoring the cavity emission can improve the fidelity of this scheme. Then, we explain another scheme to perform a deterministic gate using the electric dipole-dipole interaction.

5.3.2.1 Virtual Photon Exchange

Since both Er ions of a single node are coupled to the same cavity, the interaction between these two ions can be mediated by the exchange of virtual cavity photons [169, 129]. Using this method, it is possible to perform a controlled phase-flip (CZ) gate between Er ions. A CZ gate combined with two Hadamard gates can then be used to perform a CNOT gate; $H_{Er_{i+1}} \otimes CZ_{Er_i, Er_{i+1}} \otimes H_{Er_{i+1}}$.

To perform the CZ gate, the $|\uparrow\rangle$–$|e\rangle$ transitions of the ions are brought into resonance while both are dispersively coupled to a cavity mode (with the cavity detuning Δ). Then,

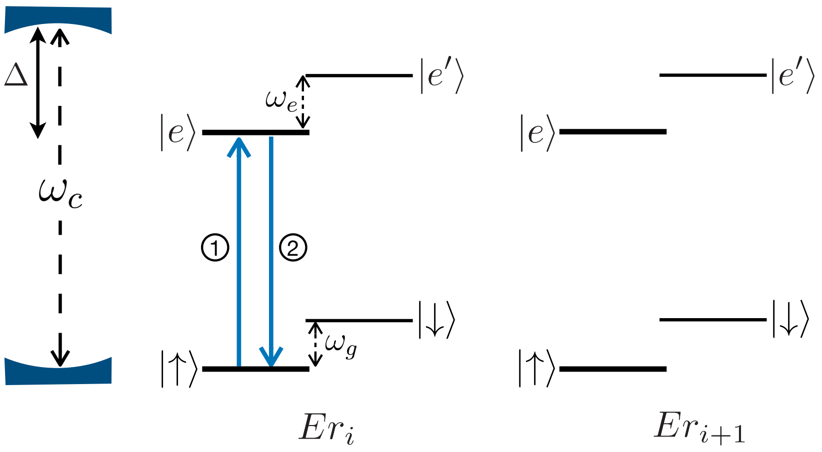

Figure 5.2: To perform a CZ gate using the virtual photon exchange, we bring the $|\uparrow\rangle$–$|e\rangle$ transition of the ions into resonance with each other while ions are dispersively coupled to the cavity. Using an optical π pulse, we then excite one of the ions and let the exchange of virtual cavity photons perform a π phase shift on the state.

we excite the first ion using an optical π pulse resonant with the $|\uparrow\rangle$–$|e\rangle$ transition, as shown in Fig.5.2. If the joint state of the ions was $|\uparrow\uparrow\rangle$, then after exciting the ion, the virtual exchange of a cavity photon between degenerate states $|\uparrow e\rangle$ and $|e\uparrow\rangle$ adiabatically performs a π phase shift on the state. Finally, another optical π pulse brings the excited qubit back to the ground state after a delay time.

So long as the splitting between states $|e\downarrow\rangle$ and $|\uparrow e'\rangle$ (which is $\delta_{eg} = (w_e - w_g)$) is large enough and the system has negligible spin-flip transitions coupled to the cavity, the other joint states of ions will not be affected by the pulses 1 and 2 [169]. The unitary operator of this phase-flip gate can be written as $U_{CZ_{(Er_i,Er_{i+1})}} = -|\uparrow\uparrow\rangle\langle\uparrow\uparrow| + |\uparrow\downarrow\rangle\langle\uparrow\downarrow| + |\downarrow\uparrow\rangle\langle\downarrow\uparrow| + |\downarrow\downarrow\rangle\langle\downarrow\downarrow|$.

After performing the CNOT gate, to complete the swapping process we measure Er_i in the X basis and Er_{i+1} in the Z basis.

The two main processes limiting the fidelity of the CZ gate are cavity mode dissipation and spontaneous emission. If the cavity detuning is too small, the Purcell enhancement will cause the ions to decay into the cavity mode before the completion of the phase flip. On the other hand, if the detuning is too large, the dissipative interaction will be too slow to complete the phase flip before spontaneous emission occurs. The former limitation can be relaxed if the cavity emission is efficiently collected and monitored during the gate. Doing so allows for the rejection of gate attempts where cavity emission occurred, thus improving fidelity at the cost of some efficiency. Adding such a post-selection scheme also allows for the scheme to be performed with a smaller cavity detuning, which in turn, decreases the gate time and makes the scheme more robust against other decoherence processes.

5.3.2.2 Electric dipole-dipole interaction

Optically exciting an Er ion changes its permanent electric dipole moment. As a result, the electric field environment around the ion will change. This change in the local electric field can impact other nearby ions by shifting their optical transition frequencies by [76]:

$$\Delta\nu = \frac{\Delta\mu_{Er_i}\Delta\mu_{Er_{i+1}}}{4\pi\epsilon\epsilon_0 h r^3}\left(\left(\hat{\mu}_{Er_i}\cdot\hat{\mu}_{Er_{i+1}}\right) - 3\left(\hat{\mu}_{Er_i}\cdot\hat{r}\right)\left(\hat{\mu}_{Er_{i+1}}\cdot\hat{r}\right)\right), \tag{5.2}$$

where Er_i is the excited ion, Er_{1+i} is its nearby ion, $\Delta\mu$ is the change of the permanent electric dipole moment, r is the distance between ions, ϵ_0 is vacuum permittivity, h is the Planck constant, and ϵ is the dielectric constant. Using this modification in the transition frequency, one can perform a deterministic CNOT gate between nearby qubits. For both ions, we consider that the transition $|\uparrow\rangle$–$|e'\rangle$ is detuned from the cavity. First, we apply a short optical π pulse resonant with the $|\uparrow\rangle$–$|e'\rangle$ transition of the control ion (e.g., Er_i), as shown in Fig. 5.3. Then, using pulses 2–4, we swap population in the target ion. Finally, pulse 5 brings the control ion back to its ground state.

This process can be interrupted by the electric dipole-dipole interaction if i) the control ion is in the state $|\uparrow\rangle$ and ii) the ions are sufficiently close to each other. In this case, if the shift in the transition frequency $\Delta\nu$ of the target ion is large compared to the transition linewidth, pulses 2–4 do not affect the system [75, 170].

The overall result of this interaction is that the state of the target qubit is flipped if the control qubit is in the state $|\downarrow\rangle$. After performing the CNOT gate, we need to also measure

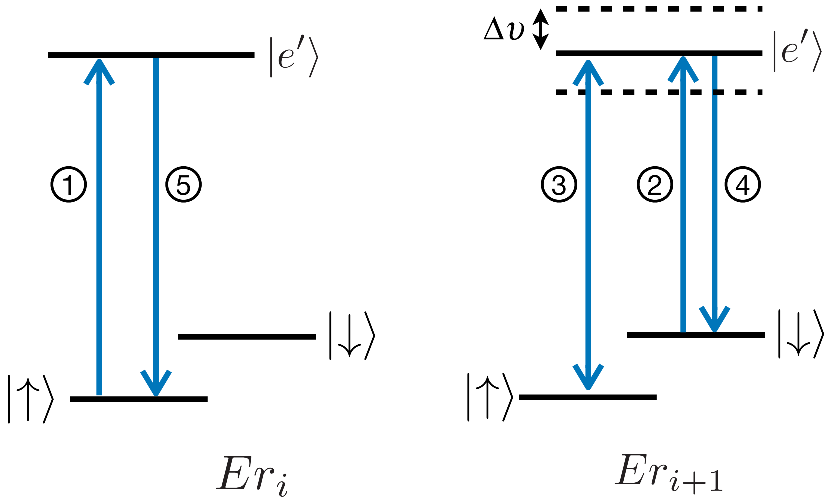

Figure 5.3: Pulse sequence to perform a CNOT gate between close-lying Er_i (control) and Er_{1+i} (target) ions. When Er_i is in the state $|\uparrow\rangle$, due to the electric dipole-dipole interaction pulses 2-4 have no effect of the target ion. Please note that all pulses shown here are optical π pulses. The double arrow for pulse 3 illustrates that the pulse can either take the state $|\uparrow\rangle$ to $|e\rangle$ or $|e\rangle$ to $|\uparrow\rangle$.

the control (target) ion in the X (Z) basis.

5.4 Fidelity and efficiency

Here we estimate the fidelity and efficiency for each step as well as the end-to-end fidelity of the protocol. We also show numerically how the fidelity of the virtual photon exchange swapping gate can be improved by monitoring the cavity emission. In this section, fidelity is computed as $F = \langle\psi|\,\hat{\rho}\,|\psi\rangle$, where $\hat{\rho}$ is the imperfect final state and $|\psi\rangle$ is the expected pure state.

5.4.1 Entanglement generation

When spin decoherence is negligible on the time scale of the optical dynamics, and the system operates in the bad-cavity regime, the fidelity of the Barrett-Kok entanglement generation scheme between two ions identical other than for emission wavelength is given by [168]:

$$F_{\text{entangle}} = \frac{1}{2}\left(1 + \frac{\gamma'^2}{\Gamma'^2 + \Delta_w^2}\right), \tag{5.3}$$

where $\gamma' = \gamma_r F_p + \gamma$ is the Purcell-enhanced optical decay rate of the ion in the presence of the cavity, $\gamma = \gamma_r + \gamma_{nr}$ is the bare ion decay rate, γ_r (γ_{nr}) is the radiative (non-radiative) component of the decay rate, $\Gamma' = \gamma' + 2\gamma^\star$ is the FWHM of the Purcell-enhanced zero-phonon line (ZPL), and Δ_w is the difference between the optical transition frequencies of the ions. We define $\gamma^\star$ as the optical pure dephasing rate and $F_p = R/\gamma_r$ as the Purcell factor, where $R = 4g^2/(\kappa+\Gamma)$ is the effective transfer rate of population between the ion and cavity [101], $\Gamma = \gamma + 2\gamma^\star$ is the FWHM of the ZPL before enhancement, g is the cavity-ion coupling rate, and κ is the cavity decay rate. In the regime where $\kappa \gg \Gamma$, the Purcell factor can be written as $F_p = 4g^2/(\gamma_r\kappa)$.

The entanglement generation fidelity is related to the mean wavepacket overlap M' of Purcell-enhanced photons from each ion $M' = \Gamma'\gamma'/(\Gamma'^2 + \Delta_w^2)$ [168] by $F_{\text{entangle}} = (1+M'I')/2$ where $I' = \gamma'/\Gamma'$ is the indistinguishability of the Purcell-enhanced photons from one ion. Note that the fidelity is less than or equal to $(1 + M')/2$, which would be the expected fidelity when accounting for interference visibility only [24]. This is because the optical pure dephasing of the emitter degrades both the temporal coherence of the emitted photons and the spin coherence of the ion state as a consequence of the spin-photon entanglement. Knowing this, the quantity I' in F_{entangle} actually accounts for the degredation of the ion spin coherence while $M' \leq I'$ quantifies the reduced interference visibility of photons from separate ions. In general, to have high interference visibility, spectral diffusion of the optical transition needs to be controlled. In our system, however, we expect the spectral diffusion to be negligible (see Sec.5.6.1 for more information).

The presence of the cavity helps improve the single-photon indistinguishability as $I' = I(1+\zeta F_p)/(1+I\zeta F_p)$ where $I = \gamma/\Gamma$ is the single-photon indistinguishability in the absence

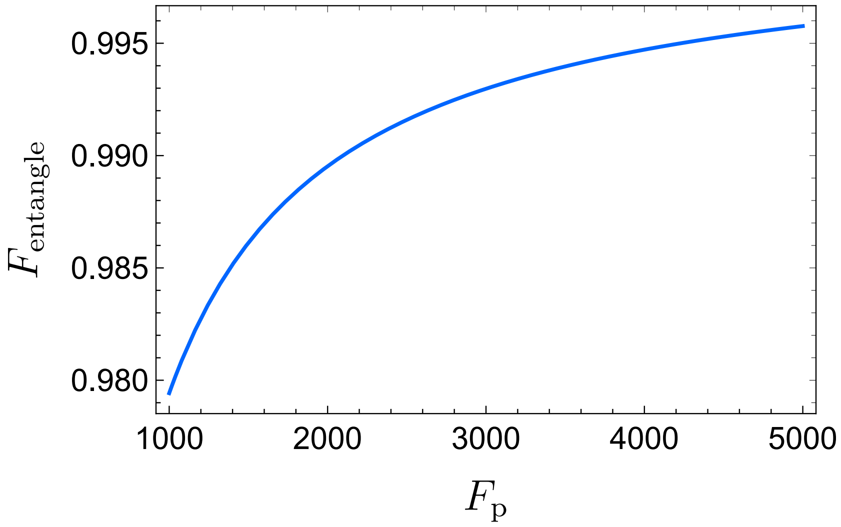

Figure 5.4: Fidelity of the entanglement generation scheme with respect to the Purcell factor. Here we assume $\Delta_w = 0$.

of the cavity and $\zeta = \gamma_r/\gamma$. This in turn improves the mean wavepacket overlap and consequently improves the entanglement generation fidelity (see Fig. 5.4).

We estimate $\gamma^\star$ using the relation $\gamma^\star = 1/T_2 - \gamma/2 = 2\pi \times 32$ Hz, where $T_2 = 4$ ms is the optical coherence time (for B=7 T) [102], and $\gamma = 2\pi \times 14$ Hz [25]. Considering $\gamma_r = 2\pi \times 3$ Hz [74], $\gamma_{nr} = 2\pi \times 11$ Hz and $\Delta_\omega = 0$ the entanglement generation fidelity would be F_{entangle} =0.996 for $F_p = 5000$, as shown in Fig. 5.4.

The entanglement generation efficiency is given by $p_{\text{en}} = \eta^2/2$, where $\eta = p\eta_t\eta_d$, $p = \eta_c F_p \gamma_r/\gamma'$ is the success probability of single-photon emission into a collection fibre mode (see Sec. 5.6.3), η_c is the collection efficiency, $\eta_t = e^{-\frac{L_0}{2L_{att}}}$ is the transmission efficiency in the fibre, $L_{att} \approx 22$ km is the attenuation length (corresponding to a loss of 0.2 dB/km), and η_d is the detection efficiency.

Before the first entanglement generation attempt and then again after every unsuccessful attempt, the ions must be initialized in the ground state $|\uparrow\rangle$. For an ion in a cavity with a large Purcell enhancement, the initialization fidelity after applying a single pulse exciting all ground states other than $|\uparrow\rangle$ to $|e\rangle$ is given by $F_{\text{init}} \geq (\gamma_r F_p + \beta\gamma)(1 - e^{-T_{\text{init}}\gamma'})/\gamma'$ where T_{init} is the initialization time needed for the excited state to decay and $\beta \geq 0.9$ is the branching ratio without a cavity [87]. For $F_p = 5000$ and $T_{\text{init}} = 8/\gamma' = 85\mu$s the fidelity can be as high as $F_{\text{init}} \geq 0.9996$. This small infidelity is negligible compared to F_{entangle}, however T_{init} can slightly reduce the repeater rate for small distances (see Sec. 5.5 for more information). For this fidelity estimation, we ignore the ground state T_1 thermalization time, which is on the order of seconds [92] and is negligible compared to the Purcell-enhanced lifetime.

5.4.2 Virtual photon exchange

While performing the CNOT gate, there is always some infidelity due to the Hadamard gates which do not depend on the scheme. Here we assume the the fidelity of the CNOT gate will be dominated by the phase gate step. In the absence of excess dephasing and in the bad-cavity regime where $\kappa > g$, the cooperativity-limited gate fidelity is $F_{\max} = 1 - 2\pi/\sqrt{C}$ [169] where $C = 4g^2/(\kappa\gamma) \gg 1$. This limit is reached when the ions are detuned from the cavity by $\Delta = \kappa\sqrt{C}/2$, which implies that the gate time $T_{\text{gate}} = \pi\Delta/g^2$ becomes $T_0 = 2\pi/(\gamma\sqrt{C})$ under the optimal conditions. Note that in this work we define fidelity to be consistent with Ref. [168] and so it is the square of the fidelity as defined in Ref. [169]. Hence some expressions in this section differ from that of Ref. [169] accordingly.

A slight detuning Δ_w between ions within the cavity or incidental cavity coupling of another transition detuned by δ_{eg} can both cause imperfections in the phase evolution of the CZ gate. To lowest order for the infidelity contributions due to finite C, Δ_w, and δ_{eg} the gate fidelity maximum is given by [169]

$$F_{\max} = 1 - \frac{2\pi}{\sqrt{C}} - \frac{6\pi^2}{32}\left[\left(\frac{T_0\Delta_w}{2\pi}\right)^2 + \left(\frac{2\pi}{T_0\delta_{eg}}\right)^2\right]. \tag{5.4}$$

These imperfections reduce the maximum achievable fidelity but they do not change the ideal ion-cavity detuning. On the other hand, some excess dephasing can both reduce the maximum fidelity and favor shorter gate times, which in turn reduces the optimal ion-cavity detuning.

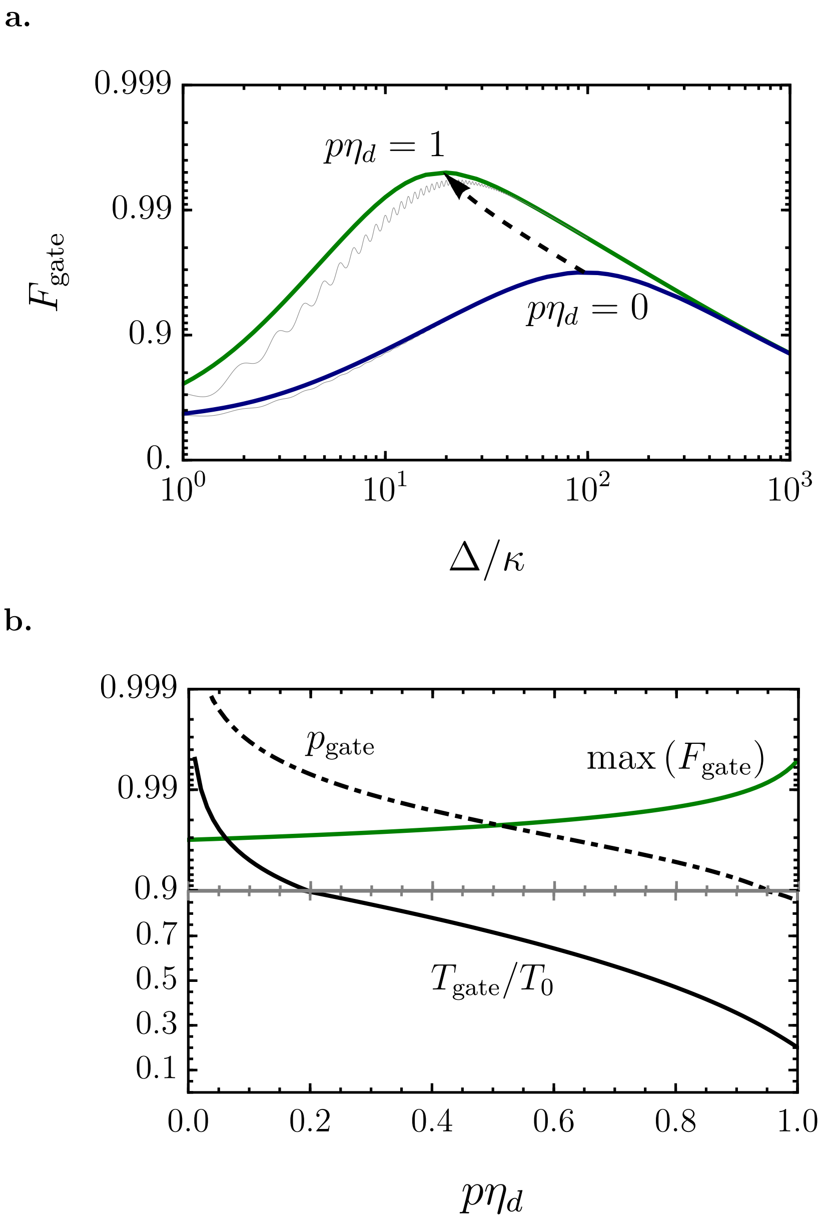

Figure 5.5: Cavity-mediated virtual photon exchange controlled phase-flip gate. **a.** Phase-flip gate fidelity F_{gate} as a function of cavity detuning Δ for no post-selection (blue curve, $p\eta_d = 0$) and perfect post-selection (green curve, $p\eta_d = 1$) of gates where no emission was observed from the cavity. The black dashed arrow shows the path that the fidelity peak follows when increasing the cavity monitoring efficiency $p\eta_d$ from 0 to 1 in the direction of the arrow. The thin gray lines show the case where $\delta_{eg} = \kappa/50$ as opposed to $\delta_{eg} \gtrsim \kappa$ of the colored solid lines. **b.** The maximum fidelity for a given monitoring efficiency $p\eta_d$ corresponding to the dashed arrow in panel a. plotted alongside the corresponding gate efficiency p_{gate} and gate time T_{gate}/T_0 where T_0 is the optimal gate time for the case of no post-selection ($p\eta_d = 0$). The cavity mediating the interaction is in the bad cavity regime with $g/\kappa = 10^{-1}$ and a cooperativity of $C = 9 \times 10^4$. For this simulation we assumed an optical pure dephasing rate of $\gamma^\star = 2.3\gamma$ for both ions.

Although the methods used in Ref. [169] cannot directly analytically account for the excess optical pure dephasing of Er ions, in the regime where the gate time T_{gate} is small compared to $1/\gamma^\star$, the resulting infidelity is proportional to $T_{\text{gate}}\gamma^\star$. Using the solution for the detuning-dependent fidelity of Ref. [169], we find that the gate fidelity for when $T_{\text{gate}}\Delta_w \ll 2\pi$ and $T_{\text{gate}}\delta_{eg} \gg 2\pi$ that includes pure dephasing is closely approximated by

$$F_{\text{gate}} = \frac{1}{4}(e^{-2\pi\Delta/C\kappa - \pi\kappa/2\Delta} + 1)^2 - 0.29\gamma^\star T_{\text{gate}}, \tag{5.5}$$

where $C = 4g^2/(\kappa\gamma)$ is the cavity cooperativity when neglecting pure dephasing and T_{gate} can be written in terms of C as $T_{\text{gate}} = 4\pi\Delta/(C\kappa\gamma)$. The coefficient 0.29 is an estimate obtained by comparing the analytic approximation to the numeric solution from simulating the master equation far in the bad-cavity regime.

Alternatively, optical pure dephasing can be seen to effectively reduce the cavity cooperativity. However, because pure dephasing does not affect the gate fidelity in the same way as spontaneous emission, replacing C by the usual definition for the reduced cavity cooperativity $4g^2/(\kappa\Gamma)$ is not accurate. Instead, we find that replacing C by the quantity $C^\star = C\gamma/(\gamma + 0.61\gamma^\star)$ provides an accurate analytic approximation, where again the coefficient 0.61 is estimated by comparison to the full numeric solution. The fact that 0.61 is smaller than 2 suggests that pure dephasing has much less of a degrading effect than would be naively expected. The maximum fidelity when accounting for pure dephasing then becomes $F_{\text{max}} = 1 - 2\pi/\sqrt{C^\star}$ and is achieved at the detuning $\Delta = \kappa\sqrt{C^\star}/2$ which implies an optimal gate time of $T_0 = \pi\kappa\sqrt{C^\star}/(2g^2) = 2\pi\sqrt{C^\star}/(C\gamma)$.

For a given cavity cooperativity, the maximum fidelity for the virtual photon exchange gate can be increased if successful attempts are post-selected when no cavity emission is observed during the interaction. To estimate the amount of improvement, we numerically simulated the state of the system given that a detector monitoring the cavity mode emission did not measure a photon.

We consider the Hamiltonian in [169]: $\hat{H} = \hat{H}_A + \hat{H}_B + \hat{H}_C + \hat{H}_I$ where $\hat{H}_k$ is the k^{th} ion Hamiltonian, $\hat{H}_C$ is the cavity mode Hamiltonian and $\hat{H}_I$ is the cavity-ion interaction. The four-level ion Hamiltonian is

$$\hat{H}_k = \omega_k \hat{\sigma}^\dagger_{\uparrow_k}\hat{\sigma}_{\uparrow_k} + (\omega_k + \omega_e)\hat{\sigma}^\dagger_{\downarrow_k}\hat{\sigma}_{\downarrow_k} + \omega_g \hat{\sigma}^\dagger_{\uparrow\downarrow_k}\hat{\sigma}_{\uparrow\downarrow_k}, \tag{5.6}$$

where ω_k is the frequency separation between $|\uparrow\rangle_k$ and $|e\rangle_k$, ω_e is the separation between $|e\rangle_k$ and $|e'\rangle_k$, and ω_g is the separation between $|\uparrow\rangle_k$ and $|\downarrow\rangle_k$. Also, $\hat{\sigma}_{\downarrow_k}|e'\rangle_k = |\downarrow\rangle_k$, $\hat{\sigma}_{\uparrow_k}|e\rangle = |\uparrow\rangle_k$, and $\hat{\sigma}_{\uparrow\downarrow_k}|\downarrow\rangle_k = |\uparrow\rangle_k$ (see figure 5.2). The cavity homogeneous evolution is $\hat{H}_C = \omega_c \hat{a}^\dagger \hat{a}$ for cavity frequency ω_c, cavity photon creation (annihilation) operator $\hat{a}^\dagger$ ($\hat{a}$), and the interaction term is

$$\hat{H}_I = \sum_{j\in\uparrow,\downarrow}\sum_{k\in A,B} g_{j_k}\hat{\sigma}^\dagger_{j_k}\hat{a} + \text{h.c.}, \tag{5.7}$$

where $g_{\downarrow_k}$ is the cavity coupling rate of the $|\downarrow\rangle$–$|e'\rangle$ transition to the cavity mode and $g_{\uparrow_k}$ is the cavity coupling rate of the $|\uparrow\rangle$–$|e\rangle$ transition to the cavity mode. In addition to the spontaneous emission rate γ_k and cavity linewidth κ, we explicitly include an optical pure dephasing rate $\gamma^\star$ in the total Lindblad master equation given by

$$\dot{\rho} = -i[\hat{H}, \hat{\rho}] + \kappa\mathcal{D}(\hat{a})\hat{\rho} + \sum_{k,j}\gamma_{j_k}\mathcal{D}(\hat{\sigma}_{j_k})\hat{\rho} + 2\gamma^\star_k\mathcal{D}(\hat{\sigma}^\dagger_{\uparrow_k}\hat{\sigma}_{\uparrow_k} + \hat{\sigma}^\dagger_{\downarrow_k}\hat{\sigma}_{\downarrow_k})\hat{\rho} \tag{5.8}$$

where $\mathcal{D}(\hat{A})\hat{\rho} = \hat{A}\hat{\rho}\hat{A}^\dagger - \{\hat{A}^\dagger\hat{A}, \hat{\rho}\}/2$. This master equation defines the superoperator $\mathcal{L}$ where $\dot{\rho} = \mathcal{L}\hat{\rho}$.

Using the method of conditional evolution [171, 172, 168] the unnormalized conditional state $\hat{\rho}_0(t)$ at time t given that no emission was observed from the cavity since time t_0 is

$$\hat{\rho}_0(t) = e^{(t-t_0)(\mathcal{L}-p\eta_d\kappa\mathcal{S})}\hat{\rho}(t_0) \tag{5.9}$$

where $\mathcal{S}\hat{\rho} = \hat{a}\hat{\rho}\hat{a}^\dagger$ is the cavity photon collapse superoperator, p is the probability of receiving a photon emitted by the cavity and η_d is the detector efficiency. Then the probability that no photon is emitted from the cavity during the gate duration $t - t_0 = T_{\text{gate}} = \pi\Delta/g^2$ is

$$p_{\text{gate}}(T_{\text{gate}}) = \text{Tr}(\hat{\rho}_0(T_{\text{gate}})), \tag{5.10}$$

where we assume that $g = g_{j_k}$ is the same for all transitions. In this case the final state after a successful gate is

$$\hat{\rho}_{\text{gate}} = \frac{1}{p_{\text{gate}}}\hat{\rho}_0(T_{\text{gate}}). \tag{5.11}$$

Here assuming $\kappa = 2\pi \times 16$ MHz, for a quality factor of 1.2×10^7 and $C \simeq 9 \times 10^4$, a cavity with a length of $\sim 5\,\mu$m is required (for more information see Sec.5.6.1). In the bad-cavity regime where $g/\kappa = 10^{-1}$, perfect monitoring efficiency $p\eta_d = 1$ improves the maximum gate fidelity from 0.968 to 0.995 while also decreasing the optimal detuning from about 100κ to 20κ, corresponding to a decrease in optimal gate time from $T_{\text{gate}} = 160\mu$s to $T_{\text{gate}} = 32\mu$s (see figure 5.5). These improvements come at the cost of the scheme becoming non-deterministic with an efficiency of 0.86.

5.4.3 Electric dipole-dipole interaction

The achievable fidelity for this CNOT gate is [114]:

$$F_{\text{gate}} \simeq 1 - \frac{T_{\text{gate}}}{80}(42\gamma + 25\gamma^\star + 25\chi) - \frac{43\pi^2}{128}\left(\frac{\delta\nu}{\Delta\nu}\right)^2 \tag{5.12}$$

where $T_{\text{gate}} = 5\pi/\Omega = 5\pi\sqrt{3}/\Delta\nu$ is the gate time, Ω is the Rabi frequency for optical transitions (here we assumed $\Omega_\uparrow = \Omega_\downarrow = \Omega$), $\Delta\nu$ is the shift in the transition frequency, $\delta\nu$ is a potential mischaracterization from the true value of $\Delta\nu$, and χ is the spin decoherence rate of the ion. Eq. 5.12 is valid to first order in $\gamma, \gamma^\star, \chi \ll \Omega \propto \Delta\nu$ and second-order in $\delta\nu/\Delta\nu \ll 1$. Considering $\chi = 2\pi \times 0.12$ Hz (for B=7 T) [92], $\gamma = 2\pi \times 14$ Hz [25], $\gamma^\star = 2\pi \times 32$ Hz, $\Delta\nu = 250$ KHz (corresponding to $r = 5$ nm) and $\delta\nu/\Delta\nu = 0.02$ the fidelity

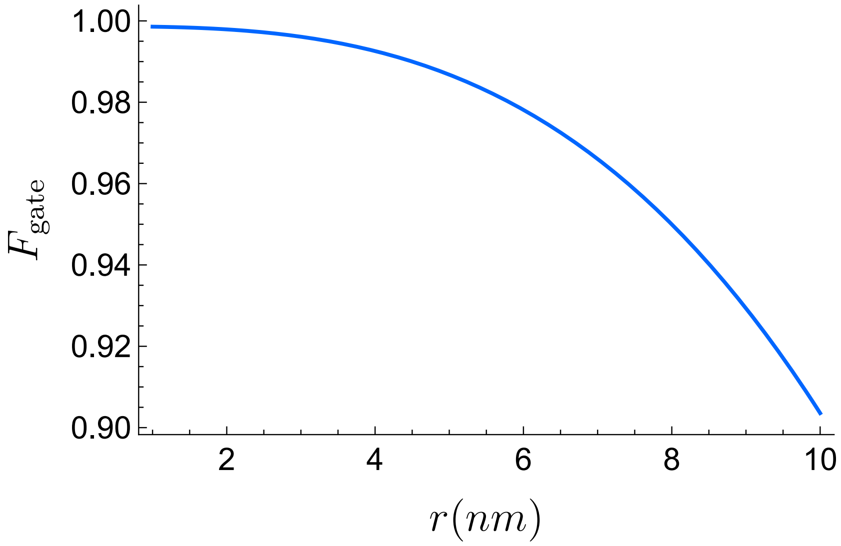

Figure 5.6: Fidelity of the electric dipole-dipole interaction gate as a function of the distance between ions. Here we assume $\delta\nu/(\Delta\nu) = 0.02$.

and gate time are $F_{\text{gate}} = 0.987$ and $T_{\text{gate}} = 108\,\mu\text{s}$, respectively. Fig. 5.6 shows the gate fidelity as a function of the separation between ions.

5.4.4 State readout

For state readout, we assume that the $|\uparrow\rangle$–$|e\rangle$ transition is resonant with the cavity while $|\downarrow\rangle$–$|e'\rangle$ is not. By exciting $|\uparrow\rangle$ with a sequence of π-pulses and monitoring emission as it decays back to $|\uparrow\rangle$, the intensity contrast can be used to distinguish $|\uparrow\rangle$ from $|\downarrow\rangle$ with high fidelity [106, 165].

Let B (D) denote the measurement result indicating $\uparrow$ ($\downarrow$). Then the fidelity is the conditional probability $P(\uparrow|B)$ ($P(\downarrow|D)$) of being in state $\uparrow$ ($\downarrow$) given the measurement outcome B (D). The total probability of success is $p_{\text{readout}} = P(B) + P(D)$ and we define the total fidelity as the weighted average of the conditional fidelity $F_{\text{readout}} = (P(B)P(\uparrow|B) + P(D)P(\downarrow|D))/p_{\text{readout}}$. If we assume that $P(\uparrow) = P(\downarrow) = 1/2$ and events B and D are complementary resulting in a deterministic scheme where $p_{\text{readout}} = 1$, then using Bayes' theorem: $P(i|j) = P(i)P(j|i)/P(j)$ where $i \in \{\uparrow, \downarrow\}$ and $j \in \{\text{B, D}\}$, we have $F_{\text{readout}} = (P(B|\uparrow) + P(D|\downarrow))/2$.

Suppose that the detector has a probability of $\xi \ll 1$ to detect a photon when the ion is in state $|\downarrow\rangle$ during a single cycle; for example, due to noise from excitation or dark counts. On the other hand, there is a chance $p\eta_d \gg \xi$ that a single cycle of $|\uparrow\rangle$–$|e\rangle$ results in a single-photon detection. A simple readout scheme is then to excite the ion a fixed number of N times and define event B to be the detection of one or more photons and event D as the complimentary (no photons). The state $|\downarrow\rangle$ results in D if no detection occurs and so $P(D|\downarrow) = (1-\xi)^N \simeq 1 - N\xi$. On the other hand, the probability to see at least one photon after N pulses is given by $P(B|\uparrow) = 1-(1-p\eta_d)^N$. Hence $F_{\text{readout}} = 1-N\xi/2-(1-p\eta_d)^N/2$.

For a fixed number of N pulses with a repetition period of T_p, the fixed readout time is $T_{\text{readout}} = NT_p$ when assuming that the measurement time after the last pulse is also T_p. To optimize this readout time, it is possible to increase the repetition rate. However, doing so risks coherently de-exciting the ion when $T_p \lesssim 1/\gamma'$, effectively reducing the probability of emitting a photon. Considering that the probability for decay between pulses separated by T_p is $1 - e^{-T_p\gamma'}$ we find that the probability for emission between the kth and $(k+1)$th pulse is $\eta_p(k) = (1-(-1)^k e^{-kT_p\gamma'})\tanh(T_p\gamma'/2)$. Then the fidelity becomes $F_{\text{readout}} \simeq 1 - N\xi/2 - (1/2)\prod_{k=1}^{N}[1 - p\eta_d\eta_p(k)]$. Using a cavity with $F_p = 5000$, the ion lifetime is $1/\gamma' \simeq 10.6\mu\text{s}$. Then for a readout time of $T_{\text{readout}} = 150\mu\text{s}$ using $N = 7$ pulses with $T_p = 21.4\mu\text{s}$, the fidelity can be as high as $F_{\text{readout}} = 0.9998$ for $p\eta_d = 0.9$ and $\xi = 10^{-5}$ (see Fig. 5.7).

5.4.5 End-to-end repeater fidelity

To estimate the fidelity of the final entangled state over the entire distance L, we multiply the fidelities of all the individual steps for a repeater protocol as follows

$$F_{\text{end-to-end}} = (F_{\text{init}})^{2m} \times (F_{\text{entangle}})^{m} \times (F_{\text{swap}})^{m-1}, \tag{5.13}$$

where m is the number of elementary links of length L_0. Note that Eq.5.13 is an estimation of the end-to-end fidelity that is only accurate at high fidelity regime. However, it still gives us a good approximation of the relative fidelity of the different cases. Here F_{swap}

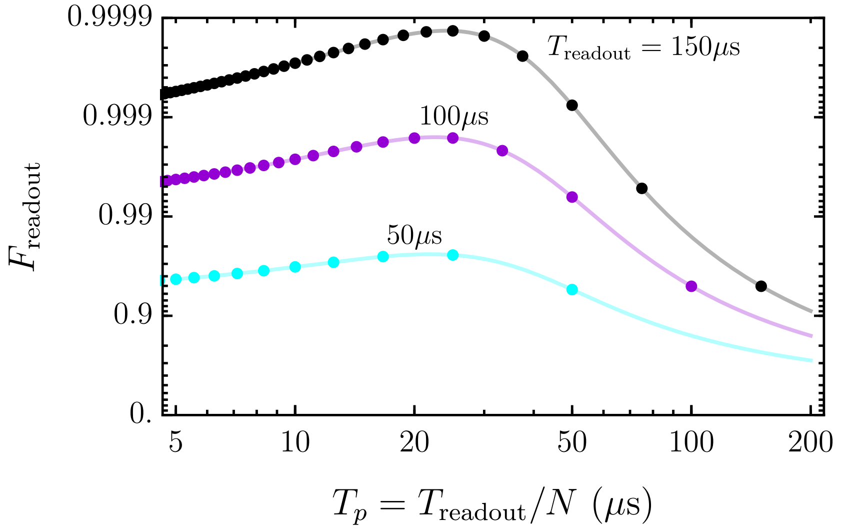

Figure 5.7: Readout fidelity F_{readout} as a function of pulse separation T_p for $p\eta_d = 0.9$, $\xi = 10^{-5}$, and a Purcell factor of $F_p = 5000$ corresponding to $1/\gamma' = 10.6\mu$s. The points show the valid discrete values associated with an integer number of total pulses N. The curves connecting the points are given by the continuous extension of F_{readout} to help guide the eye.

includes two spin read-out measurements; therefore, assuming dark counts are negligible, $F_{\text{swap}} = F_{\text{gate}} \times (F_{\text{readout}})^2$ where F_{gate} is the fidelity of performing the swapping gate for each scheme (i.e., Eqs. (5.4) and (5.12)). The fidelity of the entanglement generation needs to be established over m elementary links of length L_0. It has been shown that, even without the use of error correction protocols, the coherence time of 1 s is more than enough to distribute entanglement over the distance of $L = 1000$ km [173]. Hence, we neglect the effect of the finite coherence time of the quantum memory due to the long hyperfine coherence time of the ^{167}Er ion [92].

Fig. 5.8 shows the end-to-end fidelity estimation of the repeater protocol for different swapping schemes studied here as a function of the number of elementary links m for $F_p = 4.5 \times 10^5$ and $F_p = 5 \times 10^3$. As shown, the end-to-end fidelity of virtual photon exchange scheme increases significantly by monitoring the cavity emission to post-select successful gates. We have also shown the end-to-end fidelity of the scheme of Ref [114]. In this case the Eq. (5.13) changes to $F_{\text{end-to-end}} = (F_{\text{init}})^{3m+1} \times (F_{\text{entangle}})^m \times (F_{\text{swap}})^{m-1} \times (F_{\text{map}})^{m/2}$ where

$F_{\text{swap}} = F_{\text{map}} = (F_{\text{gate}} \times F_{\text{readout}})^2$ as each of these steps require performing two CNOT gates and two measurements (note that for the entanglement mapping, one needs to perform the gate and measurement at each end of the link) [114]. To further increase the fidelity of the repeater schemes, purification protocols could be used [174].

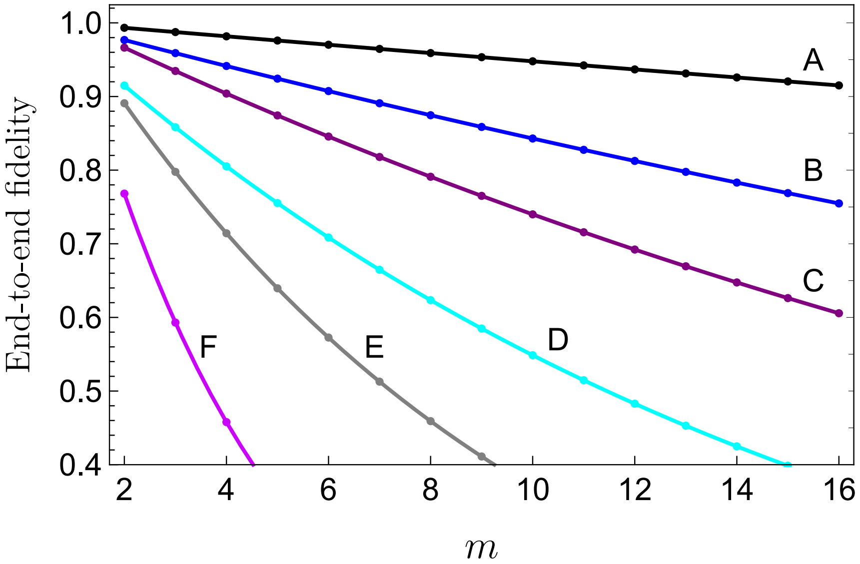

Figure 5.8: Estimation of the end-to-end fidelity of the repeater scheme with respect to the number of elementary links. Shown are the virtual photon exchange scheme post-selected on no cavity emission for $F_p = 4.5 \times 10^5$ (A), and $F_p = 5 \times 10^3$ (E), the virtual photon exchange scheme (without post-selection) for $F_p = 4.5 \times 10^5$ (C), and $F_p = 5 \times 10^3$ (F), the electric dipole-dipole interaction scheme for $F_p = 5 \times 10^3$ (B), and also the scheme of Ref [114] for $F_p = 5 \times 10^3$ (D). Here we assumed $p\eta_d = 0.9$, $N = 7$, $T_p = 2/\gamma'$, $\xi = 10^{-5}$, $\Delta_w = 0$ and $T_{\text{init}} = 8/\gamma'$. For europium (Eu) ions in ref [114], we also assumed $\gamma_{Eu} = 2\pi \times 80$ Hz, $\gamma^{\star}_{Eu} = 2\pi \times 19$ Hz and $\chi_{Eu} = 0$ [74, 40].

5.5 Entanglement generation rate

The average time to distribute entanglement over two elementary links of length L_0 is [18]

$$\langle T \rangle_{2L_0} = \left(\frac{3}{2}\right) \frac{L_0/c + T_{\text{init}}}{p_{en} p_s}, \tag{5.14}$$

where $c = 2 \times 10^8 \frac{\text{m}}{\text{s}}$, p_{en} is the success probability of entanglement generation over an elementary link (see Sec.5.4.1), and $p_s = p_{\text{gate}}$ is the success probability of the entanglement

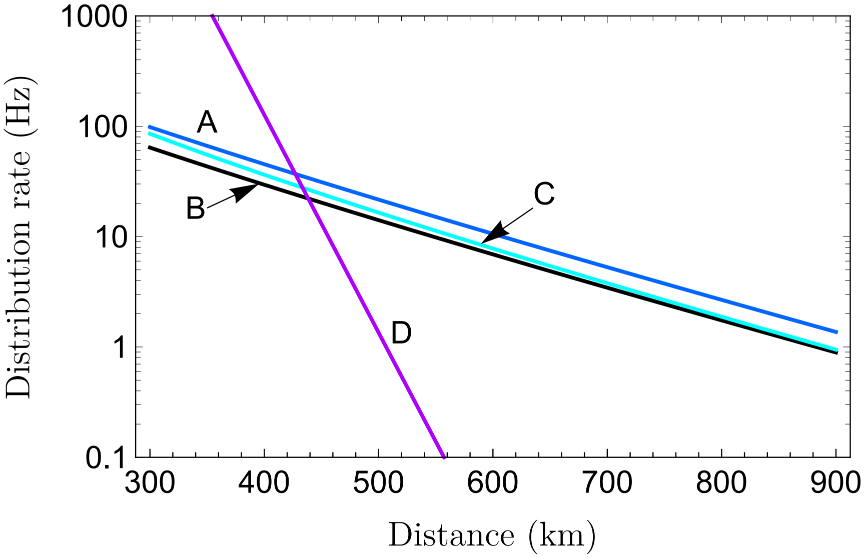

Figure 5.9: Comparison of the entanglement generation rate as a function of the distribution distance for single rare-earth ion-based repeater protocols. Our protocol for the deterministic entanglement swapping ($p_{\text{gate}} = 1$) (A) is compared with the the protocol of the Ref.[114] (B). Also shown is our protocol for the probabilistic swapping gate ($p_{\text{gate}} = 0.93$) (C), and finally the direct transmission in a fiber with a 1 GHz single-photon source (D). Here we assumed $m = 8$ and $T_{\text{init}} = 8/\gamma'$. For lines A and B we set $F_p = 5 \times 10^3$ and for line C we assumed $F_p = 4.5 \times 10^5$.

swapping. The entanglement generation time over the entire distance $L = mL_0$, where m is the number of links, is then given by [175]

$$\langle T \rangle_L = f(m)\frac{L_0/c + T_{\text{init}}}{p_{en}\, p_s^{m-1}}, \tag{5.15}$$

where $f(m) = 0.64\log_2(m) + 0.83$ is a good approximation of the average number of attempts to successfully generate entanglement (this factor reduces to 3/2 for the case of $m = 2$).

Here we assumed that the entanglement generation process could be performed on neighboring links at the same time. On the other hand, if entanglement generation should be established on neighboring links one by one (which is the case when spatial resolution of ions is not possible), then Eq. (5.15) changes to

$$\langle T \rangle_L = 2f(m/2)\frac{L_0/c + T_{\text{init}}}{p_{en}\, p_s^{m-1}}, \tag{5.16}$$

Note that here the swapping time (which includes the times required to perform the gate and read out the ions) is negligible compared to the time it takes to establish two neighboring links. As an example, even for the extreme case of $L = 300$ km and $m = 8$, the time needed to establish two neigboring links is 3.82 ms, which is quite large compare to the gate and readout times discussed in Sec.5.4. This waiting time increases significantly by increasing the length of the elementary links. For instance, when $L = 500$ km and $m = 8$, the waiting time would be 19.83 ms.

In Fig.5.9, using Eq.(5.15) we have plotted the entanglement generation rates of our proposed scheme as a function of distance for $m = 8$ and compared the result with the rates achieved using the single Er-Eu scheme [114]. Line A shows the rate of our protocol for deterministic gates with $p_{\text{gate}} = 1$ (i.e., virtual photon exchange without cavity monitoring or the electric dipole interaction), while B shows the rate for the protocol of Ref.[114]. Shown is also the repeater rates for the virtual photon exchange scheme post-selected on no cavity emission C. Here we put $p_{\text{gate}} = 0.93$ which corresponds to the $F_p = 4.5 \times 10^5$ and $p\eta_d = 0.9$, as shown in Fig.5.5. Note that, in terms of the efficiency, a high Purcell factor is not required for the other schemes. We have also plotted the rate expected using the direct transmission of photons with a 1 GHz photon rate (D) [176].

In the scheme of Ref. [114], the process of measuring the communication ion (^{168}Er), after mapping its state to the memory ion (^{151}Eu), introduced an additional source of inefficiency to the system. In our proposed scheme, however, the single ^{167}Er ions serve as both communication and memory ions; thus, the scaling with distance is better. By increasing the number of cycling transitions, the success probability of the measurement set improves, and the difference in rates between the two schemes becomes less drastic. However, even in this case, the implementation of the current proposed scheme is more experimentally feasible than the Er-Eu scheme because it does not require fabricating and identifying a close-lying pair of two species of ions.

5.6 Implementation

5.6.1 Entanglement generation

To perform entanglement generation between Er_i and Er_{i-1}, for example, as illustrated in Fig5.1.a, we need to selectively optically address one ion at a time. Therefore, we either need to spatially address ions of the same cavity or put Er_{i+1} and Er_{i-2} ions out of resonance with the cavities they are placed in. One option to achieve the latter is through applying an electric field gradient to each cavity-ion system [62]. The Stark shift will then change the optical transition frequency of the ion out of resonance with the cavity.

Then, we need to prepare each ion in the ground state $|\uparrow\rangle$. Using frequency selection, pumping of $95\pm3\%$ of the population into the $m_I = \frac{7}{2}$ hyperfine state has been demonstrated for an ensemble of Er ions [92]. For an individual Er in the presence of a high-Purcell-factor cavity, a much higher percentage is expected.

The entanglement generation step also requires the excitation of the $|\uparrow\rangle$–$|e\rangle$ transition for the ion which is resonant with the cavity. In order to avoid exciting both ground states to their respective excited states, the pulse spectral width should be much less than the difference between the ground and excited hyperfine level splittings. A cavity with a sufficiently small linewidth can also improve the branching ratio by enhancing one of the two transitions. For example, for the ground and excited states splitting difference of $\delta_{eg} \simeq 2\pi \times 100$ MHz [92], a cavity with a linewidth of κ (FWHM) centered on one transition can enhance that transition $\sim 1 + 4(\delta_{eg}/\kappa)^2$ times more than the transition detuned by δ_{eg}.

For rare-earth ions doped YSO photonic crystals cavities, quality factor of $27,000$ has been demonstrated [177]. Theoretical predictions, however, expect the quality factor as high as 10^5, which could be improved even further by, for example, post-fabrication annealing or using materials with higher refractive indexes [178, 177]. Besides, quality factor exceeding 1.1×10^7 has been measured in silicon photonic crystal nanocavities [179].

For Er ions doped into YSO crystal, Böttger et al [180] showed that the spectral diffusion decreases with increasing external magnetic field and decreasing temperature, and is undetectable at $B = 3$ T and $T = 1.6$ K even for a non-negligible Er concentration i.e., 0.0015% (see Fig.2.c of the Ref [180]). The spectral diffusion should be even lower under our conditions, where we only deal with individual Er ions at high fields and low temperatures. Hence, in this paper, we assume that the spectral diffusion is negligible compared to the Γ' (i.e., Purcell enhanced ZPL that dictates the entanglement generation fidelity), and Δ (i.e, ion-cavity detuning for swapping schemes). Note that, for the entanglement generation scheme, the Purcell effect further reduces the impact of spectral diffusion

5.6.2 Entanglement swapping

In the following, we discuss pros and cons for each entanglement swapping scheme in more detail.

Virtual photon exchange: Using this scheme, one can perform a deterministic gate between ions without the need of ions to be close-lying. During entanglement generation, the $|\uparrow\rangle$–$|e\rangle$ transition of an ion should be in resonance with the cavity. However, to perform the entanglement swapping using the virtual photon exchange scheme, the ions need to be dispersively coupled to the cavity. Therefore, one needs to detune the $|\uparrow\rangle$–$|e\rangle$ transitions away from resonance with the cavity before performing the entanglement swapping. An applied electric field amplitude E, could DC Stark shift the optical transition frequency of the ion by $\Delta = (\vec{\Delta\mu} \cdot \vec{E})\alpha/\hbar$ where $\alpha = (2+\epsilon)/3$ is the Lorentz correction factor [95]. It is also possible to detune the cavity rather than the ions by, for example, a piezoelectric effect [181].

It may be possible to avoid this detuning process between the entanglement generation step and the swapping step by making the cavity resonant with one transition (e.g., $|\uparrow\rangle$–$|e\rangle$) for entanglement generation and then choosing to use an off-resonant transition for the dissipative interaction required for entanglement swapping.

For the virtual exchange scheme, it is also necessary to tune the optical transitions of the ions into resonance with each other. In the case that we are able to address ions individually in space, this can be done by using, for example, the AC Stark effect. On the other hand, if individual addressing is not possible, we can use a large electric or magnetic field gradient to tune the transitions. The precision required for this resonance is determined by the gate time. Using equation (5.4) and the numerical values for fidelity and gate time given at the end of section 5.4.2 for $C = 9 \times 10^4$, we estimate that the transitions should be resonant to within $2\pi \times 0.8$ kHz for the deterministic scheme and within $2\pi \times 1.6$ kHz when using perfect cavity monitoring. Although any amount of ion-ion detuning can cause infidelity, transitions further separated than this value will cause infidelity greater than the infidelity caused only by the finite cavity cooperativity. Note that detuning between transitions can actually be many times larger than their linewidths. This is because the value of ion-ion detuning Δ_w required to overtake the cooperativity-limited infidelity of $2\pi/\sqrt{C}$ is proportional to $\gamma C^{1/4}$.

However, after tuning the ions, to excite only one of the Er ions to the excited state, we still require the spatial resolution. For Er ions, which have long spontaneous emission time compared to the gate time, it might be possible to obviate this requirement by exciting one ion before bringing them in resonance. In this case, we should bring ions into resonance much faster than the gate time to keep the process adiabatic.

Efficient post-selection can enhance the fidelity of the gate for a given cavity cooperativity (or equivalently, reduce the cavity cooperativity requirement for a given fidelity). This method is especially useful for RE ions, which typically couple to the cavity in the weak coupling regime. This is because the adiabatic condition needed to achieve a virtual photon interaction can be more easily violated for cavities near or within the strong coupling regime. Hence, in that regime, any gains in fidelity made by reducing the emitter-cavity detuning when post-selecting successful gates are offset by a decreased fidelity due to non-adiabatic phase evolution.

Electric dipole-dipole interaction: To perform this gate, it is necessary to use ion transitions that are far detuned from the cavity. Otherwise, the excited state may decay due to the off-resonant Purcell effect before the gate is complete. This is apparent from Eq.

(5.12) where $F_{\text{gate}} \sim 1 - T_{\text{gate}}\gamma/2$ implies that $\gamma \to \gamma + F_p\gamma_r$ would very quickly degrade the fidelity for a large Purcell factor F_p. If the cavity is resonant with $|\uparrow\rangle$–$|e\rangle$ for entanglement generation, then using the transition $|\uparrow\rangle$–$|e'\rangle$ for the dipole-dipole interaction may place the transition $|\downarrow\rangle$–$|e'\rangle$ close to the cavity resonance. Hence the difference between the Zeeman splitting of the ground and excited states δ_{eg} should be much larger than the cavity linewidth κ. Since $\delta_{eg} \simeq 2\pi \times 100$ MHz, this implies it is necessary for the cavity quality factor to be larger than about 10^7. For example, using $F_p = 5000$ and $\kappa = 2\pi \times 16$ MHz corresponding to $Q = 1.2 \times 10^7$, the gate fidelity reduces to 0.951 due to an off-resonant Purcell factor of 32.

Instead of requiring a far detuned transition, one could also actively detune the ions away from resonance with the cavity before performing the swapping gate using, for instance, the same methods mentioned for the virtual photon exchange scheme.

The electric dipole-dipole interaction performs a deterministic gate that is very sensitive to the distance between the ions and requires them to be very close together (see Fig.5.6). Hence, to perform the pulse sequence explained in Fig. 5.3, it is still necessary to have either spatial or spectral resolution of the ions.

The dipole moment difference for $^{168}\text{Er}^{3+}$:Y_2SiO_5 is approximately 0.84×10^{-31}Cm [114]. If we assume the same value for $^{167}\text{Er}^{3+}$:Y_2SiO_5, then this gives an estimate for $\Delta\nu$ of 30 and 0.03 MHz for $r_{ij} = 1$ and 10 nm, respectively. These values are quite large compared to the magnetic dipole-dipole interaction between the ions. For ^{167}Er with the magnetic moment of $-0.1618\ \mu_N$ [167], the magnetic dipole-dipole interaction is approximately 1.23 and 0.001 Hz for $r_{ij} = 1$ and 10 nm, respectively. As a result, the magnetic dipole-dipole interaction will not interfere with the electric dipole-dipole interaction.

Performing the CNOT gate using the electric dipole-dipole interaction does not require a cavity itself; however, to generate entanglement and to enhance the cycling transition (for the spin readout), the $|\uparrow\rangle$–$|e\rangle$ transition of the ions should be resonant with a cavity.

Unlike the virtual photon exchange scheme, the dipole-dipole scheme cannot take advantage of a high readout efficiency to improve fidelity by monitoring the cavity emission. This is because, in this scheme, the cavity does not mediate the interaction and so it is already necessary to minimize cavity emission by detuning it as far as possible. However, if a system can be optimized for a high collection efficiency of spontaneous emission directly from the Er ions without causing a Purcell enhancement, it may be possible to apply this same principle to the dipole-dipole gate. This type of collection enhancement could be implement using, for example, a combination of microfabricated solid-immersion lenses [24], reflective coatings on one side of the substrate, and an objective with a large numerical aperture.

5.6.3 State readout

In all of the explained schemes, a spin readout of each ion is required. To do so, we excite the $|\uparrow\rangle$–$|e\rangle$ transition of the Er ion and attempt to detect an emitted photon. The probability of emitting a photon into the cavity mode (emission quantum efficiency) is $p = \eta_c \gamma_r F_p/(\gamma_r F_p + \gamma)$. Hence, for example, for $F_p = 5000$ we expect $p = 0.999\eta_c \simeq \eta_c$. The overall collection efficiency for a cavity photon by itself depends on some other inefficiencies such as the cavity inefficiencies (e.g., fabrications imperfections, scattering loss and nonlinear absorption and dispersion) and waveguide-fibre coupling [22, 66, 182]. Even for $p = 1$, the state measurement is limited by the efficiency of the single-photon detectors. Using superconducting detectors, the detection efficiency of more than 90% has been demonstrated [104, 105, 141]. As shown in Sec. 5.4.4, to improve the detection probability, we can repeatedly excite the ion in a cycling transition (through the $|\uparrow\rangle$–$|e\rangle$ transition) such that many photons will be emitted into the cavity and eventually at least one will be detected [106, 165, 100]. Recently, it has been shown that a single ^{168}Er ion doped Y_2SiO_5 crystal coupled to a silicon nanophotonic cavity can scatter more than 1200 photons using a single cycling transition [165]. Thus the probability that the cycle terminates during the small number of pulses needed to achieve a high fidelity readout is negligible. This also implies that a high-fidelity readout is possible even if the collection and detection efficiency is low by increasing the number of readout pulses. The consequence is that the readout time increases and, if comparable to the time needed to establish entanglement over an elementary link, may impact the distribution rate.

5.7 conclusion and outlook

The ^{167}Er RE ion provides all of the desired features to implement the required elements of a quantum repeater. It has a nuclear spin coherence time within the one-second range, providing a natural long-lived quantum memory. It also has emission in the telecommunication wavelength window for low-loss long-distance transmission. Our proposed quantum repeater architecture utilizes a cavity-ion coupling to increase the spontaneous emission rate of the ion, improving the collection efficiency and single-photon indistinguishability. We discussed two different schemes to perform two qubit gates to achieve entanglement swapping within a repeater node. One can select the best scheme depending on the cavity characteristics and whether or not the ions are individually addressable in space or spectrum, or not at all. We have also shown how to improve the fidelity of a cavity-based virtual photon exchange entanglement swapping scheme by post-selecting successful gates on the absence of detected cavity emission. This post-selection approach could also be useful for other systems and gate schemes where cavity dissipation is the primary limitation for the fidelity.

We have shown that by using single ^{167}Er ions, a higher entanglement distribution rate is possible compared to a hybrid single ^{168}Er - ^{151}Eu repeater scheme [114]. This entanglement distribution rate can even be further improved by multiplexing the protocol [114]. In terms of experimental feasibility, it is also easier to deal with a single species of ions rather than a doubly doped crystal.

Under certain conditions, a modified version of the Barrett-Kok scheme [183] can be used to perform a nearly deterministic swapping gate between nearby ions of a cavity. This scheme does not require any individual addressing of ions or having them be close-lying. Instead, it needs ions to be in resonance with each other. In this modified scheme, the ions are detuned from the cavity and both are excited to the state $|e\rangle$ simultaneously. The detection of one photon then projects one ion onto the state $|\uparrow\rangle$, but does not reveal which ion decayed. This generates an entangled state $|e\uparrow\rangle + |\uparrow e\rangle$ between the ions. After the first photon detection, if both ion qubits are immediately flipped, and we wait for a second photon detection, the entangled state $|\psi^{+}\rangle$ is generated between the ions. Therefore, one can use this modified scheme to perform a CNOT gate between ions in the same cavity. Because the excited-state lifetime of Er is so long, it should be possible to perform the feedback (spin flipping) fast enough to perform a nearly deterministic gate.

Acknowledgments

FKA would like to thank P. Goldner, H. De Riedmatten, N. Lauk, S. Goswami, Y. Wu, J. Ji, S. Kumar and N. Sinclair for useful discussions. This work was supported by the Natural Sciences and Engineering Research Council of Canada (NSERC) through its Discovery Grant, Canadian Graduate Scholarships and CREATE programs, and by Alberta Innovates Technology Futures (AITF).

Chapter 6

Conclusion and outlook

Taking advantage of the laws of quantum physics, quantum communication is able to distribute quantum information over long distances, and maintain the security of data. Quantum repeaters, as building blocks of quantum communication, have therefore attracted considerable attention over the last two decades.

The main goal of this thesis was to contribute to the development of quantum communication by proposing new quantum repeater protocols. The specific focus was to develop single-emitter-based quantum repeaters that outperform ensemble-based approaches yet are experimentally feasible with the current technology. Therefore, with regards to the recent experiments with single rare-earth ions doped into crystals, we designed two repeater protocols. In the first scheme, we proposed a quantum repeater protocol based on single Erbium and Europium rare-earth ions that promises the deterministic establishment of high-fidelity entanglement over long distances at an improved rate over that of the direct transmission of photons [114]. This scheme utilizes emission within the low-loss telecommunications window. It also benefits from the long nuclear spin coherence lifetime of the Eu ion that provides the required time to perform entanglement swapping and distribute entanglement over long distances. We proposed to perform logic gates between nearby ions using permanent electric dipole-dipole interaction. Besides, we outlined a multiplexed version of the scheme that, using existing technology, promises to increase the entanglement distribution rate over a single-mode version of our scheme.

In our second repeater scheme, we used a single species of rare-earth ions, i.e., ^{167}Er rather than a doubly doped crystal [145]. This scheme is more experimentally convenient than the first scheme as it does not require fabricating and identifying a close-lying pair of ^{168}Er-^{151}Eu ions. We proposed two different schemes to perform the entanglement swapping. In the first scheme, the interaction is mediated by the exchange of virtual cavity photons. We have also shown that by monitoring and collecting the cavity emission, one can improve the fidelity of the virtual photon exchange scheme at the cost of some efficiency. In the second swapping scheme, the controlled interaction between ions is achieved by the electric dipole-dipole interaction (the same as the first repeater protocol). We estimated the overall fidelity and entanglement distribution rate of this repeater protocol and compared the result with the hybrid single ^{168}Er-^{151}Eu repeater scheme.

The second direction of this thesis was to develop cavity assisted interactions between quantum systems. The ability to perform two-qubit gates is an inevitable component of future quantum networks. In this regard, we focused on schemes that do not require the interaction between quantum systems and cavities to be in the strong coupling regime. This is especially crucial for quantum emitters unlikely to reach the strong coupling regime, such as rare-earth ions with small dipole moments. We proposed three different schemes to perform two-qubit controlled phase-flip gates [169]. In the first scheme, we performed the gate by scattering a single photon off of a cavity-qubit system. In the second scheme, we used a dissipative cavity coupling and the exchange of virtual cavity photons to perform the gate. For the third scheme, by virtual excitation of the cavity mode via a Raman coupling, we performed the controlled phase-flip gate between qubits with unequal optical transition frequencies. We calculated the fidelity of these gates and discussed the pros and cons of each scheme in detail. The use of our proposed two-qubit gates is not restricted to rare-earth ions doped into various crystals. Instead, a wider range of physical systems, including quantum dots and defects in diamond, could utilize our research results.

There are several directions for future studies in the area of quantum repeaters that require further theoretical and experimental efforts. One direction is to improve the performance of the current cavities. It is especially vital as better cavities could further enhance, for example, the quantum efficiency, the single-photon indistinguishability and the spontaneous emission rate of quantum emitters. Another direction is to extend the storage time of quantum memories as, in principle, the longer the storage time, the more transmission distance one can achieve. In addition, most approaches to quantum memories require low temperature. Hence, developing room temperature repeater schemes is of great interest. Besides all of these, one of the remaining challenges for ground-based repeaters, is to build a repeater that is actually better than the direct transition of photons.

Distances beyond 2000 km seem out of reach with fiber-based approaches, and this is where satellites might be a part of the answer. Motivated by the recent demonstration of different sorts of quantum communications with satellites, e.g., entanglement distribution over 1200 km [184], quantum teleportation between the ground and the satellite [185] and quantum key distribution between the satellite and the ground [186], many countries, including Canada, are now planning to launch quantum communication satellites. In principle, quantum repeaters, combined with quantum satellites, would allow for the distribution of quantum information between any two locations on the earth's surface [6]. Therefore it is very natural to put further efforts into the realization of global entanglement distribution using quantum repeaters and quantum satellites.

Bibliography

[1] Nicolas Gisin and Rob Thew. Quantum communication. *Nature photonics*, 1(3):165, 2007.

[2] Charles H Bennett, Gilles Brassard, Claude Crépeau, Richard Jozsa, Asher Peres, and William K Wootters. Teleporting an unknown quantum state via dual classical and einstein-podolsky-rosen channels. *Physical review letters*, 70(13):1895, 1993.

[3] Nicolas Gisin, Grégoire Ribordy, Wolfgang Tittel, and Hugo Zbinden. Quantum cryptography. *Reviews of modern physics*, 74(1):145, 2002.

[4] Daniel Gottesman, Thomas Jennewein, and Sarah Croke. Longer-baseline telescopes using quantum repeaters. *Physical review letters*, 109(7):070503, 2012.

[5] H Jeff Kimble. The quantum internet. *Nature*, 453(7198):1023–1030, 2008.

[6] Christoph Simon. Towards a global quantum network. *Nature Photonics*, 11(11):678–680, 2017.

[7] H-J Briegel, Wolfgang Dür, Juan I Cirac, and Peter Zoller. Quantum repeaters: the role of imperfect local operations in quantum communication. *Physical Review Letters*, 81(26):5932, 1998.

[8] Benjamin Schumacher. Quantum coding. *Physical Review A*, 51(4):2738, 1995.

[9] Michael A Nielsen and Isaac Chuang. Quantum computation and quantum information, 2002.

[10] Klaus Mattle, Harald Weinfurter, Paul G Kwiat, and Anton Zeilinger. Dense coding in experimental quantum communication. *Physical Review Letters*, 76(25):4656, 1996.

[11] N Lütkenhaus, J Calsamiglia, and K-A Suominen. Bell measurements for teleportation. *Physical Review A*, 59(5):3295, 1999.

[12] William K Wootters and Wojciech H Zurek. A single quantum cannot be cloned. *Nature*, 299(5886):802–803, 1982.

[13] Valerio Scarani, Sofyan Iblisdir, Nicolas Gisin, and Antonio Acin. Quantum cloning. *Reviews of Modern Physics*, 77(4):1225, 2005.

[14] Gian-Carlo Ghirardi, Alberto Rimini, and Tullio Weber. A general argument against superluminal transmission through the quantum mechanical measurement process. *Lettere al Nuovo Cimento (1971-1985)*, 27(10):293–298, 1980.

[15] Marek Zukowski, Anton Zeilinger, Michael A Horne, and Aarthur K Ekert. “event-ready-detectors”bell experiment via entanglement swapping. *Physical Review Letters*, 71:4287–4290, 1993.

[16] Ryo Namiki, Oleg Gittsovich, Saikat Guha, and Norbert Lütkenhaus. Gaussian-only regenerative stations cannot act as quantum repeaters. *Physical Review A*, 90(6):062316, 2014.

[17] Crispin Gardiner, Peter Zoller, and Peter Zoller. *Quantum noise: a handbook of Markovian and non-Markovian quantum stochastic methods with applications to quantum optics*. Springer Science & Business Media, 2004.

[18] Nicolas Sangouard, Christoph Simon, Hugues de Riedmatten, and Nicolas Gisin. Quantum repeaters based on atomic ensembles and linear optics. *Rev. Mod. Phys.*, 83:33–80, Mar 2011.

[19] L-M Duan, MD Lukin, J Ignacio Cirac, and Peter Zoller. Long-distance quantum communication with atomic ensembles and linear optics. *Nature*, 414(6862):413–418, 2001.

[20] Tobias Utikal, Emanuel Eichhammer, Lutz Petersen, Alois Renn, Stephan Götzinger, and Vahid Sandoghdar. Spectroscopic detection and state preparation of a single praseodymium ion in a crystal. *Nature communications*, 5(1):1–8, 2014.

[21] R Kolesov, K Xia, R Reuter, R Stöhr, A Zappe, J Meijer, PR Hemmer, and J Wrachtrup. Optical detection of a single rare-earth ion in a crystal. *Nature communications*, 3(1):1–7, 2012.

[22] Tian Zhong, Jonathan M Kindem, John G Bartholomew, Jake Rochman, Ioana Craiciu, Varun Verma, Sae Woo Nam, Francesco Marsili, Matthew D Shaw, Andrew D Beyer, et al. Optically addressing single rare-earth ions in a nanophotonic cavity. *arXiv preprint arXiv:1803.07520*, 2018.

[23] Chunming Yin, Milos Rancic, Gabriele G de Boo, Nikolas Stavrias, Jeffrey C McCallum, Matthew J Sellars, and Sven Rogge. Optical addressing of an individual erbium ion in silicon. *Nature*, 497(7447):91–94, 2013.

[24] Hannes Bernien, Bas Hensen, Wolfgang Pfaff, Gerwin Koolstra, MS Blok, Lucio Robledo, TH Taminiau, Matthew Markham, DJ Twitchen, Lilian Childress, et al. Heralded entanglement between solid-state qubits separated by three metres. *Nature*, 497(7447):86–90, 2013.

[25] Guokui Liu and Bernard Jacquier. *Spectroscopic properties of rare earths in optical materials*, volume 83. Springer Science & Business Media, 2006.

[26] Roger M Macfarlane. High-resolution laser spectroscopy of rare-earth doped insulators: a personal perspective. *Journal of luminescence*, 100(1-4):1–20, 2002.

[27] Y Sun, CW Thiel, RL Cone, RW Equall, and RL Hutcheson. Recent progress in developing new rare earth materials for hole burning and coherent transient applications. *Journal of luminescence*, 98(1-4):281–287, 2002.

[28] R Wo Equall, Yongchen Sun, RL Cone, and RM Macfarlane. Ultraslow optical dephasing in eu 3+: Y 2 sio 5. *Physical review letters*, 72(14):2179, 1994.

[29] Ryuzi Yano, Masaharu Mitsunaga, and Naoshi Uesugi. Ultralong optical dephasing time in eu 3+: Y 2 sio 5. *Optics letters*, 16(23):1884–1886, 1991.

[30] DR Taylor and JP Hessler. Photon echo decay in ruby: electric dipole interactions and instantaneous diffusion. *Physics Letters A*, 50(3):205–207, 1974.

[31] Jin Huang, JM Zhang, A Lezama, and TW Mossberg. Excess dephasing in photon-echo experiments arising from excitation-induced electronic level shifts. *Physical review letters*, 63(1):78, 1989.

[32] R Orbach. Spin-lattice relaxation in rare-earth salts. *Proceedings of the Royal Society of London. Series A. Mathematical and Physical Sciences*, 264(1319):458–484, 1961.

[33] Flurin Könz, Y Sun, CW Thiel, RL Cone, RW Equall, RL Hutcheson, and RM Macfarlane. Temperature and concentration dependence of optical dephasing, spectral-hole lifetime, and anisotropic absorption in eu 3+: Y 2 sio 5. *Physical Review B*, 68(8):085109, 2003.

[34] A Caprez, P Meyer, P Mikhail, and J Hulliger. New host-lattices for hyperfine optical hole burning: Materials of low nuclear spin moment. *Materials research bulletin*, 32(8):1045–1054, 1997.

[35] R. M. Macfarlane and R. M. Shelby. *Spectroscopy of Solids Containing Rare Earth Ions*. North Holland, Amsterdam, 1987.

[36] RM Macfarlane and RM Shelby. Magnetic field dependent optical dephasing in laf3: Er3+. *Optics Communications*, 42(5):346–350, 1982.

[37] William Esco Moerner and Gary C Bjorklund. *Persistent spectral hole-burning: science and applications*, volume 1. Springer, 1988.

[38] Andrej Tkalcec. Cavity qed with erbium doped crystals coupled to microwave resonators. Master's thesis, Karlsruhe Institute of Technology, 2013.

[39] Anatole Abragam and Brebis Bleaney. *Electron paramagnetic resonance of transition ions*. OUP Oxford, 2012.

[40] Manjin Zhong, Morgan P Hedges, Rose L Ahlefeldt, John G Bartholomew, Sarah E Beavan, Sven M Wittig, Jevon J Longdell, and Matthew J Sellars. Optically addressable nuclear spins in a solid with a six-hour coherence time. *Nature*, 517(7533):177–180, 2015.

[41] Thomas Jennewein and Brendon Higgins. The quantum space race. *Physics World*, 26(03):52, 2013.

[42] Peter Komar, Eric M Kessler, Michael Bishof, Liang Jiang, Anders S Sørensen, Jun Ye, and Mikhail D Lukin. A quantum network of clocks. *Nat. Phys.*, 10(8):582, 2014.

[43] Warren P Grice. Arbitrarily complete bell-state measurement using only linear optical elements. *Phys. Rev. A*, 84(4):042331, 2011.

[44] Stephen Wein, Khabat Heshami, Christopher A Fuchs, Hari Krovi, Zachary Dutton, Wolfgang Tittel, and Christoph Simon. Efficiency of an enhanced linear optical bell-state measurement scheme with realistic imperfections. *Phys. Rev. A*, 94(3):032332, 2016.

[45] Nicolas Sangouard, Romain Dubessy, and Christoph Simon. Quantum repeaters based on single trapped ions. *Phys. Rev. A*, 79:042340, Apr 2009.

[46] Stephan Ritter, Christian Nolleke, Carolin Hahn, Andreas Reiserer, Andreas Neuzner, Manuel Uphoff, Martin Mucke, Eden Figueroa, Joerg Bochmann, and Gerhard Rempe. An elementary quantum network of single atoms in optical cavities. *Nature*, 484(7393):195–200, 04 2012.

[47] Andreas Reiserer and Gerhard Rempe. Cavity-based quantum networks with single atoms and optical photons. *Rev. Mod. Phys.*, 87:1379–1418, Dec 2015.

[48] B. Hensen, H. Bernien, A. E. Dreau, A. Reiserer, N. Kalb, M. S. Blok, J. Ruitenberg, R. F. L. Vermeulen, R. N. Schouten, C. Abellan, W. Amaya, V. Pruneri, M. W. Mitchell, M. Markham, D. J. Twitchen, D. Elkouss, S. Wehner, T. H. Taminiau, and R. Hanson. Loophole-free bell inequality violation using electron spins separated by 1.3 kilometres. *Nature*, 526(7575):682–686, 10 2015.

[49] D. L. Moehring, P. Maunz, S. Olmschenk, K. C. Younge, D. N. Matsukevich, L. M. Duan, and C. Monroe. Entanglement of single-atom quantum bits at a distance. *Nature*, 449(7158):68–71, 09 2007.

[50] L. Slodička, G. Hétet, N. Röck, P. Schindler, M. Hennrich, and R. Blatt. Atom-atom entanglement by single-photon detection. *Phys. Rev. Lett.*, 110:083603, Feb 2013.

[51] Kevin J Morse, Rohan JS Abraham, Adam DeAbreu, Camille Bowness, Timothy S Richards, Helge Riemann, Nikolay V Abrosimov, Peter Becker, Hans-Joachim Pohl, Michael LW Thewalt, et al. A photonic platform for donor spin qubits in silicon. *Science advances*, 3(7):e1700930, 2017.

[52] Aymeric Delteil, Zhe Sun, W Gao, Emre Togan, Stefan Faelt, and Atac Imamoglu. Generation of heralded entanglement between distant hole spins. *Nat. Phys.*, 12(3):218–223, 2016.

[53] R. Stockill, M. J. Stanley, L. Huthmacher, E. Clarke, M. Hugues, A. J. Miller, C. Matthiesen, C. Le Gall, and M. Atatüre. Phase-tuned entangled state generation between distant spin qubits. *Phys. Rev. Lett.*, 119:010503, Jul 2017.

[54] Wolfgang Tittel, Mikael Afzelius, Thierry Chaneliere, Rufus L Cone, Stefan Kröll, Sergey A Moiseev, and Matthew Sellars. Photon-echo quantum memory in solid state systems. *Laser & Photonics Rev.*, 4(2):244–267, 2010.

[55] Félix Bussières, Nicolas Sangouard, Mikael Afzelius, Hugues de Riedmatten, Christoph Simon, and Wolfgang Tittel. Prospective applications of optical quantum memories. *J. Mod. Opt.*, 60(18):1519–1537, 2013.

[56] Shiwei Wu, Gang Han, Delia J Milliron, Shaul Aloni, Virginia Altoe, Dmitri V Talapin, Bruce E Cohen, and P James Schuck. Non-blinking and photostable upconverted luminescence from single lanthanide-doped nanocrystals. *Proc. Natl. Acad. Sci.*, 106(27):10917–10921, 2009.

[57] Y. Chu, N.P. de Leon, B.J. Shields, B. Hausmann, R. Evans, E. Togan, M. J. Burek, M. Markham, A. Stacey, A.S. Zibrov, A. Yacoby, D.J. Twitchen, M. Loncar, H. Park, P. Maletinsky, and M.D. Lukin. Coherent optical transitions in implanted nitrogen vacancy centers. *Nano Letters*, 14(4):1982–1986, 2014.

[58] Daniel Brunner, Brian D. Gerardot, Paul A. Dalgarno, Gunter Wüst, Khaled Karrai, Nick G. Stoltz, Pierre M. Petroff, and Richard J. Warburton. A coherent single-hole spin in a semiconductor. *Science*, 325(5936):70–72, 2009.

[59] R. G. Neuhauser, K. T. Shimizu, W. K. Woo, S. A. Empedocles, and M. G. Bawendi. Correlation between fluorescence intermittency and spectral diffusion in single semiconductor quantum dots. *Phys. Rev. Lett.*, 85:3301–3304, Oct 2000.

[60] Rogerio de Sousa and S. Das Sarma. Theory of nuclear-induced spectral diffusion: Spin decoherence of phosphorus donors in si and gaas quantum dots. *Phys. Rev. B*, 68:115322, Sep 2003.

[61] Kangwei Xia, Roman Kolesov, Ya Wang, Petr Siyushev, Rolf Reuter, Thomas Kornher, Nadezhda Kukharchyk, Andreas D Wieck, Bruno Villa, Sen Yang, et al. All-optical preparation of coherent dark states of a single rare earth ion spin in a crystal. *Physical review letters*, 115(9):093602, 2015.

[62] Björn Lauritzen, Jiří Minář, Hugues De Riedmatten, Mikael Afzelius, Nicolas Sangouard, Christoph Simon, and Nicolas Gisin. Telecommunication-wavelength solid-state memory at the single photon level. *Physical review letters*, 104(8):080502, 2010.

[63] Mikael Afzelius, Imam Usmani, Atia Amari, Björn Lauritzen, Andreas Walther, Christoph Simon, Nicolas Sangouard, Jiří Minář, Hugues De Riedmatten, Nicolas Gisin, et al. Demonstration of atomic frequency comb memory for light with spin-wave storage. *Phys. Rev. Lett.*, 104(4):040503, 2010.

[64] Georg Heinze, Christian Hubrich, and Thomas Halfmann. Stopped light and image storage by electromagnetically induced transparency up to the regime of one minute. *Phys. Rev. Lett.*, 111:033601, Jul 2013.

[65] Cyril Laplane, Pierre Jobez, Jean Etesse, Nicolas Gisin, and Mikael Afzelius. Multimode and long-lived quantum correlations between photons and spins in a crystal. *Phys. Rev. Lett.*, 118(21):210501, 2017.

[66] A. M. Dibos, M. Raha, C. M. Phenicie, and J. D. Thompson. Atomic source of single photons in the telecom band. *Phys. Rev. Lett.*, 120:243601, Jun 2018.

[67] Tian Zhong, Jonathan M. Kindem, John G. Bartholomew, Jake Rochman, Ioana Craiciu, Evan Miyazono, Marco Bettinelli, Enrico Cavalli, Varun Verma, Sae Woo

Nam, Francesco Marsili, Matthew D. Shaw, Andrew D. Beyer, and Andrei Faraon. Nanophotonic rare-earth quantum memory with optically controlled retrieval. *Science*, 357(6358):1392–1395, 2017.

[68] Holger P Specht, Christian Nölleke, Andreas Reiserer, Manuel Uphoff, Eden Figueroa, Stephan Ritter, and Gerhard Rempe. A single-atom quantum memory. *Nature*, 473(7346):190–193, 2011.

[69] Sen Yang, Ya Wang, DD Bhaktavatsala Rao, Thai Hien Tran, Ali S Momenzadeh, M Markham, DJ Twitchen, Ping Wang, Wen Yang, Rainer Stöhr, et al. High-fidelity transfer and storage of photon states in a single nuclear spin. *Nature Photonics*, 10(8):507–511, 2016.

[70] J. J. Longdell and M. J. Sellars. Experimental demonstration of quantum-state tomography and qubit-qubit interactions for rare-earth-metal-ion-based solid-state qubits. *Phys. Rev. A*, 69:032307, Mar 2004.

[71] J. J. Longdell, M. J. Sellars, and N. B. Manson. Demonstration of conditional quantum phase shift between ions in a solid. *Phys. Rev. Lett.*, 93:130503, Sep 2004.

[72] Andreas Reiserer, Norbert Kalb, Machiel S Blok, Koen JM van Bemmelen, Tim H Taminiau, Ronald Hanson, Daniel J Twitchen, and Matthew Markham. Robust quantum-network memory using decoherence-protected subspaces of nuclear spins. *Phys. Rev. X*, 6(2):021040, 2016.

[73] Sean D. Barrett and Pieter Kok. Efficient high-fidelity quantum computation using matter qubits and linear optics. *Phys. Rev. A*, 71:060310, Jun 2005.

[74] DL McAuslan, Jevon Joseph Longdell, and MJ Sellars. Strong-coupling cavity qed using rare-earth-metal-ion dopants in monolithic resonators: What you can do with a weak oscillator. *Phys. Rev. A*, 80(6):062307, 2009.

[75] Nicklas Ohlsson, R Krishna Mohan, and Stefan Kröll. Quantum computer hardware based on rare-earth-ion-doped inorganic crystals. *Opt. Commun.*, 201(1):71–77, 2002.

[76] SB Altner, G Zumofen, UP Wild, and M Mitsunaga. Photon-echo attenuation in rare-earth-ion-doped crystals. *Phys. Rev. B*, 54(24):17493, 1996.

[77] Christoph Simon, Hugues de Riedmatten, Mikael Afzelius, Nicolas Sangouard, Hugo Zbinden, and Nicolas Gisin. Quantum repeaters with photon pair sources and multimode memories. *Phys. Rev. Lett.*, 98:190503, May 2007.

[78] O. A. Collins, S. D. Jenkins, A. Kuzmich, and T. A. B. Kennedy. Multiplexed memory-insensitive quantum repeaters. *Phys. Rev. Lett.*, 98:060502, Feb 2007.

[79] Neil Sinclair, Erhan Saglamyurek, Hassan Mallahzadeh, Joshua A. Slater, Mathew George, Raimund Ricken, Morgan P. Hedges, Daniel Oblak, Christoph Simon, Wolfgang Sohler, and Wolfgang Tittel. Spectral multiplexing for scalable quantum photonics using an atomic frequency comb quantum memory and feed-forward control. *Phys. Rev. Lett.*, 113:053603, Jul 2014.

[80] Stefano Pirandola, Riccardo Laurenza, Carlo Ottaviani, and Leonardo Banchi. Fundamental limits of repeaterless quantum communications. *Nat. Commun.*, 8, 2017.

[81] Tian Zhong, Jonathan M Kindem, Evan Miyazono, and Andrei Faraon. Nanophotonic coherent light–matter interfaces based on rare-earth-doped crystals. *Nature communications*, 6(1):1–6, 2015.

[82] C. W. Thiel, W. R. Babbitt, and R. L. Cone. Optical decoherence studies of yttrium oxyorthosilicate y_2sio_5 codoped with er^{3+} and eu^{3+} for optical signal processing and quantum information applications at 1.5 microns. *Phys. Rev. B*, 85:174302, May 2012.

[83] T. Kornher, K Xia, R Kolesov, N Kukharchyk, R Reuter, P Siyushev, R Stöhr, M Schreck, H. W. Becker, B Villa, Andrew D. Wieck, and J Wrachtrup. Produc-

tion yield of rare-earth ions implanted into an optical crystal. *Appl. Phys. Lett.*, 108(5):053108, 2016.

[84] Marcelo Davanco, Jin Liu, Luca Sapienza, Chen-Zhao Zhang, José Vinícius De Miranda Cardoso, Varun Verma, Richard Mirin, Sae Woo Nam, Liu Liu, and Kartik Srinivasan. Heterogeneous integration for on-chip quantum photonic circuits with single quantum dot devices. *Nat. Commun.*, 8(1):889, 2017.

[85] E. Murray, D. J. P. Ellis, T. Meany, F. F. Floether, J. P. Lee, J. P. Griffiths, G. A. C. Jones, I. Farrer, D. A. Ritchie, A. J. Bennett, and A. J. Shields. Quantum photonics hybrid integration platform. *Appl. Phys. Lett.*, 107(17):171108, 2015.

[86] Je-Hyung Kim, Shahriar Aghaeimeibodi, Christopher J. K. Richardson, Richard P. Leavitt, Dirk Englund, and Edo Waks. Hybrid integration of solid-state quantum emitters on a silicon photonic chip. *Nano Letters*, 17(12):7394–7400, 2017.

[87] S. R. Hastings-Simon, B. Lauritzen, M. U. Staudt, J. L. M. van Mechelen, C. Simon, H. de Riedmatten, M. Afzelius, and N. Gisin. Zeeman-level lifetimes in $\mathrm{er}^{3+}:\mathrm{y}_2\mathrm{sio}_5$. *Phys. Rev. B*, 78:085410, Aug 2008.

[88] Thomas Böttger, C. W. Thiel, Y. Sun, and R. L. Cone. Optical decoherence and spectral diffusion at 1.5 μm in $\mathrm{er}^{3+}:\mathrm{y}_2\mathrm{sio}_5$ versus magnetic field, temperature, and er^{3+} concentration. *Phys. Rev. B*, 73:075101, Feb 2006.

[89] S. Probst, H. Rotzinger, A. V. Ustinov, and P. A. Bushev. Microwave multimode memory with an erbium spin ensemble. *Phys. Rev. B*, 92:014421, Jul 2015.

[90] O. Guillot-Noël, H. Vezin, Ph. Goldner, F. Beaudoux, J. Vincent, J. Lejay, and I. Lorgeré. Direct observation of rare-earth-host interactions in $\mathrm{Er}:\mathrm{y}_2\mathrm{Sio}_5$. *Phys. Rev. B*, 76:180408, Nov 2007.

[91] Elliott Fraval, M J Sellars, A Morrison, and A Ferris. Pr–y interaction in pr3+: Y2sio5. *J. Lumin.*, 107(1-4):347–350, 2004.

[92] Miloš Rančić, Morgan P Hedges, Rose L Ahlefeldt, and Matthew J Sellars. Coherence time of over a second in a telecom-compatible quantum memory storage material. *Nature Physics*, 14(1):50, 2018.

[93] P Siyushev, K Xia, R Reuter, M Jamali, N Zhao, N Yang, C Duan, N Kukharchyk, AD Wieck, R Kolesov, et al. Coherent properties of single rare-earth spin qubits. *Nat. Commun.*, 5, 2014.

[94] B. Lauritzen, S. R. Hastings-Simon, H. de Riedmatten, M. Afzelius, and N. Gisin. State preparation by optical pumping in erbium-doped solids using stimulated emission and spin mixing. *Phys. Rev. A*, 78:043402, Oct 2008.

[95] Jiří Minář, Björn Lauritzen, Hugues de Riedmatten, Mikael Afzelius, Christoph Simon, and Nicolas Gisin. Electric control of collective atomic coherence in an erbium-doped solid. *New Journal of Physics*, 11(11):113019, 2009.

[96] Roger M. Macfarlane. Optical stark spectroscopy of solids. *J. Lumin.*, 125(1):156 – 174, 2007. Festschrift in Honor of Academician Alexander A. Kaplyanskii.

[97] Janus H. Wesenberg, Klaus Mølmer, Lars Rippe, and Stefan Kröll. Scalable designs for quantum computing with rare-earth-ion-doped crystals. *Phys. Rev. A*, 75:012304, Jan 2007.

[98] Yongchen Sun, Thomas Böttger, C. W. Thiel, and R. L. Cone. Magnetic g tensors for the $^4\mathrm{I}_{152}$ and $^4\mathrm{I}_{132}$ states of er^{3+}:y$_2$sio$_5$. *Phys. Rev. B*, 77:085124, Feb 2008.

[99] F. M. Pichanick, P. G. H. Sandars, and G. K. Woodgate. The nuclear magnetic dipole moments of the stable isotopes of europium and the hyperfine structure anomaly. *Proc. Royal Soc. A*, 257(1289):277–282, 1960.

[100] Chris O'Brien, Tian Zhong, Andrei Faraon, and Christoph Simon. Nondestructive photon detection using a single rare-earth ion coupled to a photonic cavity. *Phys. Rev. A*, 94:043807, Oct 2016.

[101] Thomas Grange, Gaston Hornecker, David Hunger, Jean-Philippe Poizat, Jean-Michel Gérard, Pascale Senellart, and Alexia Auffèves. Cavity-funneled generation of indistinguishable single photons from strongly dissipative quantum emitters. *Physical review letters*, 114(19):193601, 2015.

[102] Thomas Böttger, CW Thiel, RL Cone, and Y Sun. Effects of magnetic field orientation on optical decoherence in er 3+: Y 2 sio 5. *Physical Review B*, 79(11):115104, 2009.

[103] Chong-Ki Hong, Zhe-Yu Ou, and Leonard Mandel. Measurement of subpicosecond time intervals between two photons by interference. *Physical review letters*, 59(18):2044, 1987.

[104] Adriana E Lita, Aaron J Miller, and Sae Woo Nam. Counting near-infrared single-photons with 95% efficiency. *Opt. Express*, 16(5):3032–3040, 2008.

[105] F Marsili, Varun B Verma, Jeffrey A Stern, S Harrington, Adriana E Lita, Thomas Gerrits, Igor Vayshenker, Burm Baek, Matthew D Shaw, Richard P Mirin, et al. Detecting single infrared photons with 93% system efficiency. *Nat. Photonics*, 7(3):210–214, 2013.

[106] John G Bartholomew, Rose L Ahlefeldt, and Matthew J Sellars. Engineering closed optical transitions in rare-earth ion crystals. *Phys. Rev. B*, 93(1):014401, 2016.

[107] M. Grimau Puigibert, G. H. Aguilar, Q. Zhou, F. Marsili, M. D. Shaw, V. B. Verma, S. W. Nam, D. Oblak, and W. Tittel. Heralded single photons based on spectral multiplexing and feed-forward control. *Phys. Rev. Lett.*, 119:083601, Aug 2017.

[108] Ki Youl Yang, Dong Yoon Oh, Seung Hoon Lee, Qi-Fan Yang, Xu Yi, Boqiang Shen, Heming Wang, and Kerry Vahala. Bridging ultrahigh-q devices and photonic circuits. *Nat. Photonics*, 12(5):297–302, 2018.

[109] Christoph Simon, Hugues De Riedmatten, Mikael Afzelius, Nicolas Sangouard, Hugo Zbinden, and Nicolas Gisin. Quantum repeaters with photon pair sources and multimode memories. *Physical review letters*, 98(19):190503, 2007.

[110] B. Car, L. Veissier, A. Louchet-Chauvet, J.-L. Le Gouët, and T. Chanelière. Selective optical addressing of nuclear spins through superhyperfine interaction in rare-earth doped solids. *Phys. Rev. Lett.*, 120:197401, May 2018.

[111] Stephanie Wehner, David Elkouss, and Ronald Hanson. Quantum internet: A vision for the road ahead. *Science*, 362(6412):eaam9288, 2018.

[112] David Elieser Deutsch. Quantum computational networks. *Proceedings of the Royal Society of London. A. Mathematical and Physical Sciences*, 425(1868):73–90, 1989.

[113] L You and MS Chapman. Quantum entanglement using trapped atomic spins. *Physical Review A*, 62(5):052302, 2000.

[114] F Kimiaee Asadi, N Lauk, S Wein, N Sinclair, C O'Brien, and C Simon. Quantum repeaters with individual rare-earth ions at telecommunication wavelengths. *Quantum*, 2:93, 2018.

[115] M-A Lemonde, S Meesala, A Sipahigil, MJA Schuetz, MD Lukin, M Loncar, and P Rabl. Phonon networks with siv centers in diamond waveguides. *arXiv preprint arXiv:1801.01904*, 2018.

[116] L-M Duan, B Wang, and HJ Kimble. Robust quantum gates on neutral atoms with cavity-assisted photon scattering. *Physical Review A*, 72(3):032333, 2005.

[117] Ruffin E Evans, Mihir K Bhaskar, Denis D Sukachev, Christian T Nguyen, Alp Sipahigil, Michael J Burek, Bartholomeus Machielse, Grace H Zhang, Alexander S Zibrov, Edward Bielejec, et al. Photon-mediated interactions between quantum emitters in a diamond nanocavity. *Science*, 362(6415):662–665, 2018.

[118] Mang Feng. Quantum computing with trapped ions in an optical cavity via raman transition. *Physical Review A*, 66(5):054303, 2002.

[119] J Majer, JM Chow, JM Gambetta, Jens Koch, BR Johnson, JA Schreier, L Frunzio, DI Schuster, AA Houck, Andreas Wallraff, et al. Coupling superconducting qubits via a cavity bus. *Nature*, 449(7161):443, 2007.

[120] Mika A Sillanpää, Jae I Park, and Raymond W Simmonds. Coherent quantum state storage and transfer between two phase qubits via a resonant cavity. *Nature*, 449(7161):438, 2007.

[121] M Suhail Zubairy, Moochan Kim, and Marlan O Scully. Cavity-qed-based quantum phase gate. *Physical Review A*, 68(3):033820, 2003.

[122] Asoka Biswas and Girish Saran Agarwal. Quantum logic gates using stark-shifted raman transitions in a cavity. *Physical Review A*, 69(6):062306, 2004.

[123] J Pelal Reithmaier, G Sek, A Löffler, C Hofmann, S Kuhn, S Reitzenstein, LV Keldysh, VD Kulakovskii, TL Reinecke, and A Forchel. Strong coupling in a single quantum dot–semiconductor microcavity system. *Nature*, 432(7014):197, 2004.

[124] Emmanuelle Peter, Pascale Senellart, David Martrou, Aristide Lemaître, J Hours, JM Gérard, and Jacqueline Bloch. Exciton-photon strong-coupling regime for a single quantum dot embedded in a microcavity. *Physical review letters*, 95(6):067401, 2005.

[125] Dirk Englund, Andrei Faraon, Ilya Fushman, Nick Stoltz, Pierre Petroff, and Jelena Vučković. Controlling cavity reflectivity with a single quantum dot. *Nature*, 450(7171):857, 2007.

[126] Andreas Wallraff, David I Schuster, Alexandre Blais, Luigi Frunzio, R-S Huang, Johannes Majer, Sameer Kumar, Steven M Girvin, and Robert J Schoelkopf. Strong coupling of a single photon to a superconducting qubit using circuit quantum electrodynamics. *Nature*, 431(7005):162, 2004.

[127] DL McAuslan, D Korystov, and JJ Longdell. Coherent spectroscopy of rare-earth-metal-ion-doped whispering-gallery-mode resonators. *Physical Review A*, 83(6):063847, 2011.

[128] Stephan Welte, Bastian Hacker, Severin Daiss, Stephan Ritter, and Gerhard Rempe. Photon-mediated quantum gate between two neutral atoms in an optical cavity. *Physical Review X*, 8(1):011018, 2018.

[129] Alexandre Blais, Ren-Shou Huang, Andreas Wallraff, Steven M Girvin, and R Jun Schoelkopf. Cavity quantum electrodynamics for superconducting electrical circuits: An architecture for quantum computation. *Physical Review A*, 69(6):062320, 2004.

[130] L-M Duan and HJ Kimble. Scalable photonic quantum computation through cavity-assisted interactions. *Physical review letters*, 92(12):127902, 2004.

[131] Xiu-Min Lin, Zheng-Wei Zhou, Ming-Yong Ye, Yun-Feng Xiao, and Guang-Can Guo. One-step implementation of a multiqubit controlled-phase-flip gate. *Physical Review A*, 73(1):012323, 2006.

[132] Halyne S Borges, Daniel Z Rossatto, Fabrício S Luiz, and Celso J Villas-Boas. Heralded entangling quantum gate via cavity-assisted photon scattering. *Physical Review A*, 97(1):013828, 2018.

[133] Stephen Wein, Nikolai Lauk, Roohollah Ghobadi, and Christoph Simon. Feasibility of efficient room-temperature solid-state sources of indistinguishable single photons using ultrasmall mode volume cavities. *Physical Review B*, 97(1):205418, 2018.

[134] Alexandre Blais, Jay Gambetta, Andreas Wallraff, David I Schuster, Steven M Girvin, Michel H Devoret, and Robert J Schoelkopf. Quantum-information processing with circuit quantum electrodynamics. *Physical Review A*, 75(3):032329, 2007.

[135] A Imamoglu, David D Awschalom, Guido Burkard, David P DiVincenzo, Daniel Loss, M Sherwin, A Small, et al. Quantum information processing using quantum dot spins and cavity qed. *Physical review letters*, 83(20):4204, 1999.

[136] Feng Liu, Alistair J Brash, John O'Hara, Luis MPP Martins, Catherine L Phillips, Rikki J Coles, Benjamin Royall, Edmund Clarke, Christopher Bentham, Nikola Prtljaga, et al. High purcell factor generation of indistinguishable on-chip single photons. *Nature nanotechnology*, 13(9):835, 2018.

[137] Niccolo Somaschi, Valerian Giesz, Lorenzo De Santis, JC Loredo, Marcelo P Almeida, Gaston Hornecker, Simone Luca Portalupi, Thomas Grange, Carlos Antón, Justin Demory, et al. Near-optimal single-photon sources in the solid state. *Nature Photonics*, 10(5):340, 2016.

[138] Xing Ding, Yu He, Z-C Duan, Niels Gregersen, M-C Chen, S Unsleber, Sebastian Maier, Christian Schneider, Martin Kamp, Sven Höfling, et al. On-demand single photons with high extraction efficiency and near-unity indistinguishability from a resonantly driven quantum dot in a micropillar. *Physical review letters*, 116(2):020401, 2016.

[139] Hélène Ollivier, Ilse Maillette de Buy Wenniger, Sarah Thomas, Stephen Wein, Guillaume Coppola, Abdelmounaim Harouri, Paul Hilaire, Clément Millet, Aristide Lemaître, Isabelle Sagnes, Olivier Krebs, Loïc Lanco, Juan Carlos Loredo, Carlos

Antón, Niccolo Somaschi, and Pascale Senellart. Reproducibility of high-performance quantum dot single-photon sources. *arXiv preprint arXiv:1910.08863*, 2019.

[140] Hui Wang, Yu-Ming He, T-H Chung, Hai Hu, Ying Yu, Si Chen, Xing Ding, M-C Chen, Jian Qin, Xiaoxia Yang, et al. Towards optimal single-photon sources from polarized microcavities. *Nature Photonics*, pages 1–6, 2019.

[141] Mohsen K Akhlaghi, Ellen Schelew, and Jeff F Young. Waveguide integrated superconducting single-photon detectors implemented as near-perfect absorbers of coherent radiation. *Nature communications*, 6:8233, 2015.

[142] Mark G Thompson. Large-scale integrated quantum photonic technologies for communications and computation. In *Optical Fiber Communication Conference*, pages W3D–3. Optical Society of America, 2019.

[143] Svetlana Khasminskaya, Felix Pyatkov, Karolina Słowik, Simone Ferrari, Oliver Kahl, Vadim Kovalyuk, Patrik Rath, Andreas Vetter, Frank Hennrich, Manfred M Kappes, et al. Fully integrated quantum photonic circuit with an electrically driven light source. *Nature Photonics*, 10(11):727, 2016.

[144] Carl Bradac, Weibo Gao, Jacopo Forneris, Matt Trusheim, and Igor Aharonovich. Quantum nanophotonics with group iv defects in diamond. *arXiv preprint arXiv:1906:10992*, 2019.

[145] F Kimiaee Asadi, S C Wein, and C Simon. Protocols for long-distance quantum communication with single 167er ions. *Quantum Science and Technology*, 5(4):045015, sep 2020.

[146] Brendon C Rose, Ding Huang, Zi-Huai Zhang, Paul Stevenson, Alexei M Tyryshkin, Sorawis Sangtawesin, Srikanth Srinivasan, Lorne Loudin, Matthew L Markham, Andrew M Edmonds, et al. Observation of an environmentally insensitive solid-state spin defect in diamond. *Science*, 361(6397):60–63, 2018.

[147] XX Yi, XH Su, and L You. Conditional quantum phase gate between two 3-state atoms. *Physical review letters*, 90(9):097902, 2003.

[148] Jonathan M Kindem, John G Bartholomew, Philip JT Woodburn, Tian Zhong, Ioana Craiciu, Rufus L Cone, Charles W Thiel, and Andrei Faraon. Characterization of yb 3+ 171: Yvo 4 for photonic quantum technologies. *Physical Review B*, 98(2):024404, 2018.

[149] Jonathan M Kindem, Andrei Ruskuc, John G Bartholomew, Jake Rochman, Yan Qi Huan, and Andrei Faraon. Control and single-shot readout of an ion embedded in a nanophotonic cavity. *Nature*, 580(7802):201–204, 2020.

[150] Baidyanath Misra and EC George Sudarshan. The zeno's paradox in quantum theory. *Journal of Mathematical Physics*, 18(4):756–763, 1977.

[151] Jiannis Pachos and Herbert Walther. Quantum computation with trapped ions in an optical cavity. *Physical review letters*, 89(18):187903, 2002.

[152] Andrew J Daley. Quantum trajectories and open many-body quantum systems. *Advances in Physics*, 63(2):77–149, 2014.

[153] CY Hu, A Young, JL O'Brien, WJ Munro, and JsG Rarity. Giant optical faraday rotation induced by a single-electron spin in a quantum dot: applications to entangling remote spins via a single photon. *Physical Review B*, 78(8):085307, 2008.

[154] Daniel F Walls and Gerard J Milburn. *Quantum optics*. Springer Science & Business Media, 2007.

[155] L Childress, JM Taylor, Anders Søndberg Sørensen, and Mikhail D Lukin. Fault-tolerant quantum repeaters with minimal physical resources and implementations based on single-photon emitters. *Physical Review A*, 72(5):052330, 2005.

[156] Siddhartha Santra, Sreraman Muralidharan, Martin Lichtman, Liang Jiang, Christopher Monroe, and Vladimir S Malinovsky. Quantum repeaters based on two species trapped ions. *New Journal of Physics*, 21(7):073002, 2019.

[157] Filip Rozpedek, Raja Yehia, Kenneth Goodenough, Maximilian Ruf, Peter C Humphreys, Ronald Hanson, Stephanie Wehner, and David Elkouss. Near-term quantum-repeater experiments with nitrogen-vacancy centers: Overcoming the limitations of direct transmission. *Physical Review A*, 99(5):052330, 2019.

[158] Sourabh Kumar, Nikolai Lauk, and Christoph Simon. Towards long-distance quantum networks with superconducting processors and optical links. *Quantum Science and Technology*, 4(4):045003, 2019.

[159] Rikizo Ikuta, Toshiki Kobayashi, Shuto Yasui, Shigehito Miki, Taro Yamashita, Hirotaka Terai, Mikio Fujiwara, Takashi Yamamoto, Masato Koashi, Masahide Sasaki, et al. Frequency down-conversion of 637 nm light to the telecommunication band for non-classical light emitted from nv centers in diamond. *Optics express*, 22(9):11205–11214, 2014.

[160] Kristiaan De Greve, Leo Yu, Peter L McMahon, Jason S Pelc, Chandra M Natarajan, Na Young Kim, Eisuke Abe, Sebastian Maier, Christian Schneider, Martin Kamp, et al. Quantum-dot spin–photon entanglement via frequency downconversion to telecom wavelength. *Nature*, 491(7424):421–425, 2012.

[161] Kazuya Takemoto, Yoshiki Sakuma, Shinichi Hirose, Tatsuya Usuki, Naoki Yokoyama, Toshiyuki Miyazawa, Motomu Takatsu, and Yasuhiko Arakawa. Non-classical photon emission from a single inas/inp quantum dot in the 1.3-μm optical-fiber band. *Japanese journal of applied physics*, 43(7B):L993, 2004.

[162] L Bergeron, C Chartrand, ATK Kurkjian, KJ Morse, H Riemann, NV Abrosimov, P Becker, H-J Pohl, MLW Thewalt, and S Simmons. Characterization of the t center in ^{28}si. *arXiv preprint arXiv:2006.08794*, 2020.

[163] W Redjem, A Durand, T Herzig, A Benali, S Pezzagna, J Meijer, A Yu Kuznetsov, HS Nguyen, S Cueff, J-M Gérard, et al. Single artificial atoms in silicon emitting at telecom wavelengths. *arXiv preprint arXiv:2001.02136*, 2020.

[164] Bernardo Casabone, Chetan Deshmukh, Shuping Liu, Diana Serrano, Alban Ferrier, Thomas Hümmer, Philippe Goldner, David Hunger, and Hugues de Riedmatten. Dynamic control of purcell enhanced emission of erbium ions in nanoparticles. *arXiv preprint arXiv:2001.08532*, 2020.

[165] Mouktik Raha, Songtao Chen, Christopher M Phenicie, Salim Ourari, Alan M Dibos, and Jeff D Thompson. Optical quantum nondemolition measurement of a single rare earth ion qubit. *Nature Communications*, 11(1):1–6, 2020.

[166] CW Thiel, Thomas Böttger, and RL Cone. Rare-earth-doped materials for applications in quantum information storage and signal processing. *Journal of luminescence*, 131(3):353–361, 2011.

[167] DL McAuslan, JG Bartholomew, MJ Sellars, and JJ Longdell. Reducing decoherence in optical and spin transitions in rare-earth-ion doped materials. *arXiv preprint arXiv:1201.4610*, 2012.

[168] Stephen C Wein, Jia-Wei Ji, Yu-Feng Wu, Faezeh Kimiaee Asadi, Roohollah Ghobadi, and Christoph Simon. Analyzing photon-count heralded entanglement generation between solid-state spin qubits by decomposing the master-equation dynamics. *Physical Review A*, 102(3):033701, 2020.

[169] F Kimiaee Asadi, SC Wein, and Christoph Simon. Cavity-assisted controlled phase-flip gates. *Physical Review A*, 102(1):013703, 2020.

[170] RL Ahlefeldt, DL McAuslan, JJ Longdell, NB Manson, and MJ Sellars. Precision measurement of electronic ion-ion interactions between neighboring eu 3+ optical centers. *Physical review letters*, 111(24):240501, 2013.

[171] Howard Carmichael. *An open systems approach to quantum optics: lectures presented at the Université Libre de Bruxelles, October 28 to November 4, 1991*, volume 18. Springer Science & Business Media, 2009.

[172] Peter Zoller and Crispin W Gardiner. Quantum noise in quantum optics: the stochastic schrodinger equation. *arXiv preprint quant-ph/9702030*, 1997.

[173] Mohsen Razavi, Marco Piani, and Norbert Lütkenhaus. Quantum repeaters with imperfect memories: Cost and scalability. *Physical Review A*, 80(3):032301, 2009.

[174] W Dür, H-J Briegel, J Ignacio Cirac, and P Zoller. Quantum repeaters based on entanglement purification. *Physical Review A*, 59(1):169, 1999.

[175] Jia-Wei Ji, Yu-Feng Wu, Stephen C Wein, Faezeh Kimiaee Asadi, Roohollah Ghobadi, and Christoph Simon. Proposal for a room-temperature quantum network with diamonds and optomechanics at telecommunication wavelengths. *under preparation*, 2020.

[176] Yan Chen, Michael Zopf, Robert Keil, Fei Ding, and Oliver G Schmidt. Highly-efficient extraction of entangled photons from quantum dots using a broadband optical antenna. *Nature communications*, 9(1):1–7, 2018.

[177] Tian Zhong, Jake Rochman, Jonathan M Kindem, Evan Miyazono, and Andrei Faraon. High quality factor nanophotonic resonators in bulk rare-earth doped crystals. *Optics express*, 24(1):536–544, 2016.

[178] Jie Tian, Wei Yan, Yazhao Liu, Jun Luo, Daozhong Zhang, Zhiyuan Li, and Min Qiu. Optical quality improvement of si photonic devices fabricated by focused-ion-beam milling. *Journal of lightwave technology*, 27(19):4306–4310, 2009.

[179] Takashi Asano, Yoshiaki Ochi, Yasushi Takahashi, Katsuhiro Kishimoto, and Susumu Noda. Photonic crystal nanocavity with a q factor exceeding eleven million. *Optics express*, 25(3):1769–1777, 2017.

[180] Thomas Böttger, CW Thiel, Y Sun, and RL Cone. Optical decoherence and spectral diffusion at 1.5 μ m in er 3+: Y 2 sio 5 versus magnetic field, temperature, and er 3+ concentration. *Physical Review B*, 73(7):075101, 2006.

[181] Sumit Goswami, Khabat Heshami, and Christoph Simon. Theory of cavity-enhanced nondestructive detection of photonic qubits in a solid-state atomic ensemble. *Physical Review A*, 98(4):043842, 2018.

[182] Paul E Barclay, Kartik Srinivasan, and Oskar Painter. Nonlinear response of silicon photonic crystal microresonators excited via an integrated waveguide and fiber taper. *Optics express*, 13(3):801–820, 2005.

[183] Leigh S Martin and K Birgitta Whaley. Single-shot deterministic entanglement between non-interacting systems with linear optics. *arXiv preprint arXiv:1912.00067*, 2019.

[184] Juan Yin, Yuan Cao, Yu-Huai Li, Sheng-Kai Liao, Liang Zhang, Ji-Gang Ren, Wen-Qi Cai, Wei-Yue Liu, Bo Li, Hui Dai, et al. Satellite-based entanglement distribution over 1200 kilometers. *Science*, 356(6343):1140–1144, 2017.

[185] Ji-Gang Ren, Ping Xu, Hai-Lin Yong, Liang Zhang, Sheng-Kai Liao, Juan Yin, Wei-Yue Liu, Wen-Qi Cai, Meng Yang, Li Li, et al. Ground-to-satellite quantum teleportation. *Nature*, 549(7670):70–73, 2017.

[186] Sheng-Kai Liao, Wen-Qi Cai, Wei-Yue Liu, Liang Zhang, Yang Li, Ji-Gang Ren, Juan Yin, Qi Shen, Yuan Cao, Zheng-Ping Li, et al. Satellite-to-ground quantum key distribution. *Nature*, 549(7670):43–47, 2017.

APPENDIX A

Copyright permissions

This appendix states the copyright permissions required to include papers 1-3 in this thesis.

A.1 Permissions from journals

All these papers are published in journals that grant me permission to include them in my thesis. Proof of these permissions for the papers 1,2 and 3 are included in Figs. A.1, A.2, and A.3, respectively, via screen-shots from the journal websites.

A.2 Permissions from co-authors

Permission from all co-authors has been granted (via e-mail communication)

- Christoph Simon, Fig. Fig.A.4
- Stephen Wein, Fig. Fig.A.5
- Nikolai Lauk, Fig.A.6
- Neil Sinclair, Fig.A.7
- Chris O'Brien, Fig.A.8

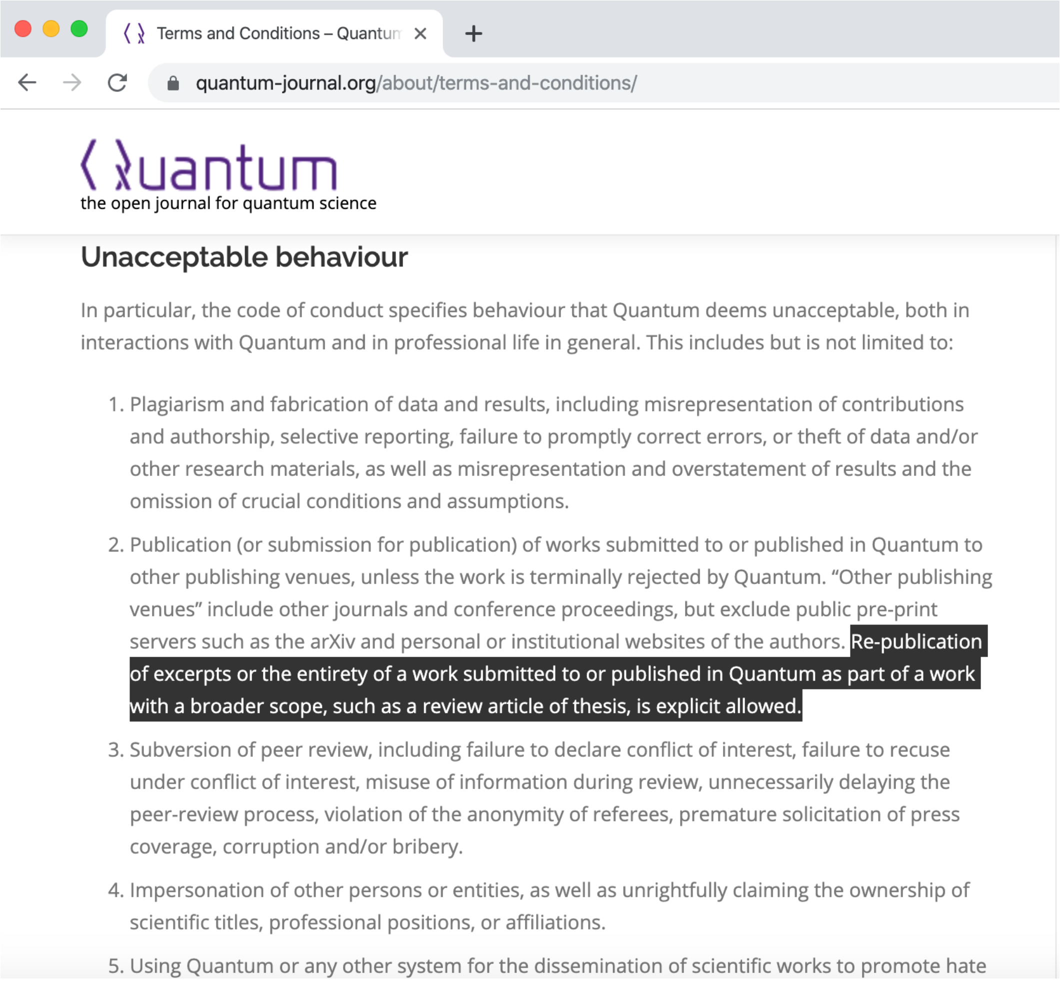

Unacceptable behaviour

In particular, the code of conduct specifies behaviour that Quantum deems unacceptable, both in interactions with Quantum and in professional life in general. This includes but is not limited to:

1. Plagiarism and fabrication of data and results, including misrepresentation of contributions and authorship, selective reporting, failure to promptly correct errors, or theft of data and/or other research materials, as well as misrepresentation and overstatement of results and the omission of crucial conditions and assumptions.
2. Publication (or submission for publication) of works submitted to or published in Quantum to other publishing venues, unless the work is terminally rejected by Quantum. "Other publishing venues" include other journals and conference proceedings, but exclude public pre-print servers such as the arXiv and personal or institutional websites of the authors. Re-publication of excerpts or the entirety of a work submitted to or published in Quantum as part of a work with a broader scope, such as a review article of thesis, is explicit allowed.
3. Subversion of peer review, including failure to declare conflict of interest, failure to recuse under conflict of interest, misuse of information during review, unnecessarily delaying the peer-review process, violation of the anonymity of referees, premature solicitation of press coverage, corruption and/or bribery.
4. Impersonation of other persons or entities, as well as unrightfully claiming the ownership of scientific titles, professional positions, or affiliations.
5. Using Quantum or any other system for the dissemination of scientific works to promote hate

Figure A.1: Proof of copyright of paper 1. This paper is published in Quantum, an open-access peer-reviewed journal for quantum science.

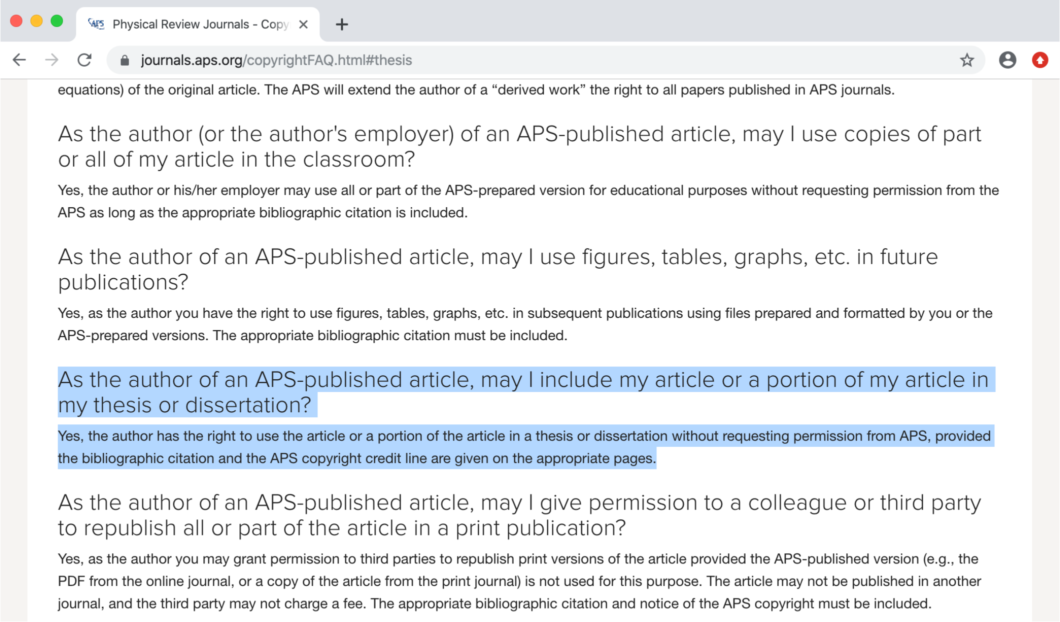

equations) of the original article. The APS will extend the author of a “derived work” the right to all papers published in APS journals.

As the author (or the author's employer) of an APS-published article, may I use copies of part or all of my article in the classroom?

Yes, the author or his/her employer may use all or part of the APS-prepared version for educational purposes without requesting permission from the APS as long as the appropriate bibliographic citation is included.

As the author of an APS-published article, may I use figures, tables, graphs, etc. in future publications?

Yes, as the author you have the right to use figures, tables, graphs, etc. in subsequent publications using files prepared and formatted by you or the APS-prepared versions. The appropriate bibliographic citation must be included.

As the author of an APS-published article, may I include my article or a portion of my article in my thesis or dissertation?

Yes, the author has the right to use the article or a portion of the article in a thesis or dissertation without requesting permission from APS, provided the bibliographic citation and the APS copyright credit line are given on the appropriate pages.

As the author of an APS-published article, may I give permission to a colleague or third party to republish all or part of the article in a print publication?

Yes, as the author you may grant permission to third parties to republish print versions of the article provided the APS-published version (e.g., the PDF from the online journal, or a copy of the article from the print journal) is not used for this purpose. The article may not be published in another journal, and the third party may not charge a fee. The appropriate bibliographic citation and notice of the APS copyright must be included.

Figure A.2: Proof of copyright of paper 2. This paper is published in Physical Review A, a journal of the American Physical Society (APS).

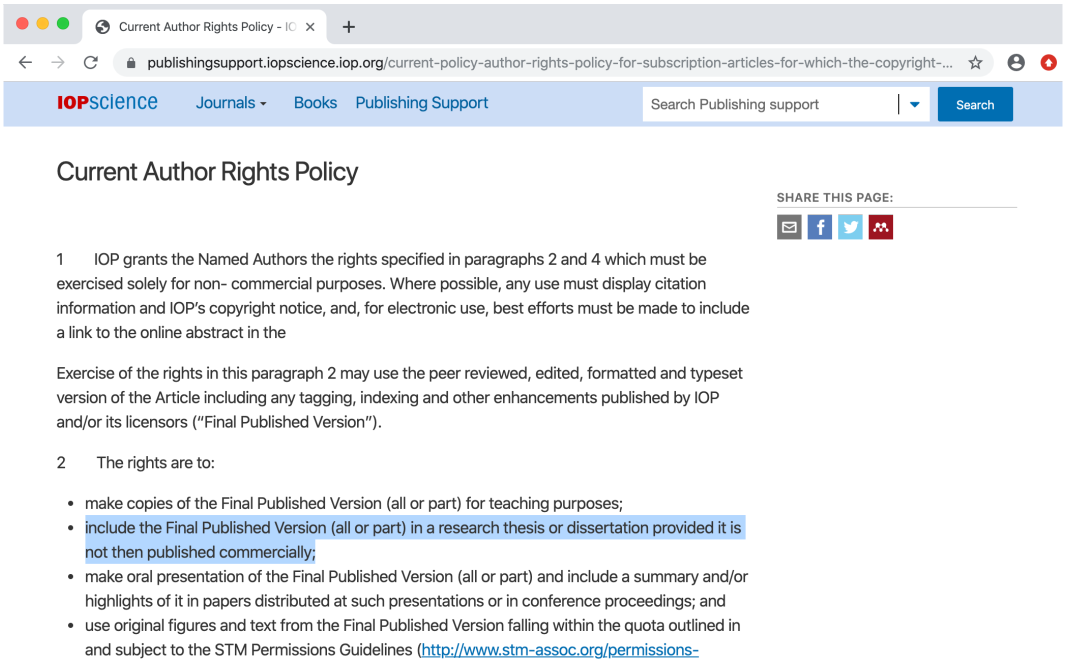

Current Author Rights Policy

1 IOP grants the Named Authors the rights specified in paragraphs 2 and 4 which must be exercised solely for non- commercial purposes. Where possible, any use must display citation information and IOP’s copyright notice, and, for electronic use, best efforts must be made to include a link to the online abstract in the

Exercise of the rights in this paragraph 2 may use the peer reviewed, edited, formatted and typeset version of the Article including any tagging, indexing and other enhancements published by IOP and/or its licensors (“Final Published Version”).

2 The rights are to:

- make copies of the Final Published Version (all or part) for teaching purposes;
- include the Final Published Version (all or part) in a research thesis or dissertation provided it is not then published commercially;
- make oral presentation of the Final Published Version (all or part) and include a summary and/or highlights of it in papers distributed at such presentations or in conference proceedings; and
- use original figures and text from the Final Published Version falling within the quota outlined in and subject to the STM Permissions Guidelines (http://www.stm-assoc.org/permissions-

Figure A.3: Proof of copyright of paper 3. This paper is published in Quantum science and Technology, a journal of the Institute of Physics (IOPscience).

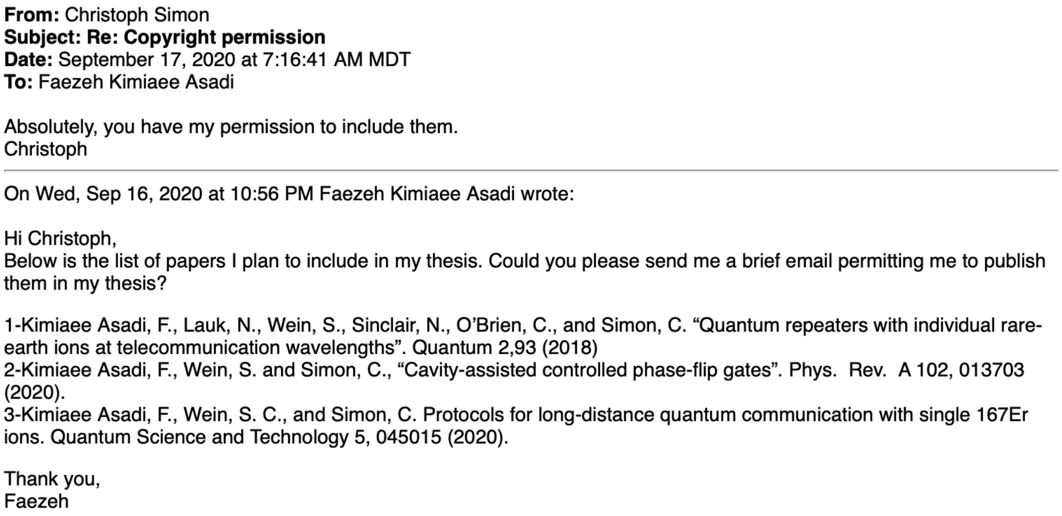

From: Christoph Simon
Subject: Re: Copyright permission
Date: September 17, 2020 at 7:16:41 AM MDT
To: Faezeh Kimiaee Asadi

Absolutely, you have my permission to include them.
Christoph

On Wed, Sep 16, 2020 at 10:56 PM Faezeh Kimiaee Asadi wrote:

Hi Christoph,
Below is the list of papers I plan to include in my thesis. Could you please send me a brief email permitting me to publish them in my thesis?

1-Kimiaee Asadi, F., Lauk, N., Wein, S., Sinclair, N., O'Brien, C., and Simon, C. "Quantum repeaters with individual rare-earth ions at telecommunication wavelengths". Quantum 2,93 (2018)
2-Kimiaee Asadi, F., Wein, S. and Simon, C., "Cavity-assisted controlled phase-flip gates". Phys. Rev. A 102, 013703 (2020).
3-Kimiaee Asadi, F., Wein, S. C., and Simon, C. Protocols for long-distance quantum communication with single 167Er ions. Quantum Science and Technology 5, 045015 (2020).

Thank you,
Faezeh

Figure A.4: Email from Christoph Simon granting me permission to publish the papers of which he is a co-author.

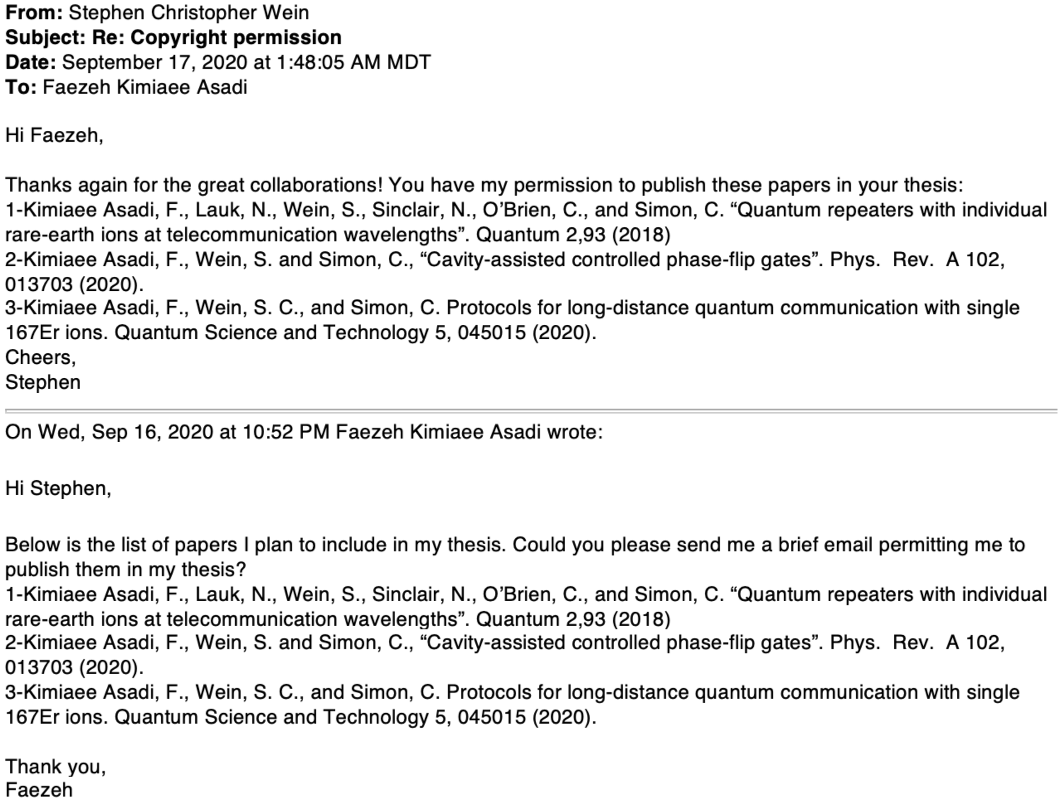

From: Stephen Christopher Wein
Subject: Re: Copyright permission
Date: September 17, 2020 at 1:48:05 AM MDT
To: Faezeh Kimiaee Asadi

Hi Faezeh,

Thanks again for the great collaborations! You have my permission to publish these papers in your thesis:
1-Kimiaee Asadi, F., Lauk, N., Wein, S., Sinclair, N., O'Brien, C., and Simon, C. "Quantum repeaters with individual rare-earth ions at telecommunication wavelengths". Quantum 2,93 (2018)
2-Kimiaee Asadi, F., Wein, S. and Simon, C., "Cavity-assisted controlled phase-flip gates". Phys. Rev. A 102, 013703 (2020).
3-Kimiaee Asadi, F., Wein, S. C., and Simon, C. Protocols for long-distance quantum communication with single 167Er ions. Quantum Science and Technology 5, 045015 (2020).
Cheers,
Stephen

On Wed, Sep 16, 2020 at 10:52 PM Faezeh Kimiaee Asadi wrote:

Hi Stephen,

Below is the list of papers I plan to include in my thesis. Could you please send me a brief email permitting me to publish them in my thesis?
1-Kimiaee Asadi, F., Lauk, N., Wein, S., Sinclair, N., O'Brien, C., and Simon, C. "Quantum repeaters with individual rare-earth ions at telecommunication wavelengths". Quantum 2,93 (2018)
2-Kimiaee Asadi, F., Wein, S. and Simon, C., "Cavity-assisted controlled phase-flip gates". Phys. Rev. A 102, 013703 (2020).
3-Kimiaee Asadi, F., Wein, S. C., and Simon, C. Protocols for long-distance quantum communication with single 167Er ions. Quantum Science and Technology 5, 045015 (2020).

Thank you,
Faezeh

Figure A.5: Email from Stephen Wein granting me permission to publish the papers of which he is a co-author.

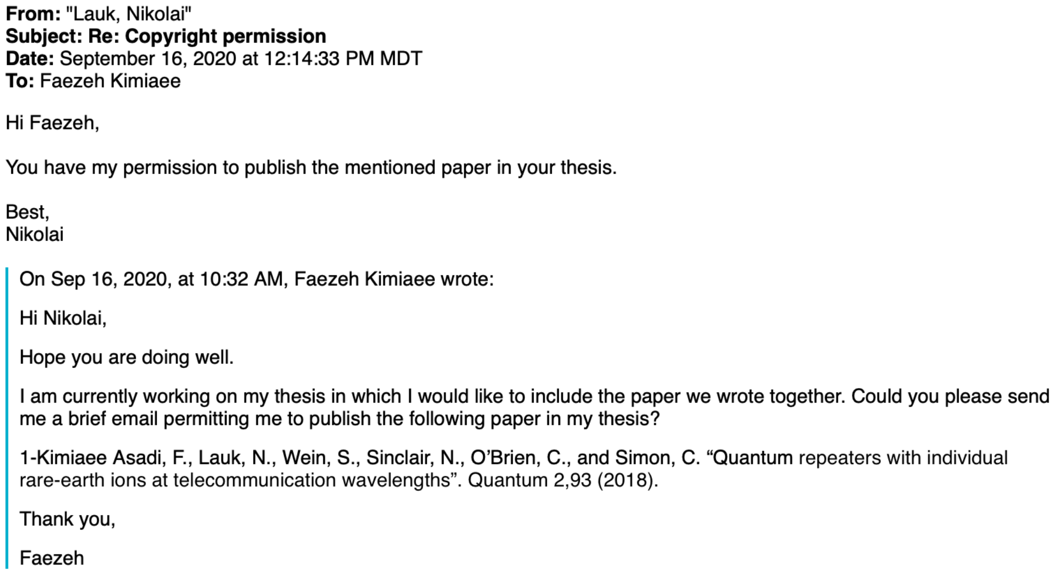

From: "Lauk, Nikolai"
Subject: Re: Copyright permission
Date: September 16, 2020 at 12:14:33 PM MDT
To: Faezeh Kimiaee

Hi Faezeh,

You have my permission to publish the mentioned paper in your thesis.

Best,
Nikolai

> On Sep 16, 2020, at 10:32 AM, Faezeh Kimiaee wrote:
>
> Hi Nikolai,
>
> Hope you are doing well.
>
> I am currently working on my thesis in which I would like to include the paper we wrote together. Could you please send me a brief email permitting me to publish the following paper in my thesis?
>
> 1-Kimiaee Asadi, F., Lauk, N., Wein, S., Sinclair, N., O'Brien, C., and Simon, C. "Quantum repeaters with individual rare-earth ions at telecommunication wavelengths". Quantum 2,93 (2018).
>
> Thank you,
>
> Faezeh

Figure A.6: Email from Nikolai Lauk granting me permission to publish the paper of which he is a co-author.

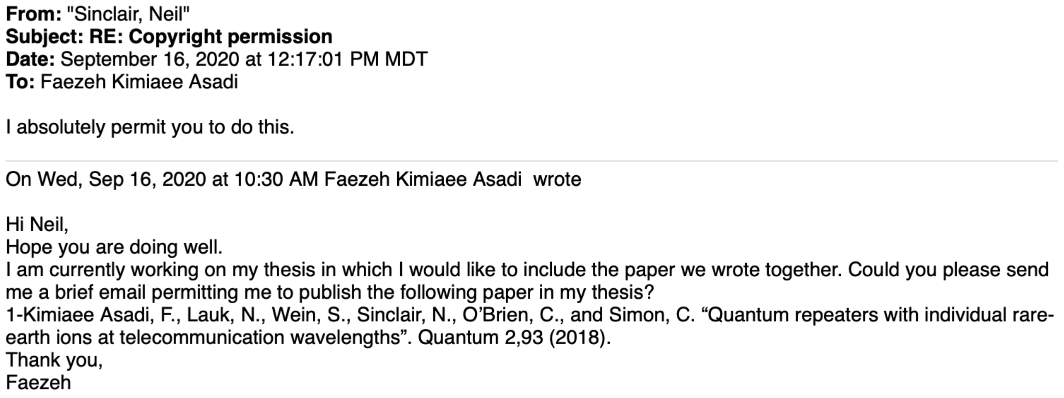

From: "Sinclair, Neil"
Subject: RE: Copyright permission
Date: September 16, 2020 at 12:17:01 PM MDT
To: Faezeh Kimiaee Asadi

I absolutely permit you to do this.

On Wed, Sep 16, 2020 at 10:30 AM Faezeh Kimiaee Asadi wrote

Hi Neil,
Hope you are doing well.
I am currently working on my thesis in which I would like to include the paper we wrote together. Could you please send me a brief email permitting me to publish the following paper in my thesis?
1-Kimiaee Asadi, F., Lauk, N., Wein, S., Sinclair, N., O'Brien, C., and Simon, C. "Quantum repeaters with individual rare-earth ions at telecommunication wavelengths". Quantum 2,93 (2018).
Thank you,
Faezeh

Figure A.7: Email from Neil Sinclair granting me permission to publish the paper of which he is a co-author.

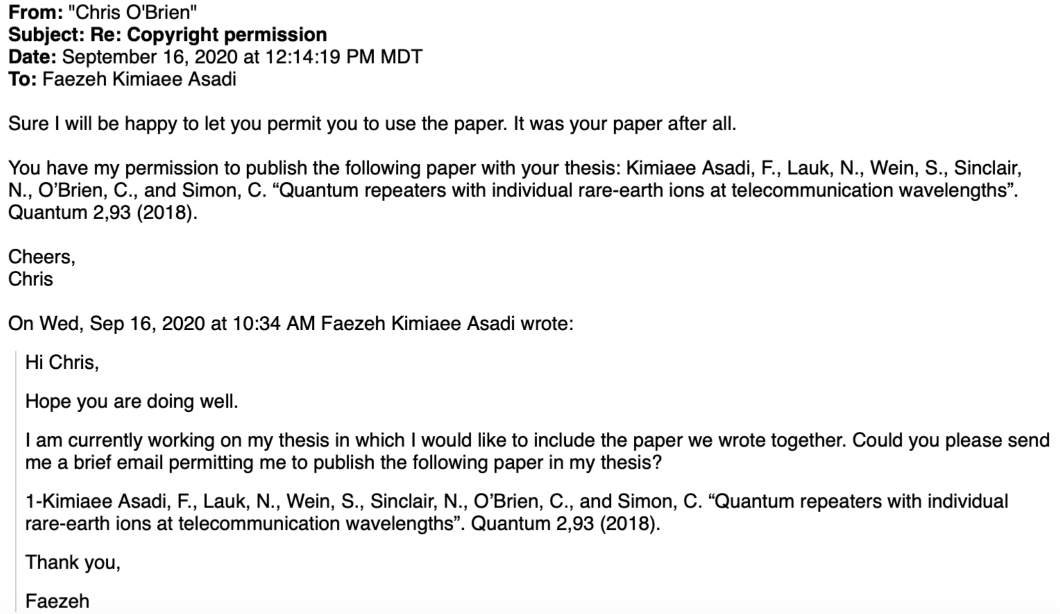

From: "Chris O'Brien"
Subject: Re: Copyright permission
Date: September 16, 2020 at 12:14:19 PM MDT
To: Faezeh Kimiaee Asadi

Sure I will be happy to let you permit you to use the paper. It was your paper after all.

You have my permission to publish the following paper with your thesis: Kimiaee Asadi, F., Lauk, N., Wein, S., Sinclair, N., O'Brien, C., and Simon, C. "Quantum repeaters with individual rare-earth ions at telecommunication wavelengths". Quantum 2,93 (2018).

Cheers,
Chris

On Wed, Sep 16, 2020 at 10:34 AM Faezeh Kimiaee Asadi wrote:

> Hi Chris,
>
> Hope you are doing well.
>
> I am currently working on my thesis in which I would like to include the paper we wrote together. Could you please send me a brief email permitting me to publish the following paper in my thesis?
>
> 1-Kimiaee Asadi, F., Lauk, N., Wein, S., Sinclair, N., O'Brien, C., and Simon, C. "Quantum repeaters with individual rare-earth ions at telecommunication wavelengths". Quantum 2,93 (2018).
>
> Thank you,
>
> Faezeh

Figure A.8: Email from Chris O'Brien granting me permission to publish the paper of which he is a co-author.